Development of Low-cost Organic Solar Cells Using Polythiophenes as Donors

by

Zhifang Zhang

A thesis

presented to the University of Waterloo

in fulfillment of the

thesis requirement for the degree of

Master of Applied Science

in

Chemical Engineering

Waterloo, Ontario, Canada, 2019

Author's Declaration

I hereby declare that I am the sole author of this thesis. This is a true copy of the thesis,

including any required final revisions, as accepted by my examiners.

I understand that my thesis may be made electronically available to the public.

Abstract

The need to develop sustainable, eco-friendly energy sources is a major driving force in the development of efficient photovoltaic cells. Organic solar cells are a relatively new solar energy technology compared to their inorganic counterparts and have many desirable properties including light weight, easy fabrication and potential for large-scale manufacture. Till now many semiconducting polymers have been synthesized and investigated extensively. One of the widely common donor polymers is P3HT, which has been used with fullerene-based acceptors as BHJ blend systems in OPV. However, because of the high cost and weak absorption of fullerene-based acceptors, non-fullerene acceptors have been investigated as promising alternatives. ITIC, as a representative of non-fullerene acceptors, exhibits broad strong absorption and high electron mobility. Although the ideal PCE is 9%, the highest PCE of P3HT:ITIC obtained till now in literature is 1.25% only which may be due to the recombination of free charges. In this thesis, we tried to overcome the recombination of free charges by using P3HT with lower regioregularity (P3HT rr~85%) which would increase the interaction between donor and acceptor and help to enhance charge transfer. Interestingly, organic solar cells with P3HT (rr~85%):ITIC as the active layer approached a PCE (Power conversion efficiency) of 1.33% which is significantly higher than P3HT (rr~98%):ITIC device with a PCE of 0.76%. The height and phase AFM images suggested interpenetrating morphology with lower RMS roughness in the P3HT(rr~85%):ITIC blend film, indicating better bulk charge transport properties. Moreover, both hole and electron mobilities of P3HT (rr~85%):ITIC were higher which could be explained by the better bi-continuous network formation at nanoscale. Consequently, P3HT (rr~85%):ITIC exhibited higher short circuit current density (Jsc) resulting in better performance.

In order to balance the needs of low cost and high performance, our group synthesized

two novel donor polymers (P-TOBT-1 and P-TOBT-2) with simpler synthetic route and lower cost and the PCE based on the OSCs reached 9.04% after optimization. To the best of our knowledge, this is the lowest synthetic cost with high PCE above 9%. PTOBT-1 contains only Z configuration in the side chain while PTOBT-2 contains both Z and E configurations. The Voc for the blend of P3HT:ITIC was 0.53 V, while a significantly higher Voc of up to 0.90 V was obtained with P-TOBT-1 and P-TOBT-2 as donors. Because of superior bulk charge transport properties, P-TOBT-1:ITIC showed higher Jsc 19.86 mA/cm^2 resulting in a better PCE (9.04%) than P-TOBT-2:ITIC (PCE: 6.32%) , which may be caused by higher crystallinity and smoother morphology.

Acknowledgements

Table of Contents

List of Figures

List of Tables

List of Abbreviations and Symbols

AFM: atomic force microscopy

BGBC: bottom gate bottom contact

CV: cyclic voltammetry

D-A: donor-acceptor

DDTS: dodecyl trichlorosilane

FF: fill factor

HOMO: highest occupied molecular orbital

I_{ON}/I_{OFF}: current ON/OFF ratio

Jsc: short-circuit current density

λ_m: wavelength of incident light with maximum adsorption

L: channel length

LUMO: lowest unoccupied molecular orbital

OTFT: organic thin film transistor

OPV: organic photovoltaic

OSC: organic solar cell

PCE: power conversion efficiency

RMS: root mean square

Rs: series resistance

Rsh: shunt resistance

UV-Vis: ultraviolet-visible

Voc: open-circuit voltage

V_{th}: threshold voltage

V_G: gate voltage

μ: charge carrier mobility

W: channel width in OTFT

XRD: X-ray diffraction

Other abbreviations and symbols are defined in the text.

Chapter 1.   Introduction

1.1 Research Background

The annual energy provided from the sun far exceeds energy reserve as shown in **Figure 1-1**.[1,2] In addition, solar energy is a renewable and environmentally-friendly resource, which does not account for any harmful emissions during generation and consumption.[3] Thus, the technologies for utilizing solar power will be the key to solve the exhaustion of fossil fuels and environmental issues.[4]
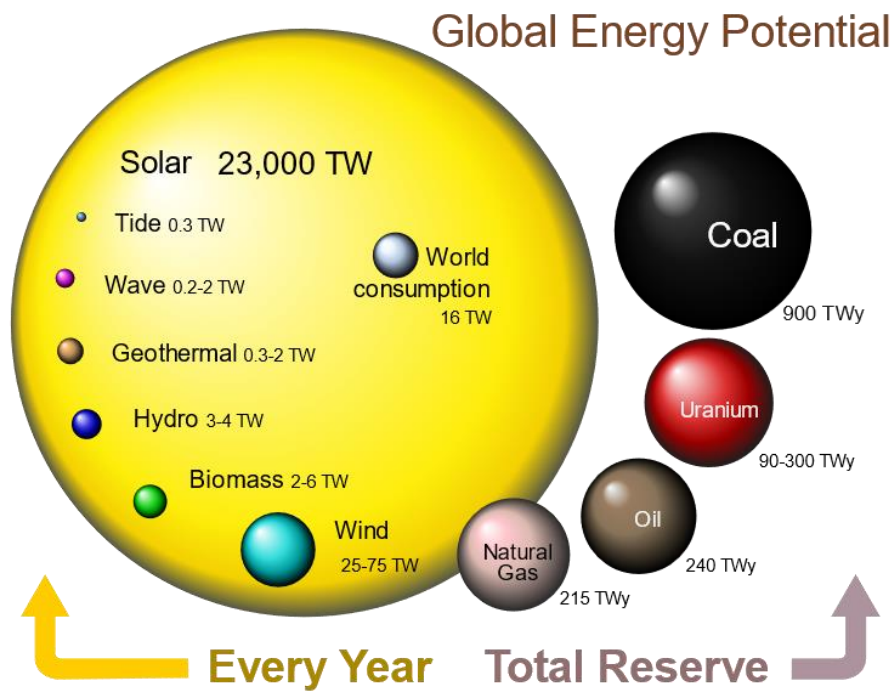
Figure 1-1 A fundamental look at energy potential for the planet.[2]

Solar cell appears as one of the important photovoltaic energy conversion methods that can directly convert solar light into electrical energy, as schematically described in (**Figure 1-2**), showing the typical solar cell configuration. To date, there are numerous solar cells manufactured from different materials, which can be traditionally classified into three generations: The first generation of solar photovoltaics are mainly made of

crystalline silicon, such as monocrystalline silicon (Mono c-Si), and polycrystalline silicon (Poly c-Si).[5] The first-generation solar cells are well-developed in fabrication process and have been the most popular for residential use due to high efficiency (~25%).[5] However, the high manufacturing cost and relatively heavy weight of crystalline silicon limit the development of the first-generation solar cells.[6] The second generation of solar cells are usually called thin-film solar cells because they comprise of thin successive layers with p-n junction such as amorphous silicon and cadmium telluride (CdTe).[7,8] Compared with the first-generation solar panels, thin film solar cells require less materials and can be deposited on larger and less expensive substrate such as glass, thereby lowering the cost.[9] However, thin-film solar cells exhibited half the efficiency of monocrystalline or polycrystalline solar panels.[10] Furthermore, most materials of thin film solar cells are highly toxic (cadmium and arsenic) and are becoming increasingly rare (indium).[10] Those challenges within inorganic solar cells are driving attempts to explore alternative approaches for utilizing solar energy. Third-generation solar cells, which apply solution processable materials, such as semiconducting organic macromolecules and inorganic nanoparticles, hold a promising prospect for photovoltaic systems.[11] Although this type of solar cells is still the subject of intense research, the third generation of solar cells, especially organic solar cells, have showed enormous potential due to several prominent features. First, organic materials generally possess high absorption coefficients and light weight, thereby holding promise for fabricating portative devices with thin-film architecture[13,14] Second, mechanical flexibility and solution processability allow organic solar cells to be manufactured using high throughput printing techniques in roll-to-roll processes, which make it possible to manufacture them in large-scale with lower production cost.[12–14]

Third, because of diversity of organic materials, OSCs can be modified with different properties in order to fit different applications. [15,16]
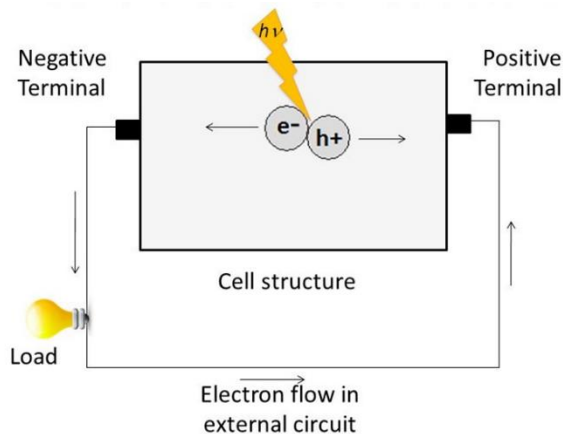
Figure 1-2 The typical solar cell configuration.[17]

1.2 Organic Solar Cells

In 1986, the first successful organic solar cell was introduced by Tang.[18] This photovoltaic device employed an active bilayer that consisted of copper phthalocyanine (CuPc) as electron donor and 3,4,9,10-perylenetetracarboxyl-bis-benzimidazole as acceptor, achieving a power conversion efficiency (PCE) of about 1%. As shown in **Figure 1-3**, the photovoltaic conversation firstly involves light absorption in the active layers, followed by the donor material generating exciton, which is a pair of electron and hole correlated by Coulomb force. As the exciton diffuses to the interface between donor and acceptor, it dissociates into an electron and a hole. Consequently, the electron will transfer from the donor to the acceptor, resulting from the potential difference between the highest occupied molecular orbital (HOMO) of the donor and the lowest unoccupied molecular orbital (LUMO) of the acceptor. Finally, after the fully separated

free electron and hole flow into the respective electrodes, the solar energy is converted into the photovoltaic current.[12]
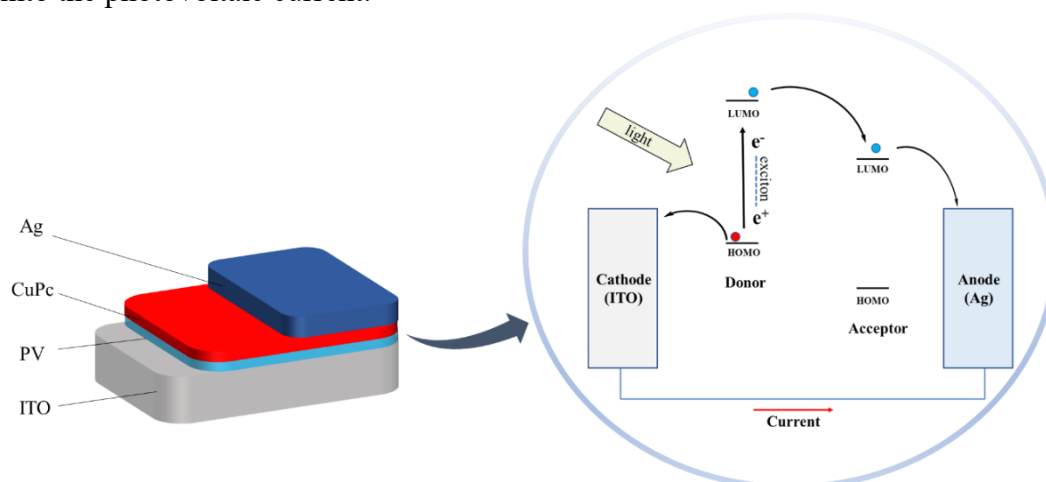
Figure 1-3 The schematic representation and principle of OSC reported by Tang.

In 1993, Sariciftci, N. S.et.al[19] reported a similar planar heterojunction (PHJ) organic solar cell whose acceptor was replaced by a material with better electron conductivity, phenyl-C61-butyric acid methyl ester ($PC_{61}BM$). However, the limited lifetime of excitons defines that they can only diffuse a short length within 10-20 nm.[19–23] Thus, in such planar heterojunction devices, there is a loss of photogenerated charges because of recombination of excitons that are far from the donor-acceptor interface, resulting in low quantum efficiencies.[24,25] Consequently, to achieve higher substantial energy conversion, Halls.et.al[26] and Yu.et.al[20] introduced bulk-heterojunction (BHJ) by blending acceptor and donor materials in a nanoscale interpenetrating network (**Figure 1-4**). With significantly improved donor-acceptor heterojunction interface[27], the excitons could diffuse throughout the whole bulk of active layer.[28]. Since then, BHJ architecture has become a typical configuration for OSCs.[29]
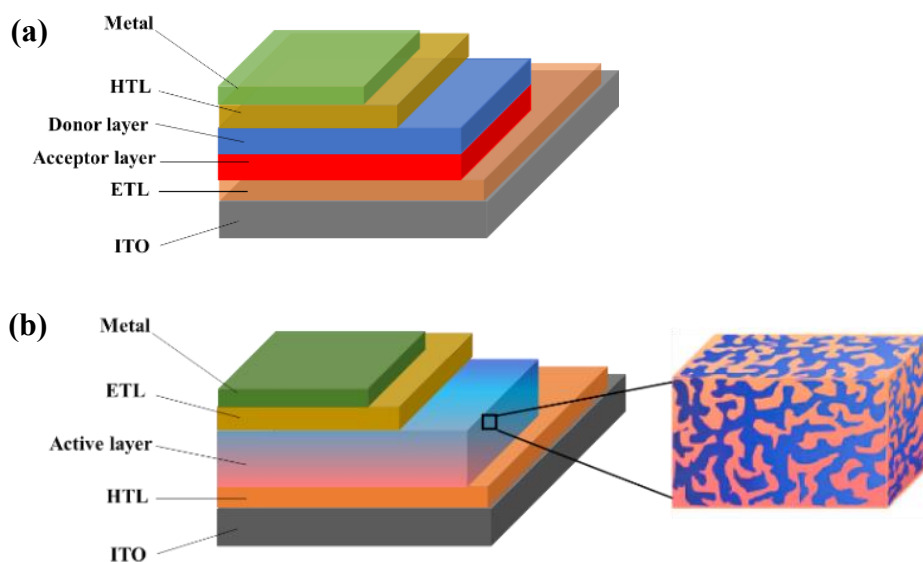
Figure 1-4 Typical device configurations of organic solar cells: **(a)** bilayer device with planar heterojunction, **(b)** bulk heterojunction device

1.3 Organic Solar Cell Working Principles

The working principle of an organic solar cell can be schematically illustrated by four consecutive steps[30]: (i)Formation of excitons by absorbing photons, (ii) Diffusion of excitons to the interface of donor-acceptor, (iii) Subsequent separation of excitons into free carriers and (iv) Charge carriers transport through donor and acceptor phases and collection by the respective electrodes. Inevitably, all these steps have limitations and restrictions and in the following section, details of each step in BHJ OPV devices will be analyzed.

Firstly, light absorption in organic solar cells results in the formation of excitons which can separate into free charges only at interface of donor and acceptor while inorganic solar cells could directly generate free charges.[31] Generally, organic materials for photoactive layer have much higher molar absorption ($\sim10^5$ cm^{-1}) compared with that of the inorganic semiconductor such as polycrystalline silicon ($\sim10^3$ cm^{-1}).[32] This important property allows the active layer of OPVs to absorb a significant amount of

light with a thickness of only 100-200 nm. In addition, the band gap calculated by the difference of LUMO/HOMO levels also limits the absorption coefficient.[33] More specifically, photoactive layer only could absorb photons with energy more than the difference between excited electronic and ground states energy level (band gap). Secondly, in order to separate into free charges, excitons need to diffuse to the interface of donor and acceptor. **Figure 1-5** showed several states in the process from exciton formation to charge transfer. As mentioned before, in BHJ solar cells, it exhibits that only excitons generated within the distance of 10-20 nm from a donor-acceptor interface can separate into free charge carriers, otherwise the geminate recombination occurs, as shown in **Figure 1-6 (a)**.[23] Typically, time scale for this charge transfer process is sub-picosecond, which is 1000 times faster than nonradiative or radiative decay of photo excitons at heterojunction interface.[20] The pairs of electrons and holes resulting from the charge transfer of excitons with weak binding energy located in the acceptor and donor phases could be either separated by electric filed or dissociated with thermal energy.[34] The energy of charge transfer excitons is lower than optical band gap which allows electron transfer to occur instead of energy transfer.[35] In general, the energy losses in this process greatly influence the open circuit voltage and the underlying theories still have issues and have not been fully investigated yet.[36] Also, an appropriate difference between LUMOs of the two materials is required, in order to offer the necessary energy to break the bond between electron and hole, which gives rise to free charges.[37] Usually, this energy offset should be larger than 0.3 eV.[22]
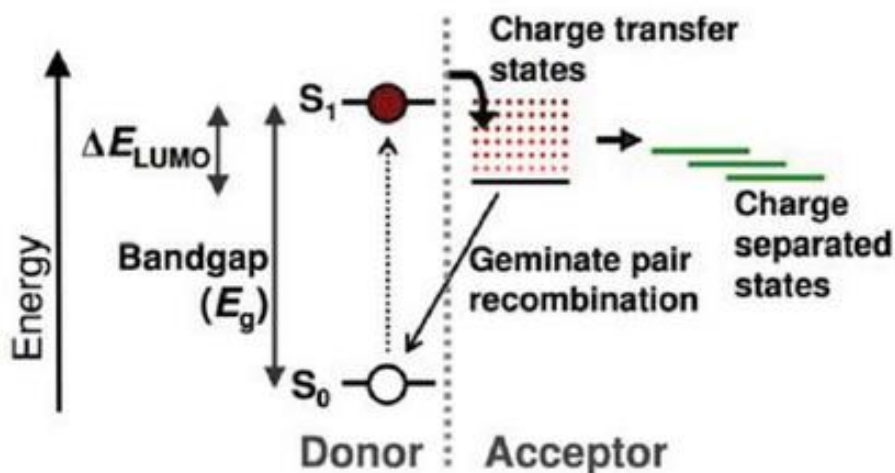
Figure 1-5 Schematic view of the charge separation and geminate pair recombination. [38]

Thirdly, after the separation of excitons, the charge carriers need to be transported and collected by the respective electrodes to generate photocurrent. Compared with crystalline inorganic counterparts, the electronic states in organic semiconductors are more localized rather than the delocalization of charges over the electronic states.[39,40] Particularly, in organic materials, the inter-molecular or hopping charge transport which is thermally activated and occurred between neighbouring molecules is generally less efficient than that in intra-molecule.[41,42] In addition, in BHJ devices, the photoactive layer is always semi-crystalline or amorphous where hopping transport prevails.[43,44] Besides the properties such as energy disorder, hopping charge transport also heavily depends on the morphology resulting from the blending of acceptor and donor phases in BHJ devices.[45] Furthermore, even though excitons have completely separated, there still exists the possibilities of bimolecular recombination, shown in **Figure 1-6 (b)**, which also is strongly influenced by morphologic features of photoactive layer.[39] For instance, based on P3HT:PCBM devices, annealing could redistribute phases resulting in higher crystallinity of P3HT and larger domain size of PCBM, shown in **Figure 1-7**.[46] Thus, after annealing, the efficiency could increase from 1% to 4.9% because of the reduction of recombination

7

and the enhancement of electron transport.[47,48]. Therefore, the accurate control on morphology is a crucial and challenging part in an efficient OSC. So far, various processing methods, such as thermal and solvent annealing[27,49,50] or the use of solvent additives[51,52], have been applied to optimize microstructure and improve the performance of OPV devices.

(a)

(b)

Geminate pair recombination

Bimolecular recombination
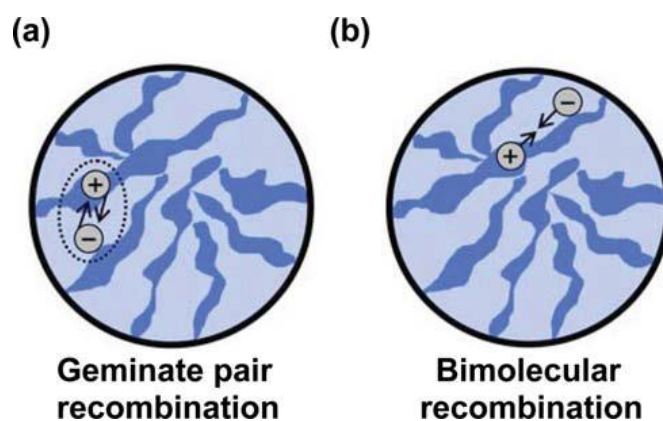
Figure 1-6 Illustrations of **(a)** geminate pair recombination and **(b)** bimolecular recombination.[38]

amorphous P3HT/PCBM matrix

PCBM cluster

a) non-annealed film

substrate

annealing

P3HT-crystallite with a-axis orientation

amorphous P3HT/PCBM matrix

PCBM cluster

b) annealed film

substrate

P3HT-molecule

• PCBM-molecule
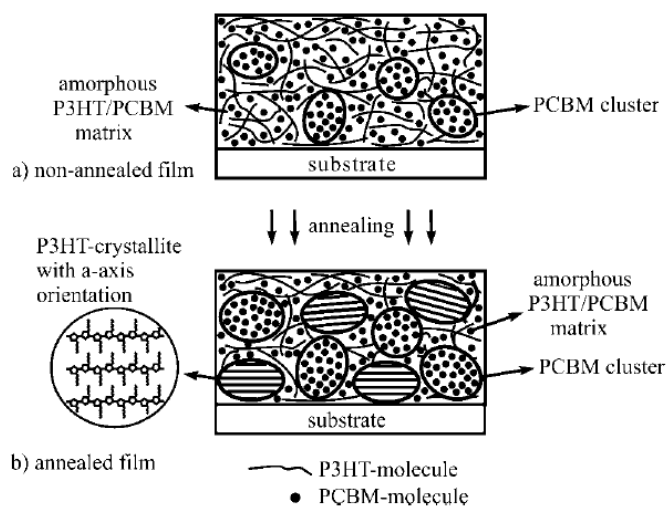
Figure 1-7 Schematic pictures showing the changes in the P3HT:PCBM blend film after annealing.[53]

8

Finally, the last step of mechanism in OSC solar energy conversion is the extraction and collection of free charges to the respective electrodes. It is worthy noting that the work function of the anode needs to have a higher energy level than the HOMO level of donor. Correspondingly, the work-function of cathode should have a lower energy level than LUMO level of acceptor.[54] Additionally, the bi-continuous donor and acceptor phases are also required to guarantee a high yield of free charges transport from interface to electrode.[31]

1.4 Characterization of Polymers for Organic Solar Cells

1.4.1 Ultraviolet-Visible (UV) Absorption and Photoluminescence (PL) Spectroscopy

UV-vis absorption spectroscopy is a fundamental measurement to obtain the profile of absorption. The wavelength of onset in absorption spectrum determines the minimum excitation energy required for a photon excites an electron from ground states to the lowest excited states, known as band gap. Then what follows is the relaxation of the excited states resulting in the emission of light (fluorescence). PL spectroscopy is used for measuring intensity of fluorescence probed by a specific excitation wavelength. Due to the non-radiative pathways such as the vibrational transition, showed in **Figure 1-8**, the energy of fluorescence transition is lower thus accompanying with longer wavelength rather than shorter absorption wavelength. This phenomenon is known as stokes shift. Additionally, compared with absorption and fluorescence spectra, the shapes of these two transitions are mirror images of each other initially predicted by Frank Condon principle.[55]

PL measurement indicates the sum of radiative emissions of excitons relaxing from the excited states to ground states. In D/A blend film, the excitons undergo a non-radiative transition due to charge transfer, which is known as photoluminescence quenching efficiency (PLQE):

$$PLQE = 1 - \frac{PL_{Blend}}{PL_{Neat}}$$

where PL$_{Blend}$ is the PL intensity (counts) of blend films and PL$_{neat}$ is the PL intensity (counts) of neat films.
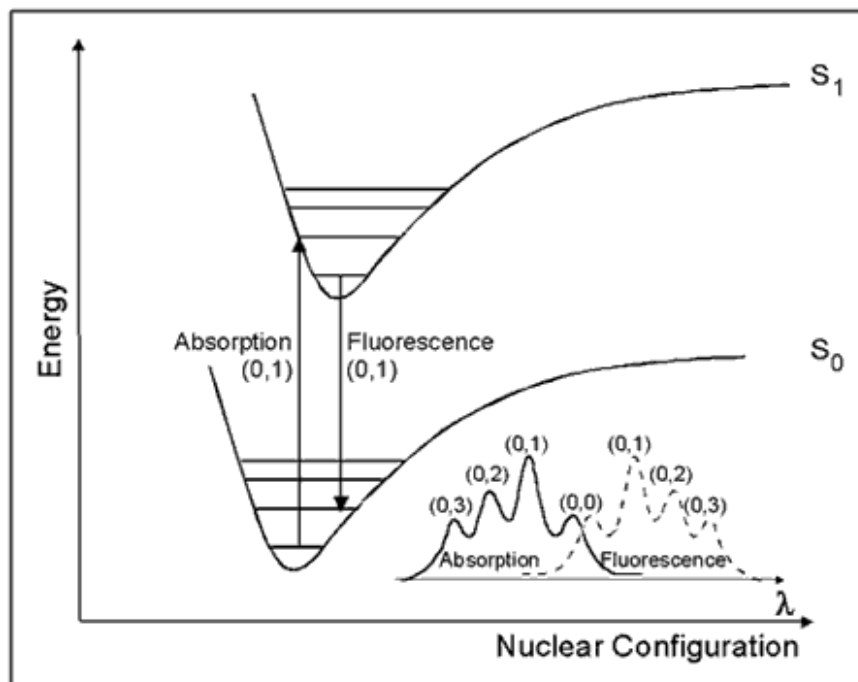
Figure 1-8 Frank Condon principle.[56]

1.4.2 Cyclic Voltammetry

Cyclic voltammetry (CV) is a type of measurement to reveal the electrochemical properties of materials. The HOMO and LUMO levels can be estimated from the oxidation and reduction onset potentials. Thus, the HOMO and LUMO levels can be calculated by using the equations below:

$$E_{HOMO} \text{ (eV)} = -e\ (E_{ox}^{onset}) - 4.8 \text{ eV}$$

$$E_{LUMO} \text{ (eV)} = -e\ (E_{red}^{onset}) - 4.8 \text{ eV}$$

where e is the energy of an electron and E_{ox}^{onset} and E_{red}^{onset} are oxidation and reduction redox onset potentials, respectively. Herein, ferrocene was used as a reference. Also, HOMO energy level of ferrocene is -4.8 eV oxidation and onset potential sets at 0 V.

1.4.3 Current Density -Voltage Curves

The most important parameters, as shown in **Figure 1-9**, are open circuit voltage

(Voc), short circuit current density (Jsc), power conversion efficiency fill factor (FF), series resistance (Rs) and shunt resistance (Rsh).
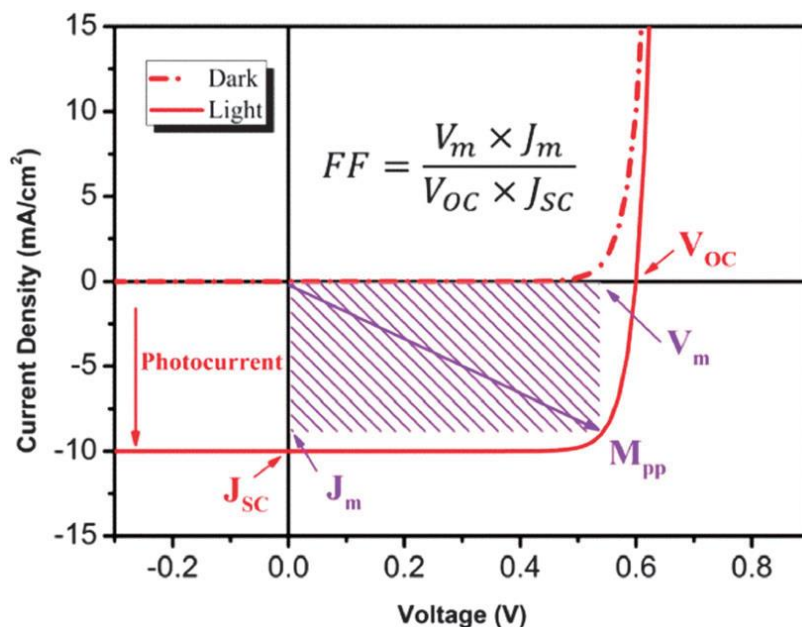
Figure 1-9 Schematic representation of important characteristics derived from typical J-V curves.[57]

Under steady illumination and open circuit voltage conditions, the electron and hole generated in photoactive layer will accumulate at cathode and anode respectively, generating a potential difference that is described as Voc.[58] This potential difference (Voc) also corresponds to the maximum possible voltage that could be obtained from an OSC.[59,60] In a BHJ OSC, the Voc is mainly determined by the offset of the HOMO level of donor and LUMO level of acceptor and can be inferred by following relationship[22]:

$$Voc = \frac{1}{q}(|E_{DHOMO}| - |E_{ALUMO}|) - 0.3V$$

where q is the elementary charge, E_{DHOMO} and E_{ALUMO} are HOMO energy level of donor and LUMO energy level of acceptor respectively, 0.3V arises from disorder within the intermixing donor and acceptor phases. This equation also provided a guideline to design

and tune a new material in order to get expected energy level. Besides the energy levels, the real value of Voc is also influenced by charge transfer states, the interface between donor and acceptor and the work function of electrodes.[61,62]

The Jsc is the current density obtained under short circuit conditions when the voltage is 0 V and ultimately depends on the amount of free charges collected by the electrodes. However, there are many factors influencing the amount of free charges carriers before the free charges are extracted at electrodes. As discussed before, the properties of photoactive layer such as the absorption coefficient and band gap determine the primary number of photons that can be absorbed. [33] Furthermore, the dissociation of excitons and mobility of free charge carriers vary with the morphology and the nature of materials.[31]

The power conversion efficiency (PCE) is one of the important parameters to illustrate performance of OSC, which is defined by the ratio of P_{max} (maximum power) to P_{in} (incident light).

$$PCE = \frac{P_{max}}{P_{in}} = \frac{Jsc \times Voc \times FF}{Pin}$$

where the fill factor (FF) is the ratio of the maximum power (P_{in}) obtained from the cell ($I_m \times V_m$) to the product (P_{max}) of Jsc and Voc, as shown in **Figure 1-9**. Therefore, the value of FF could indicate the quality of a solar cell and represent the deviation of current-voltage curves from theoretical one.[63] The FF is strongly affected by the electrical resistances (Rsh and Rs) and increasingly low series resistance and high shunt resistance results in higher FF, as shown in **Figure 1-10**. The Rs could be reduced by some processing methods to decrease the contact resistance such as the accurate choice of hole and electron transport layer and electrodes.[64] On the other hand, the Rsh could increase by decreasing the shunt currents flow through the photoactive layer by improving the BHJ morphology.[65]
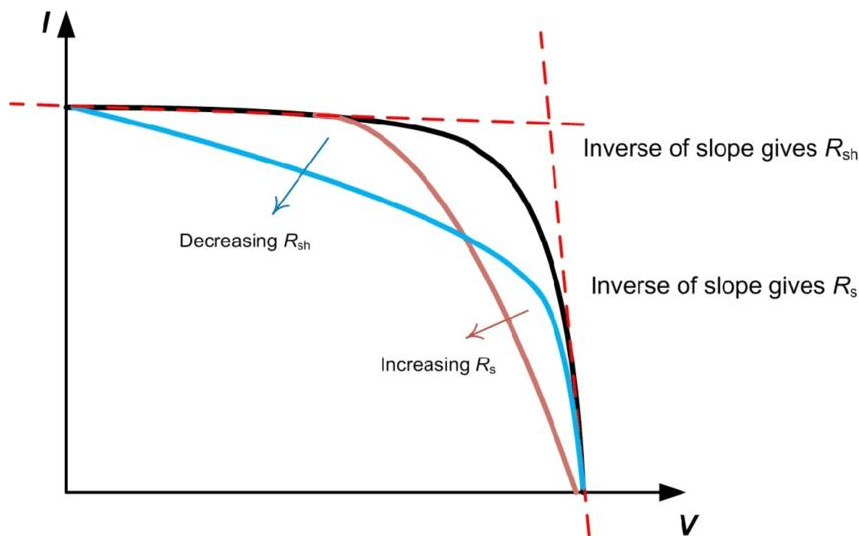
Figure 1-10 Evolution of I-V curves with higher Rs and lower Rsh. [64]

1.4.4 External Quantum Efficiency

The external quantum efficiency (EQE), known as the incident photon conversion efficiency (IPCE), is another crucial photovoltaic parameter assessing solar cells. It is defined as, under short-circuit conditions, the fraction of incident photons that collected by electrodes as photoinduced charges, as shown in the equation below:

$$\text{External Quantum Efficiency (EQE)} = \frac{Number\ of\ electron\ collected}{Number\ of\ incident\ photons}$$

In EQE, due to the limitation of light absorption capability of photoactive layer and losses because of scattering and reflection, the value is always far from unity in most BHJ OPV cells.

1.5 The State-of-the-art of Polythiophenes for Organic Solar Cells

Polythiophene (PT) and its derivatives have been exhibited great potentials for the application in organic solar cells.[66] Among these polymers, P3HT (poly(3-hexylthiophene)) played a prominent role in the development of organic solar cells as the early class of polythiophenes. The power conversion efficiency of OSC based on P3HT:$PC_{71}BM$ (phenyl-C_{71}-butyric acid methyl ester) have reached up to 5%.[67] In

13

order to further improve the performance of organic solar cells, considerable efforts have been devoted into molecular design of polythiophenes[68] and optimizing the architecture of devices[69]. On the one hand, many donor polythiophenes through engineering the donor and acceptor units achieved high performance in organic solar cells and the chemical structures of representatives were shown in **Figure 1-11**. For instance, Fan[68] fabricated solar cell with PBDD-ff4T:ITIC and obtained a PCE of 9.2% . Furthermore, Xu[70] introduced a new Pt-PSFTZ with the acceptor (Y6) and got a PCE of 16.35%. On the other hand, as shown in **Figure 1-12,** Meng[71] used tandem cell strategy to enable efficient light absorption and achieved a PCE of 17.3% of organic solar cell.
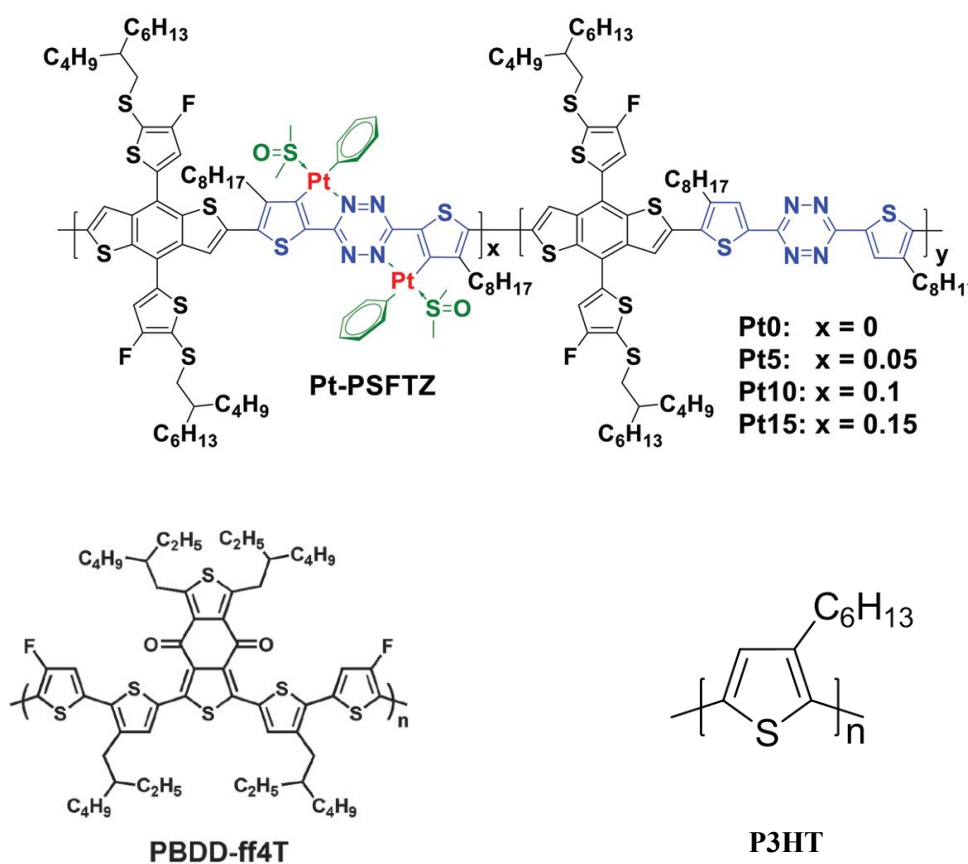
Figure 1-11 Chemical structures of P3HT and recent donor polythiophenes (Pt-PSFTZ[70] and PBDD-ff4T[68]) with high performance for OSCs.
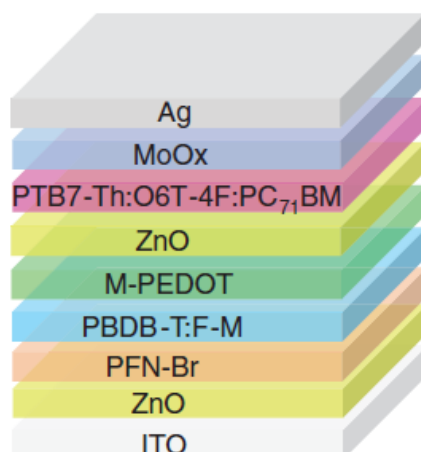
Figure 1-12 Device architecture of the tandem cell. [71]

However, as shown in the **Figure 1-11**, although some polythiophenes achieved high performance of organic solar cells, P3HT has simplest synthetic route thus has the lowest synthetic complexity (SC) [72] among all reported polythiophenes. Additionally, the performance of P3HT-based organic solar cells still has great potential to improve. For example, the ideal PCE of P3HT:ITIC solar cell is 6%~7% but the realistic PCE remains at 1.25%.[73] Besides, tandem structures also increase complexity in the manufacturing process, inhibiting the application of roll-to-roll printing techniques and commercialization.[71] Therefore, in order to make commercializable large area solar cells, it is still necessary and worthy to develop low-cost donor polythiophenes with simpler synthetic route in traditional bulk heterojunction structure.

1.6 Objective and Structure of This Thesis

Poly(3-hexylthiophene) (P3HT) has the greatest potential for commercialization due to good stability and straightforward synthetic route[74]. At present, the power conversion efficiencies (PCE) have recently climbed to 16.5%[75] and 17.3%[71] for single-junction and tandem organic solar cells respectively. However, compared with P3HT, the synthesis of high-performing polymers tends to be complex and expensive thus inhibiting the commercialization of OSCs. Therefore, the development of low-cost

donor polymers is a promising way to balance the needs of commercialization and high performance.

In Chapter 2, the objective of this work is to improve the OSC performance of P3HT:ITIC by introducing P3HT (rr~85%) to increase interaction between donor and acceptor phases. Furthermore, the results will be further analyzed through several characterizations including X-ray diffraction and atomic force microscopy.

In Chapter 3, to further improve Voc and Jsc based on P3HT:ITIC, the P-TOBT-1 and P-TOBT-2 (polythiophene derivatives) which synthesized with relative low cost and simple synthesis, were used as donors to achieve a balance between high performance and commercial use. The optical, electrochemistry and crystal properties will be further investigated.

Finally, in Chapter 4, the conclusions of this thesis will be summarized, and future work will be proposed for further improvement.

Chapter 2. Influence of Regioregularity of P3HT on the Performance of P3HT:ITIC Solar Cells

2.1 Introduction

In the past decade, many soluble polythiophene derivatives have been designed, synthesized and researched owing to their potential application in organic photovoltaics field.[76] Specifically, poly(3-hexylthiophene) (P3HT) has been investigated extensively [49,77–80] due to its relatively straightforward synthetic route[74] and stability[81], and possibility of large-scale production.[82] For the aspect of acceptor, fullerene derivatives such as phenyl-C_{61}-butyric acid methyl ester ($PC_{61}BM$) and $PC_{71}BM$, shown in **Figure 2-1**, have attracted the most attention and achieved the high efficiencies. For example, the power conversion efficiency of OSC based on P3HT:$PC_{71}BM$ (phenyl-C_{71}-butyric acid methyl ester) have reached up to 5%.[67] These fullerene derivatives are derived from C_{60} and C_{70} fullerenes, which have fully conjugated structures, with many advantages including (i) the strong electron accepting capability which enables electrons can be delocalized in the whole molecule, (ii) high electron mobility, (iii) the ability to aggregate a in appropriate length-scale in BHJ films for charge separation.[83] However, fullerene-based acceptors have some significant drawbacks such as weak absorption and high cost of synthesis.[84] Additionally, $PC_{61}BM$ or $PC_{71}BM$ blends with polymers have morphological instability because of the tendency to aggregate in BHJ film under thermal stress.[85] Therefore, in last five years, researchers have devoted considerable efforts to develop non-fullerene acceptor (NFA) [66,83,86,87] and the chemical structures of some of the most common NFAs are shown in **Figure 2-1**. The power conversion efficiency of PTB7-TH:ITIC or PBDB-T:IT4F based solar cell can be up to 6.59%[86] and 13.1%[88], respectively. Among these acceptors, ITIC[86] exhibits broad and strong absorption, high electron mobility and relatively simpler synthesis than its

derivatives (such as IT-4F). Moreover, in BHJ blend films, it is morphologically stable owing to the four rigid 4-hexylphenyl substituents which could restrict aggregation[89].
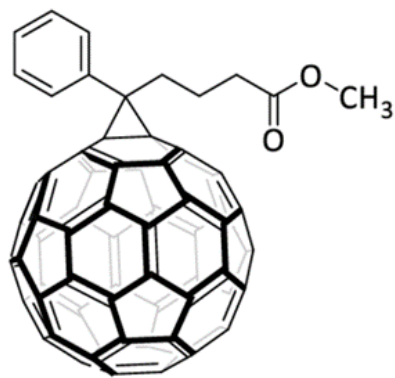
PC$_{61}$BM
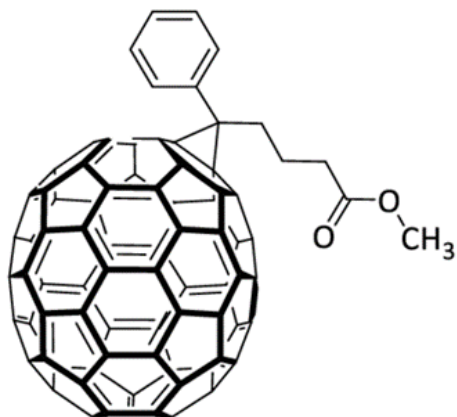
PC$_{71}$BM
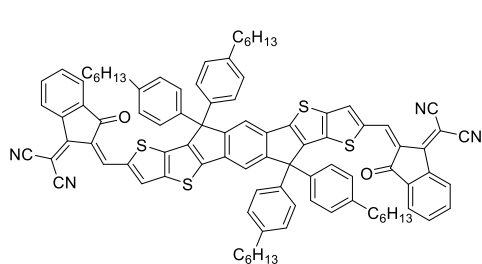
ITIC
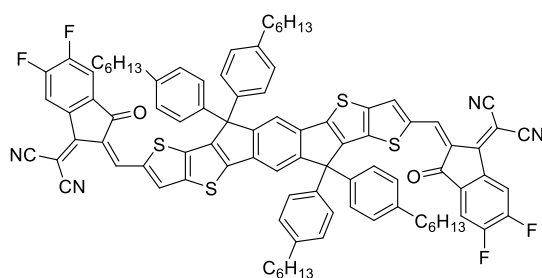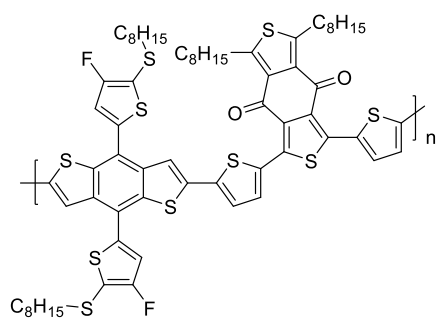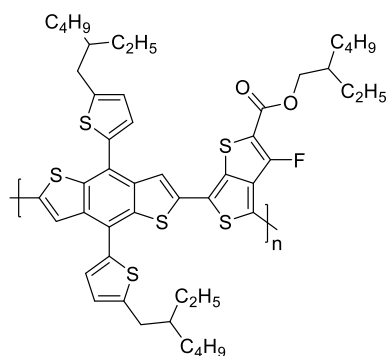
IT-4F

PTB7-TH

PBDB-T

Figure 2-1 Chemical structure of PC$_{61}$BM, PC$_{71}$BM, ITIC, IT-4F, PTB7-TH and PBDB-T.

Therefore, P3HT and ITIC are frequently used donor and acceptor, respectively. From initial assessment for the feasibility of OSCs, P3HT:ITIC blend showed complementary absorption profile and matched energy levels (**Figure 2-2 (a)**). However, the highest PCE of this system found in papers is around 1.25%[73] due to the recombination of free charges. In several studies[90,91], it has been found that P3HT with high molecular weight (Mn > 20kDa) and high RR(>95%) exhibits optimal performance because of the improved electronic and optical properties. Nevertheless, a systematic study of the effect of regioregularity has been reported on P3HT:PCBM systems, indicating P3HT(rr~85%):PCBM showed better thermal stability than P3HT(rr~98%):PCBM because weaker phase segregation.[92] In this chapter, we introduced regiorandomness in P3HT to increase interaction between donor and acceptor phases which would enhance charge separation and transfer. The resulting effects on the charge carrier mobilities and phase segregation in D/A blend have also been studied. In this work, the P3HT and ITIC were bought from 1 Materials. The AFM, EQE and XRD were measured by Pankaj Kumar. Furthermore, the NMR spectra were acquired by Wuqi Li to determine the regioregularity of polymers.
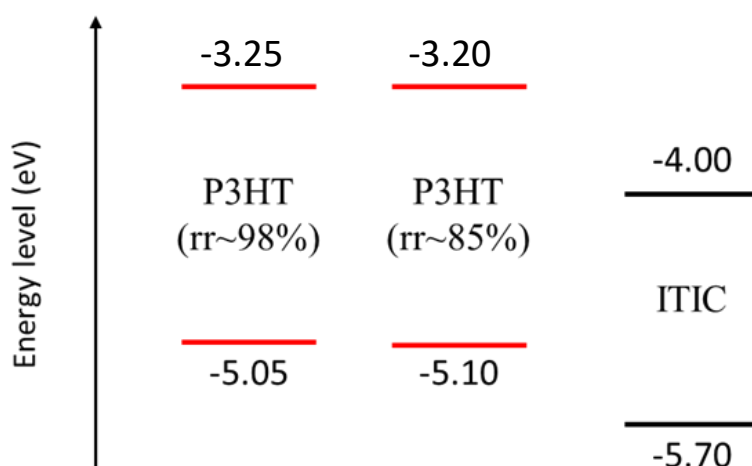
Figure 2-2 The comparison of the HOMO/LUMOs of P3HT(rr~98%), P3HT(rr~85%) and ITIC.

2.2 Characterization of P3HT(rr~98%) and P3HT(rr~85%)

2.2.1 Characterization of P3HT(rr~98%) and P3HT(rr~85%) by UV-Vis, PL, CV and XRD

The P3HT polymer can be synthesized with different regioregularities by controlling the ratio of couplings, which includes head-to-tail (HT), head-to-head (HH) and tail-to-tail (TT), shown in **Figure 2-3**.

Head-to-tail   Head-to-head   Tail-to-tail

(H-T)   (H-H)   (T-T)
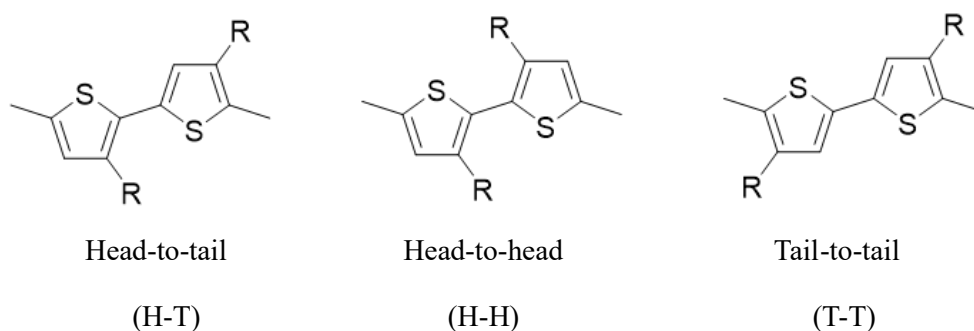
Figure 2-3 Three substituted bithiophenes.

Also, the ratio of couplings can be controlled by the structure of catalyst and reaction temperature. For example, P3HT(rr~86%) can be obtained through a copolymerization of 2-bromo-3-hexylthiophene and 5-bromo-3,3′-dihexyl-2,2′-bithiophene.[92] Additionally, as shown in **Figure 2-4 (a)**, regioselectivity can be influenced by reaction temperature.[93] Due to the regularity of the hexyl sidechain, the backbone of regioregular P3HT has less torsion angles, resulting in a longer conjugated pathway and more ordered intermolecular packing,[94] that would lead to higher degree of crystallinity.

(a)

R	T/t	2/3 (%)[a]
n-Hexyl	rt/1 h	90 : 10
n-Hexyl	−45°C to rt/4 h	93 : 7
n-Hexyl	−78°C to rt/4 h	97 : 3

(b)
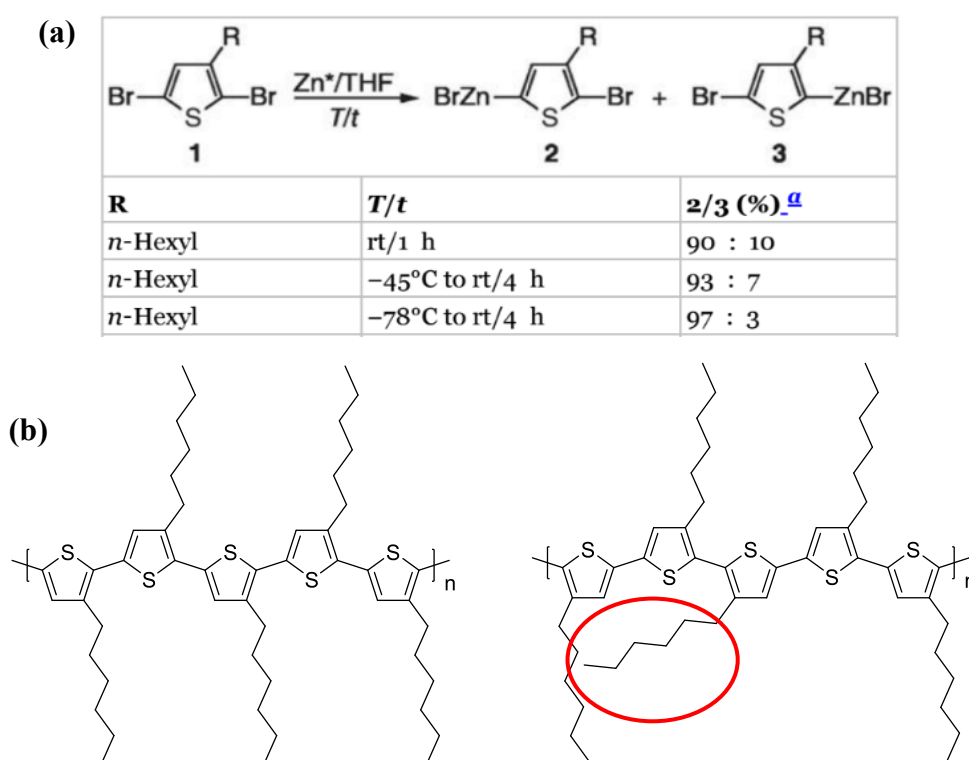
Figure 2-4 (a) Regiocontrolled synthesis of P3HT[93], **(b)** regioregular P3HT and regiorandom P3HT.

The UV-Vis absorption spectra of P3HT(rr~98%), P3HT(rr~85%), ITIC, P3HT(rr~98%):ITIC and P3HT(rr~85%):ITIC in thin films are shown in **Figure 2-5 (a)** and **(b)**. The thin films were obtained after annealing at 160 °C for 10 mins, which is the optimal annealing temperature for OSCs based on P3HT:ITIC.[73] From **Figure 2-5**

(a), both polymers showed maximum absorption wavelength (λ_m) at 505 nm. Due to randomly oriented side chains, P3HT(rr~85%) exhibited weaker intermolecular interactions. Therefore, compared with P3HT(rr~85%), P3HT(rr~98%) exhibited more red-shift adsorption wavelength and a weak shoulder peak at 546 nm indicating more extended conjugation of the polymer chains in the thin film. The optical band gap of P3HT(rr~98%) and P3HT(rr~85%) in thin film are calculated to be 1.91 and 1.95 eV, respectively, from the onsets of absorption profiles. On the other hand, the λ_m of ITIC is around 707 nm and a weak shoulder appeared at 651 nm. Moreover, the absorption of P3HT polymers and ITIC showed complementary absorption profile, which would be beneficial for enhanced light absorption as discussed in pervious study[95]. The absorption profiles of blend films are shown in **Figure 2-5 (b)**.
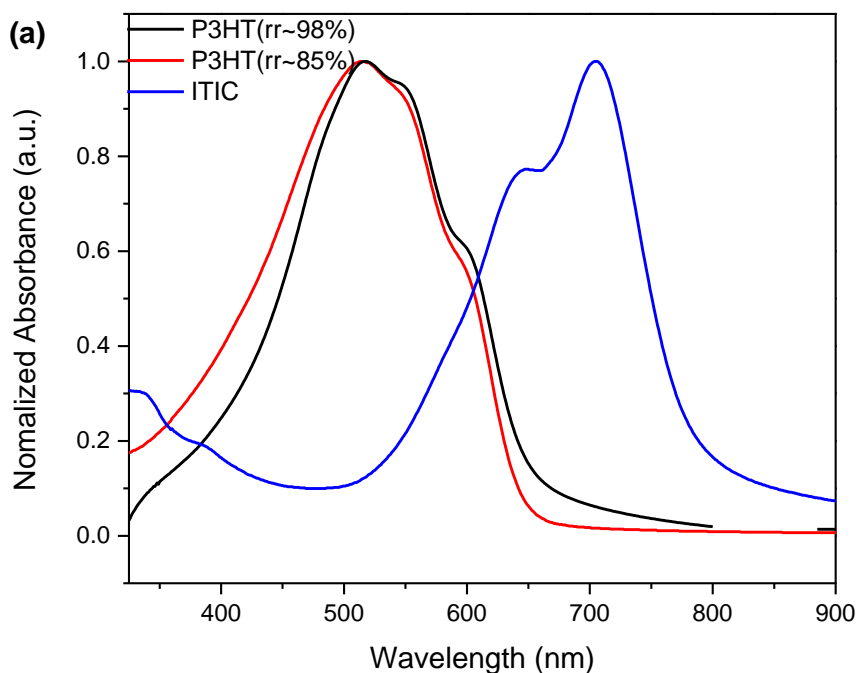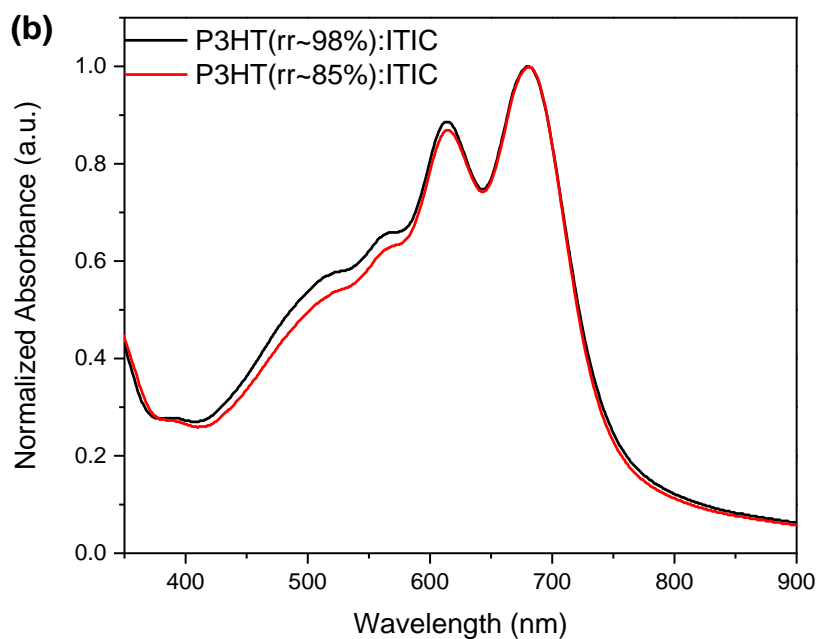
Figure 2-5 (a) Normalized UV-vis absorption spectra of P3HT(rr~98%),
P3HT(rr~85%) and ITIC in thin film, **(b)** normalized UV-vis absorption spectra of
P3HT(rr~98%):ITIC, P3HT(rr~85%):ITIC in thin film (D/A ratio:1:1).

The CV curve was used to measure electrochemical properties of the polymers, as shown in **Figure 2-6**. The HOMO level of P3HT(rr~98%) and P3HT(rr~85%) calculated from the oxidation onset potentials was -5.05 eV and -5.10 eV respectively. Combined with band gap, the calculated LUMO energy levels of P3HT(rr~98%) and P3HT(rr~85%) are 3.25 eV and 3.20 eV respectively. The LUMO energy offsets (ΔE_{LUMO}) between P3HT(rr~98%) or P3HT(rr~85%) and ITIC are 0.75 eV and 0.80 eV, respectively, which is higher than empirical threshold of 0.3 eV for exciton dissociation efficiently.
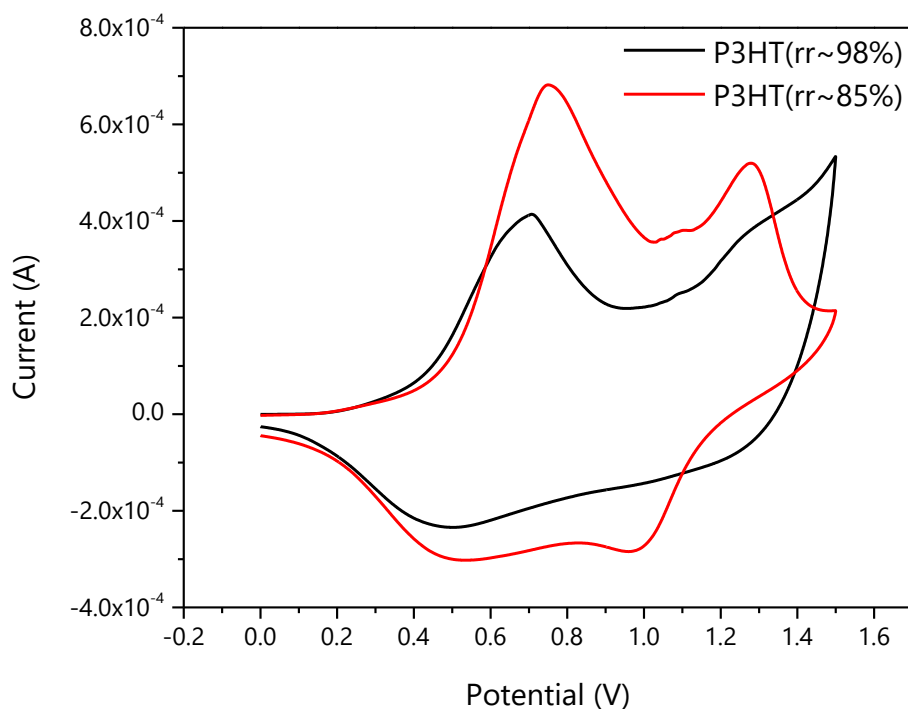
Figure 2-6 The CV diagram of P3HT(rr~98%) and P3HT(rr~85%) at a scan rate of 0.1 V/s. The electrolyte was 0.1 M tetrabutylammonium hexafluorophosphate in anhydrous acetonitrile.

The efficiency of separation of excitons was investigated through measuring the photoluminescence quenching efficiency (PLQE) of blend films. As shown in **Figure 2-7**, the photoluminescence of P3HT(rr~98%) and P3HT(rr~85%) are quenched by ITIC with PLQE of 96% and 95%, respectively, when P3HT polymer was excited at the wavelength of 505 nm. Moreover, both photoluminescence of ITIC are quenched by P3HT(rr~98%) and P3HT(rr~85%) with PLQE around 85%, respectively, when ITIC was excited at wavelength of 707 nm. From the results of quenching, considerable interactions between donor and acceptor in the blend occurred. In addition, both donor and acceptor excitation showed similar PLQE, indicating similar efficiency of excitons dissociation and separation.
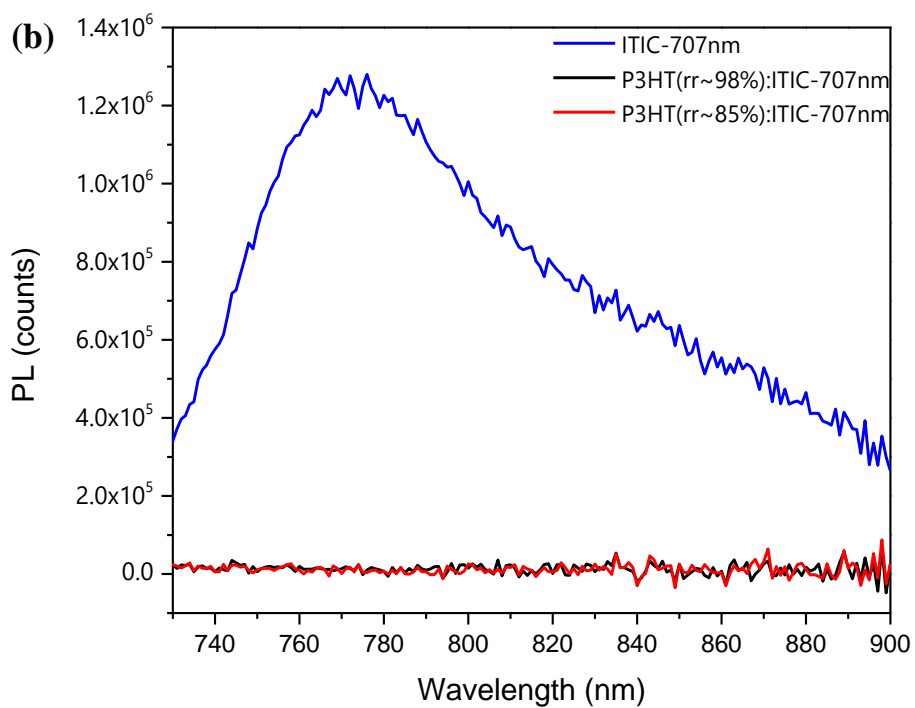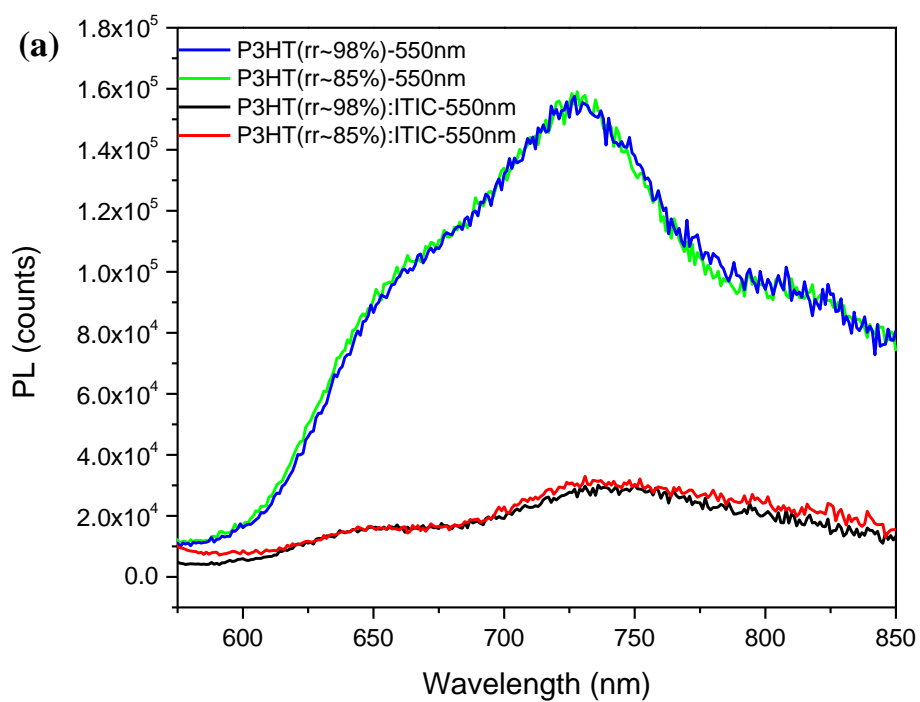
Figure 2-7 (a) Photoluminescence spectra of neat P3HT(rr~98%), P3HT(rr~85%) and

blends of P3HT(rr~98%):ITIC and P3HT(rr~85%):ITIC, employing an excitation

wavelength at 505 nm, **(b)** neat ITIC and blends of P3HT(rr~98%):ITIC and

P3HT(rr~85%):ITIC, employing an excitation wavelength at 707 nm.

The molecular orientation of the polymer P3HT (rr~98%) and P3HT (rr~85%) films was characterized by reflective X-ray diffraction technique. As shown in **Figure 2-5**, P3HT (rr~98%) pristine film showed an intense diffraction peak at $2\theta = 5.28°$, corresponding to the interlayer lamellar d-spacing of 1.67 nm ($q_z = 0.37$ Å^{-1}). On the other hand, a clear lamellar peak at $2\theta = 5.22°$ ($q_z = 0.37$ Å^{-1}) in P3HT (rr~85%), corresponding to the interlayer lamellar d-spacing of 1.69 nm. Because of disordered side-chain of P3HT (rr~85%), the diffraction peak of lamellar packing exhibited lower intensity compared with that of P3HT (rr~98%).
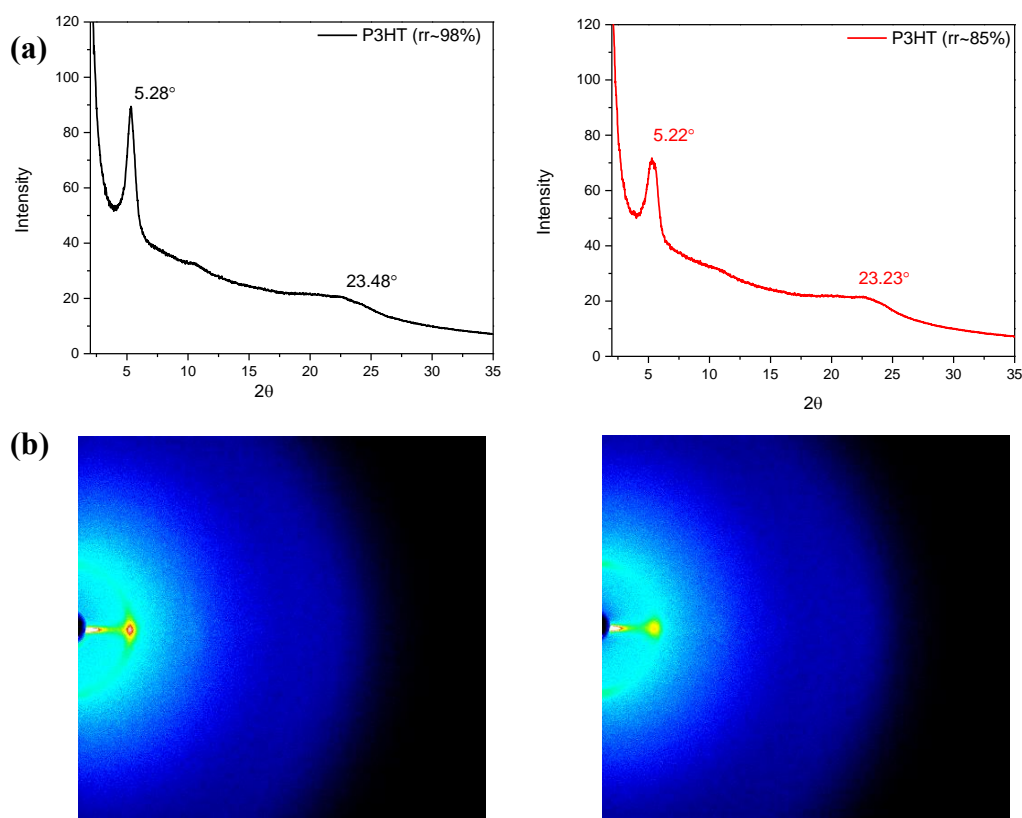
Figure 2-8 (a) The out of plane XRD patterns obtained from the spin-coated P3HT

(rr~98%) and P3HT (rr~85%) thin film on SiO2/Si substrates modified by DDTS, annealed at 160 °C for 10mins. **(b)** GIWAXS scans for P3HT (rr~98%) and P3HT (rr~85%).

Since the π-π stacking peak is quite weak in out of plane XRD patterns, we measured transmission XRD patterns, as shown in **Figure 2-9**. The π- π stacking in both neat P3HT (rr~98%) and P3HT (rr~85%) are visible at $2\theta =23.48°$ and $2\theta =23.23°$, corresponding π- π distance of 0.37 nm and 0.38 nm, respectively.

(a)　　　　　　　　　　　　　　　　　**(b)**
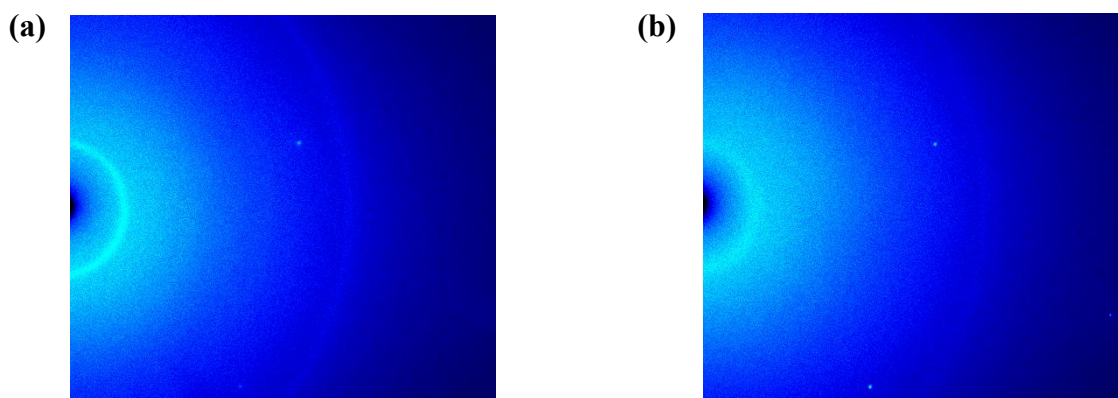
Figure 2-9 Transmission geometry X-ray diffraction obtained from the spin-coated **(a)** P3HT (rr~98%) and **(b)** P3HT (rr~85%) thin film. The patterns were obtained on a thin mica film, thick films were casted from chloroform solution.

Figure 2-10 depicts the XRD diagram based on P3HT (rr~98%):ITIC and P3HT (rr~85%):ITIC. It is clearly shown that both blend films exhibit no obvious change in size of lamellar d-spacing but the intensity decreases inevitably by blending with ITIC. Interestingly, the intensity of π-π stacking peak based on P3HT (rr~85%):ITIC is higher as compared to the peak in P3HT (rr~98%):ITIC, which is favorable for vertical charge transport. While in the P3HT (rr~98%) blend, the presence of high intensity lamellar

peak (edge on stacking preference) is favorable for parallel charge transport. P3HT (rr~85%) has less intensity of lamellar peak in comparison of P3HT (rr~98%).
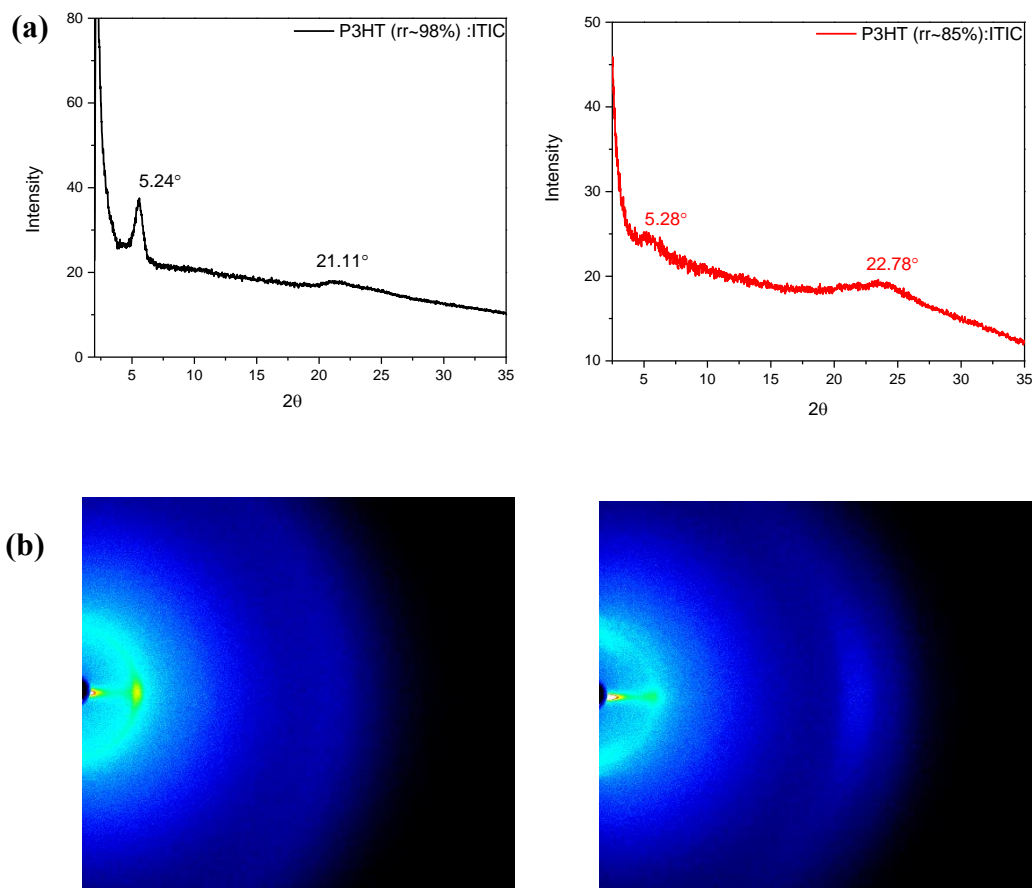
Figure 2-10 (a) The out of plane XRD patterns obtained from the spin-coated P3HT (rr~98%):ITIC and P3HT (rr~85%):ITIC thin film on SiO2/Si substrates modified by DDTS, annealed at 160 °C for 10mins. **(b)** GIWAXS scans for P3HT (rr~98%):ITIC and P3HT (rr~85%):ITIC.

2.2.2 OTFT Performance of P3HT(rr~98%) and P3HT(rr~85%)

P3HT(rr~98%) and P3HT(rr~85%) were evaluated as p-channel semiconductors in BGBC OTFT devices, as shown in **Figure 2-11.** The OTFT fabrications and characterizations are shown in   section 2.5.1.
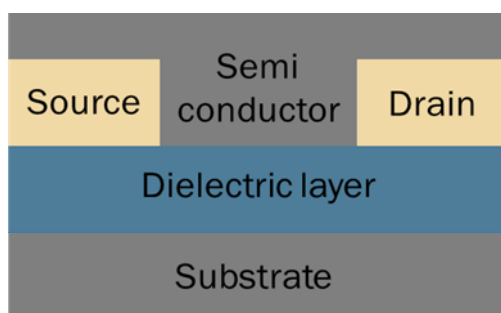
Figure 2-11 Configurations of BGBC (bottom-gate, bottom-contact) OTFT structure.

Both polymers exhibited p-type charge transport behavior (**Figure 2-12** and **Table 2-1**). All OTFT devices were annealing at 160 °C which is the optimal annealing temperature for solar cell.[73] For devices based on P3HT (rr~98%), the highest hole mobility is 1.01×10^{-2} cm^2 V^{-1} s^{-1} with an average of 6.73×10^{-3} cm^2 V^{-1} s^{-1} and the output curve and transport curve are shown in **Figure 2-12**. For devices based on P3HT (rr~85%), the highest hole mobilities is 1.65×10^{-3} cm^2 V^{-1} s^{-1} with an average of 1.45×10^{-3} cm^2 V^{-1} s^{-1} which is lower than that P3HT (rr~98%). Moreover, P3HT (rr~85%) film exhibits a weaker diffraction lamellar peak indicating poorer crystallinity and reduced edge-on packing. This might arise from redundant side chain disturbs the conjugation of backbone, resulting in lower hole mobility in the planar direction.

Table 2-1 Summary of BGBC OTFT performance of P3HT (rr~98%) and P3HT (rr~85%)

Polymer	Annealing Temperature (°C)	Mobility (cm^2 V^{-1} s^{-1})	V_{th} (V)	I_{on}/I_{off}
P3HT (rr~98%)	160	1.01×10^{-2}	-10.03	10^4
P3HT (rr~85%)	160	1.65×10^{-3}	-15.17	10^2
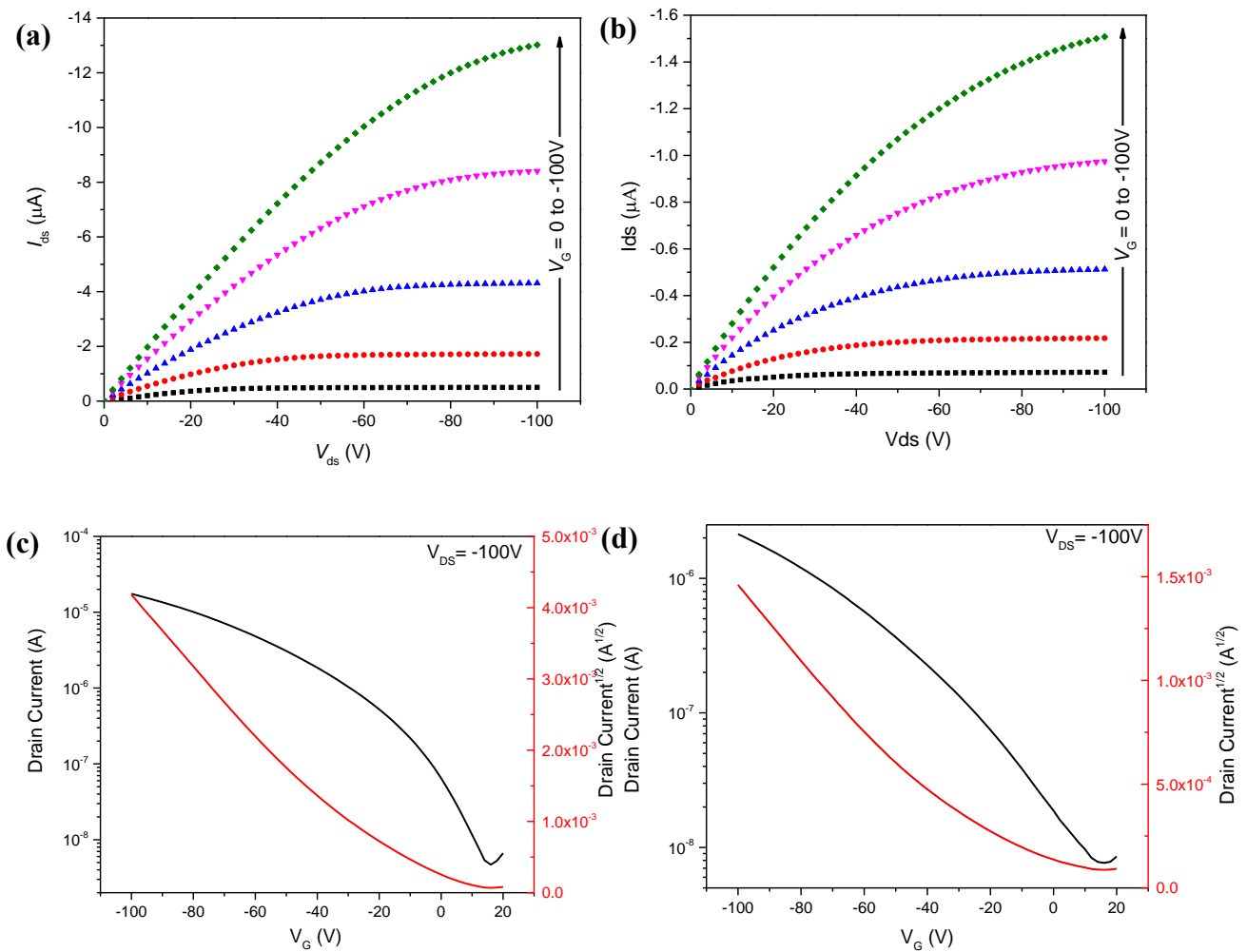
Figure 2-12 The output curves **(a)**, **(b)** and transfer curves **(c)** and **(d)** for OTFTs based on P3HT (rr~98%) and P3HT (rr~85%) annealed at 160 ℃. Device dimensions: channel length (L) = 30 μm; channel width (W) = 1000 μm. V_G valued from 0 to -100 V in the step of -20 V.

2.3 OPV Performances of P3HT(rr~98%):ITIC and P3HT(rr~85%):ITIC

The device configuration was ITO/PEDOT:PSS/P3HT(rr~98%) or P3HT(rr~85%):ITIC/LiF/Al (**Figure 2-13 (a)**). For the photoactive layer, we used optimized condition[73] with the weight ratio 1:1 between donor and acceptor with chloroform as processing solvent. The photovoltaic results are summarized in **Table 2-**

2 and corresponding J-V curves are shown in **Figure 2-13 (b)**. For a comparative study, both P3HT(rr~98%):ITIC and P3HT(rr~85%):ITIC based devices were controlled under optimal condition as mentioned before. In addition, from **Table 2-2**, a PCE of 1.33% was obtained (Voc = 0.52 V, Jsc = 4.69 mA/cm^2, and FF = 0.54) for P3HT(rr~85%):ITIC. In comparison to P3HT(rr~98%):ITIC (Voc = 0.53 V, Jsc = 2.72 mA/cm^2, FF = 0.53 and PCE = 0.76%) (**Table 2-2**), P3HT(rr~85%):ITIC based devices exhibited higher Jsc, resulting in higher PCE, which is also better than the record on paper.
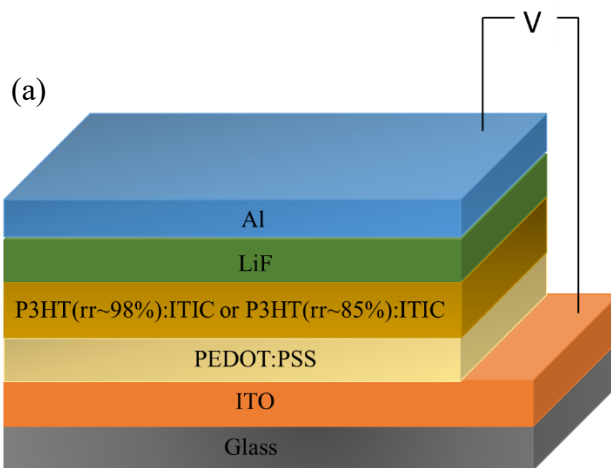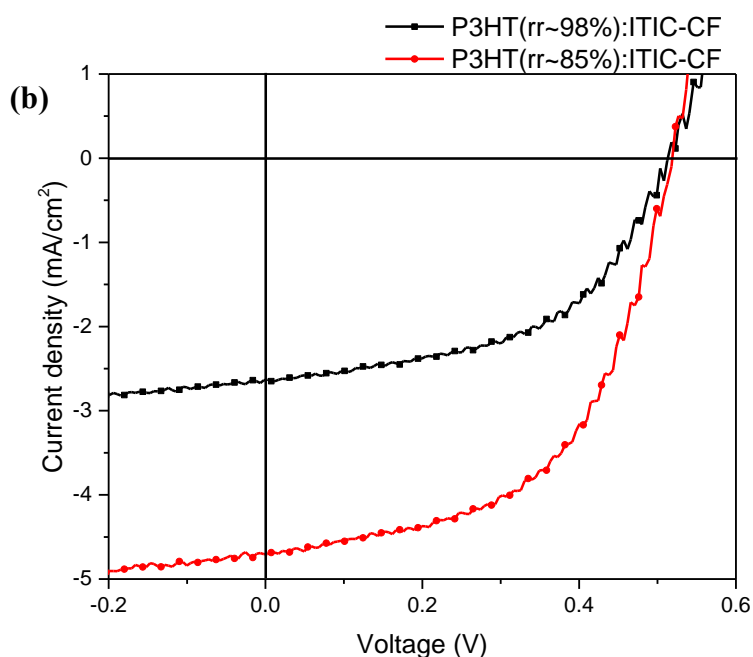
Figure 2-13 (a) Schematic representation of the solar cell device structure, **(b)** the J-V curve based on P3HT(rr~98%):ITIC and P3HT(rr~85%):ITIC under AM 1.5G illumination.

Table 2-2 Summary of the device performance of P3HT(rr~98%):ITIC and P3HT(rr~85%):ITIC.

	Jsc (mA/cm²)	Voc（V）	FF	PCE （%）	Rsh (ohm/cm²)	Rs (ohm/cm²)
P3HT(rr~98%): ITIC-CF	2.72	0.53	0.53	0.76	934	39
P3HT(rr~85%): ITIC-CF	4.69	0.52	0.54	1.31	995	24

To further understand the perfermance of solar cells of P3HT(rr~98%):ITIC and P3HT(rr~85%):ITIC, it is necessary to measure the charge transport properties of the blend films by the space-charge-limited current (SCLC) technique. The electron-only

device was composed of ITO/ZnO/Active layer/LiF/Al while hole-only device consisted of ITO/PEDOT:PSS/Active layer/MoO3/Ag (**Figure 2-14 (a), (b)**). Based on Mott-Gurney equation, the hole and electron mobility was calculated through fitting the J-V curves in the near quadratic region:

$$J = \frac{9}{8}\mu\varepsilon\varepsilon_0\frac{V^2}{L^3}$$

where J is current density, μ is carrier mobility, ε (dielectric constant) is approximately 3 for organic semiconductors, ε_0 is vacuum dielectric constant (8. 85×10^{-12} F/m), V is voltage and L is the thickness of the active layer. The Hole mobilities of neat P3HT (rr~98%) and P3HT (rr~85%) films were determined to be 2.48 × 10^{-4} cm^2 V^{-1} s^{-1} and 2.63 × 10^{-4} cm^2 V^{-1} s^{-1} respectively (**Figure 2-15 (b)** and **Table 2-3**), exhibiting comparable hole transport ability. Interestingly, the hole mobility of P3HT(rr~98%):ITIC film dropped to 1.02×10^{-4} cm^2 V^{-1} s^{-1} while that of P3HT(rr~85%):ITIC film is 2.46×10^{-4} cm^2 V^{-1} s^{-1} (**Figure 2-15 (c)** and **Table 2-3**). Moreover, the electron mobilities of P3HT(rr~98%):ITIC and P3HT(rr~85%):ITIC films are 1.56×10^{-5} cm^2 V^{-1} s^{-1} and 2.60×10^{-5} cm^2 V^{-1} s^{-1}, respectively (**Figure 2-15 (d)** and **Table 2-3**). It is worthy to note that the crucial requirement for high performance OSCs to achieve balanced hole/electron carrier mobilities, demonstrating the ratio between hole and electron mobilities is close to unity.[49,96] The P3HT(rr~98%):ITIC and P3HT(rr~85%):ITIC films exhibited balanced hole/electron mobilities which is required for equal collection (ratio of hole/electron mobilities: 0.65 and 0.94, repectively). However, both hole and elctron mobilities of P3HT(rr~85%):ITIC are higher than that of P3HT(rr~98%):ITIC, which could explain why the Jsc of P3HT(rr~85%):ITIC is almost two times higher than another one.
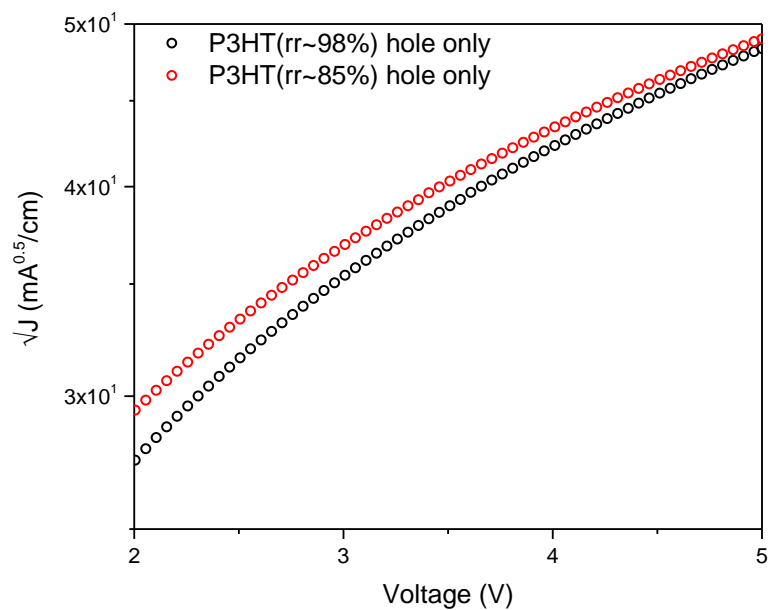
Figure 2-14 The J-V characteristics of the hole-only devices for neat P3HT(rr~98%) and P3HT(rr~85%).
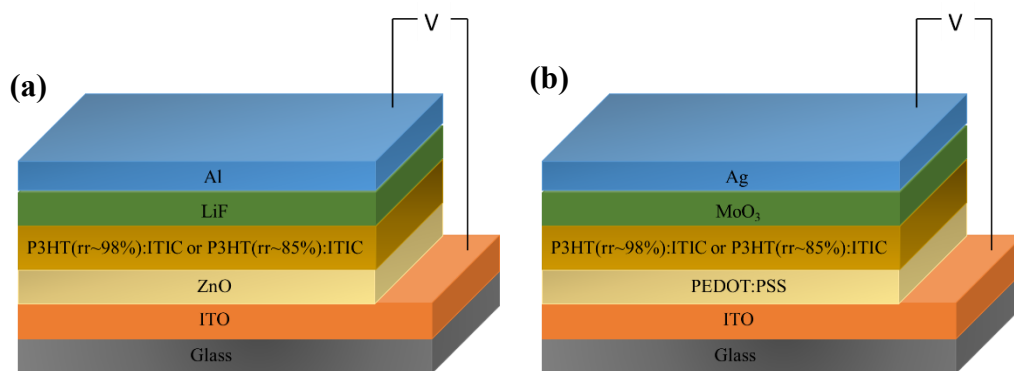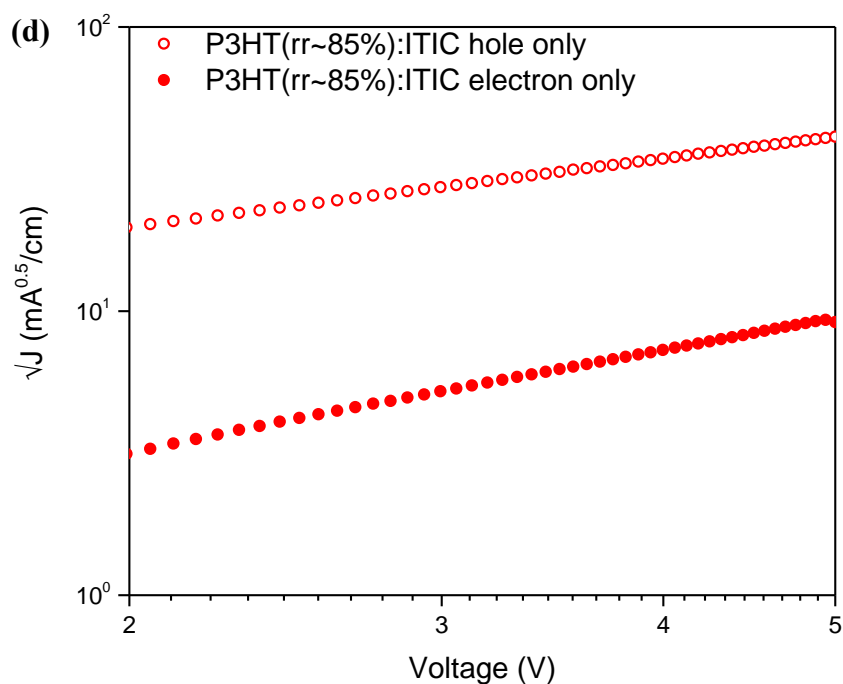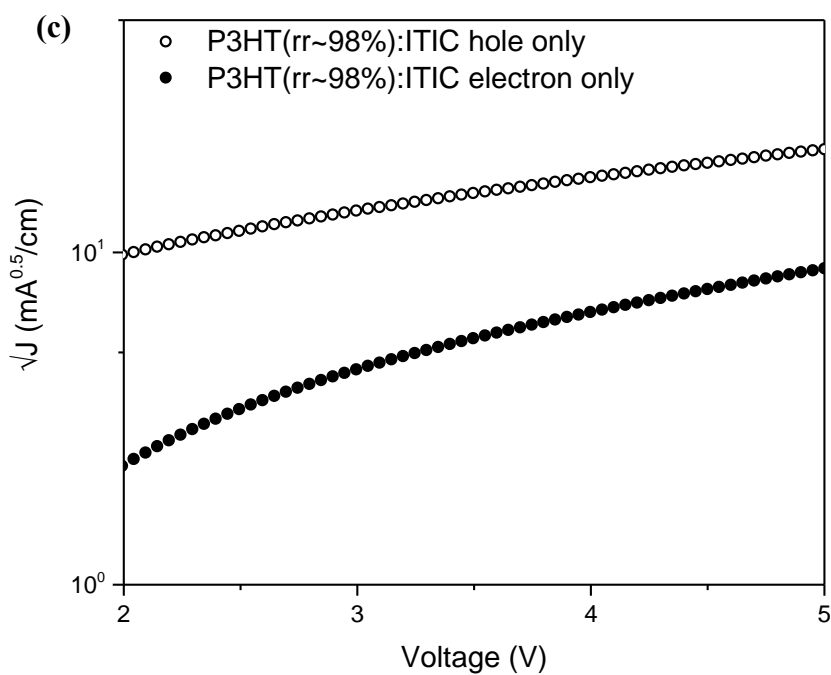
Figure 2-15 Schematic representation of the SCLC devices structure: **(a)** hole-only; **(b)** electron-only. **(c)** the J-V characteristics of the hole-only and electron-only devices for P3HT(rr~98%):ITIC, **(d)** the J-V characteristics of the hole-only and electron-only devices for P3HT(rr~98%):ITIC.

Table 2-3 Summary of the hole and electron mobility of P3HT(rr~98%):ITIC and

P3HT(rr~85%):ITIC.

The external quantum efficiency (EQE) was used to understand the different photocurrent generation efficiencies due to spectral response of devices. **Figure 2-16**

Active layer	P3HT(rr~98%)	P3HT(rr~85%)
Hole mobility ($cm^2 V^{-1} s^{-1}$)	2.63×10^{-4}	2.48×10^{-4}
Active layer	P3HT(rr~98%):ITIC	P3HT(rr~85%):ITIC
Hole mobility ($cm^2 V^{-1} s^{-1}$)	1.02×10^{-4}	2.46×10^{-4}
Electron mobility ($cm^2 V^{-1} s^{-1}$)	1.56×10^{-5}	2.60×10^{-5}

shows the EQE spectra of best devices based on P3HT(rr~98%):ITIC and P3HT(rr~85%):ITIC. Compared with the spectrum of P3HT(rr~98%):ITIC (the maxima of 10.07% at ~ 498 nm), the P3HT(rr~85%):ITIC exhibits greatly enhanced EQE response in the wavelength range of 400 ~ 600 nm with the maxima of 19.6% (at ~ 489 nm) where P3HT absorbs dominantly. Additionally, it is obvious that EQE response of P3HT(rr~85%):ITIC is also higher than that of P3HT(rr~98%):ITIC in wavelength range 600 ~ 750 nm, where ITIC absorbs dominantly. A plausible reason is that the domain size of P3HT(rr~85%) in blend maybe smaller due to the hindrance of side chain, giving better donor/acceptor intermixing at nanometer scale.
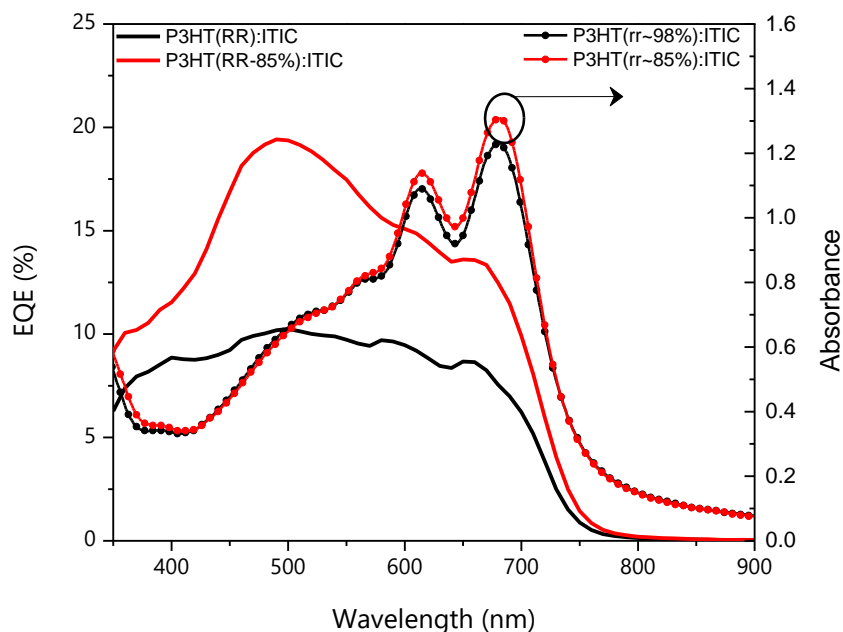
Figure 2-16 EQE curves of PSCs and absorption spectra based on
P3HT(rr~98%):ITIC and P3HT(rr~85%):ITIC.

To further understand the difference between the performance of P3HT(rr~98%):ITIC
and P3HT(rr~85%):ITIC, AFM measurement was used to investigate the nano-
morphologies of the blend films, which were obtained by spin-coated active layer with
chloroform as processing solvent and annealing at 100 ℃ for 10 mins sequentially. As
shown in **Figure 2-17**, the P3HT(rr~85%) shows smoother morphology because
polymer side chains are less ordered leading to weaker aggregation. Moreover,
combined with EQE results, P3HT(rr~85%):ITIC exhibits enhanced current density in
absorption ranges of P3HT and ITIC, demonstrating more efficient charge transport
from active layer to respective electrode. Because of the limited exciton diffusion length,
the ideal domain size is around 10 -20 nm[23] and therefore a coarsened morphology is
detrimental for the performance of device. Therefore, uniform and better mixed surface
morphology could partially explain the higher Jsc in P3HT(rr~85%):ITIC device
because it is favorable for charge separation and transportation.
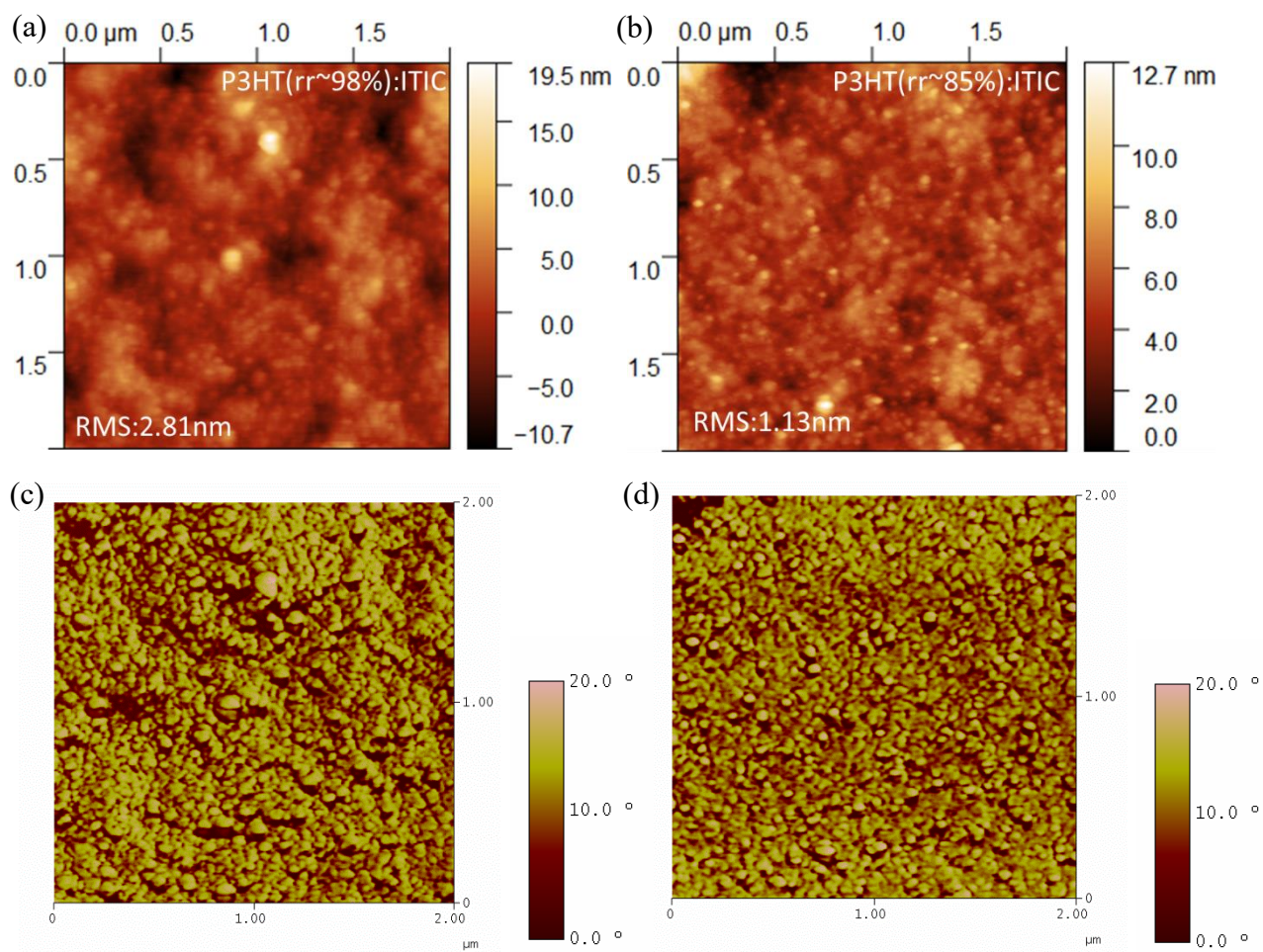
Figure 2-17 Height AFM images of **(a)** P3HT (rr~98%):ITIC **(b)** P3HT (rr~85%):ITIC; phase AFM images of **(c)** P3HT (rr~98%):ITIC and **(d)** P3HT (rr~85%):ITIC. The films were spin-coated on PEDOT: PSS/ITO substrates and were annealed at 160 ℃ for 10 mins.

2.4 Summery and Future Directions

In conclusion, P3HT (rr~85%):ITIC was introduced to increase the interaction between donor and acceptor, which exhibits higher Jsc resulting in better performance. Herein, for the OTFT devices, the P3HT (rr~98%) and P3HT (rr~85%) showed p-type dominant charge transport properties with hole mobility up to 1.01×10^{-2} cm^2 V^{-1} s^{-1} and 1.65×10^{-3} cm^2 V^{-1} s^{-1}, respectively. When the polymers applied to solar cell, a PCE of 1.33% was

obtained based on P3HT (rr~85%):ITIC which is higher than the P3HT (rr~98%):ITIC efficiency published (1.25%). Meanwhile, a PCE of 0.76% based on P3HT (rr~98%):ITIC was obtained under our laboratory conditions. The small difference of HOMO energy level and band gap between P3HT (rr~98%) and P3HT (rr~85%) resulted in similar Voc (0.54 and 0.52 eV respectively) based on P3HT (rr~95%):ITIC and P3HT (rr~85%):ITIC OSCs. The main reason for the optimized performance of P3HT (rr~85%):ITIC is higher Jsc compared with P3HT (rr~98%):ITIC. In AFM images large-scale phase separation with higher RMS roughness (2.81 nm) was found in the P3HT(rr~98%):ITIC blend films, indicating poor miscibility at nanometer scale while P3HT(rr~85%):ITIC film exhibited better morphology (RMS:1.13 nm). Additionally, the hole mobility of P3HT(rr~98%):ITIC film is 1.02×10^{-4} cm^2 V^{-1} s^{-1} while that of P3HT(rr~85%):ITIC film is 2.46×10^{-4} cm^2 V^{-1} s^{-1}. Moreover, the electron mobilities of P3HT(rr~98%):ITIC and P3HT(rr~85%):ITIC films are 1.56×10^{-5} cm^2 V^{-1} s^{-1} and 2.60×10^{-5} cm^2 V^{-1} s^{-1}, respectively. Therefore, charge transport is more efficient from D/A interface to respective electrode, leading to higher Jsc (4.69 mA/cm^2) of P3HT (rr~85%):ITIC device while Jsc in P3HT (rr~85%):ITIC is (2.97 mA/cm^2). Moreover, P3HT with different regioregularities, such as 70% or 90%, are required to do a more systematic comparative study of OSC performance.

2.5 Experimental Section

2.5.1 Materials and Characterization

P3HT (rr~98%; Mw = 44 kDa, PDI:1.44) and P3HT (rr~85%; Mw = 25 kDa, PDI:1.45) were purchased from 1-materials. Transmission XRD measurements were carried out on a Bruker Smart 6000 CCD 3-50 circle D8 diffractometer with a Cu RA (Rigaku) X-ray source (λ = 0.15406 nm) and the polymer flakes stacked between two Mylar substrates. NMR data was recorded with a Bruker DPX 300 MHz spectrometer with chemical shifts relative to tetramethyl silane (TMS, 0 ppm). Atomic force microscopy

(AFM) images were taken on polymer thin films spin-coated on the DDTS-modified SiO2/Si substrates with a dimension 3100 scanning probe microscope.

According to the NMR results (**Figure 2-18**), the signals in aromatic region of P3HT (rr~98%) and P3HT (rr~85%) can be observed at 6 ~ 7 ppm. The ratio between the head to head and head to tail arrangement can be calculated from the methylene peaks, which could be observed at 2.5 ~ 3.0 ppm. The HT arrangement is at the range of 2.75~2.8 ppm while the HH arrangement is around 2.5~2.6 ppm.
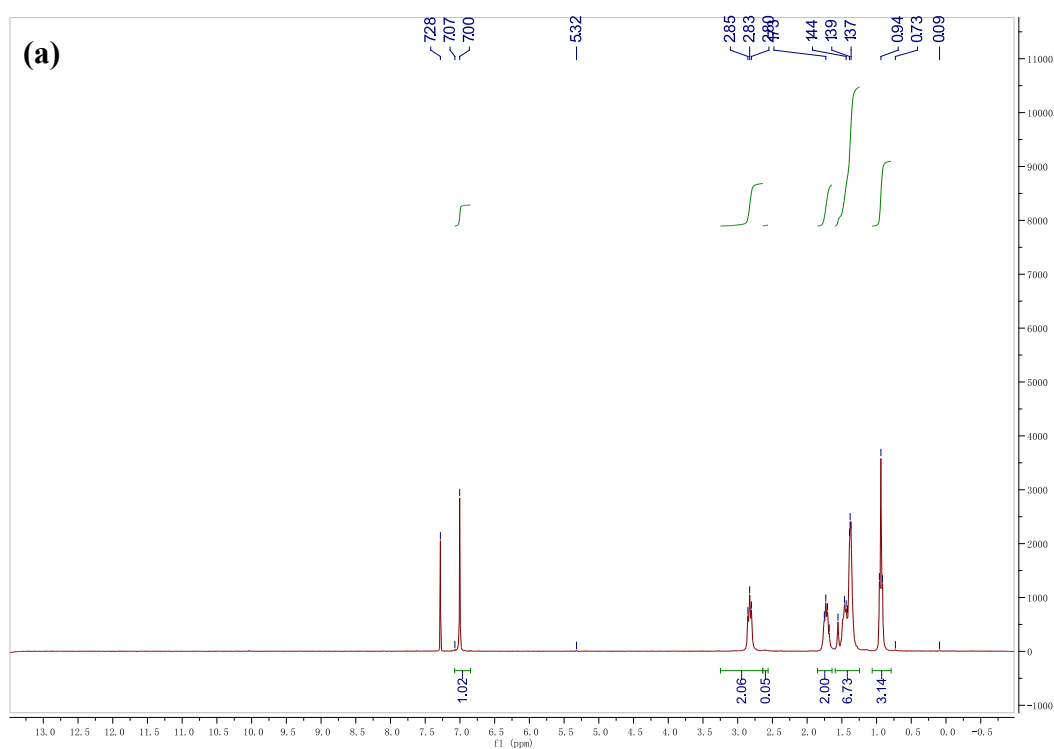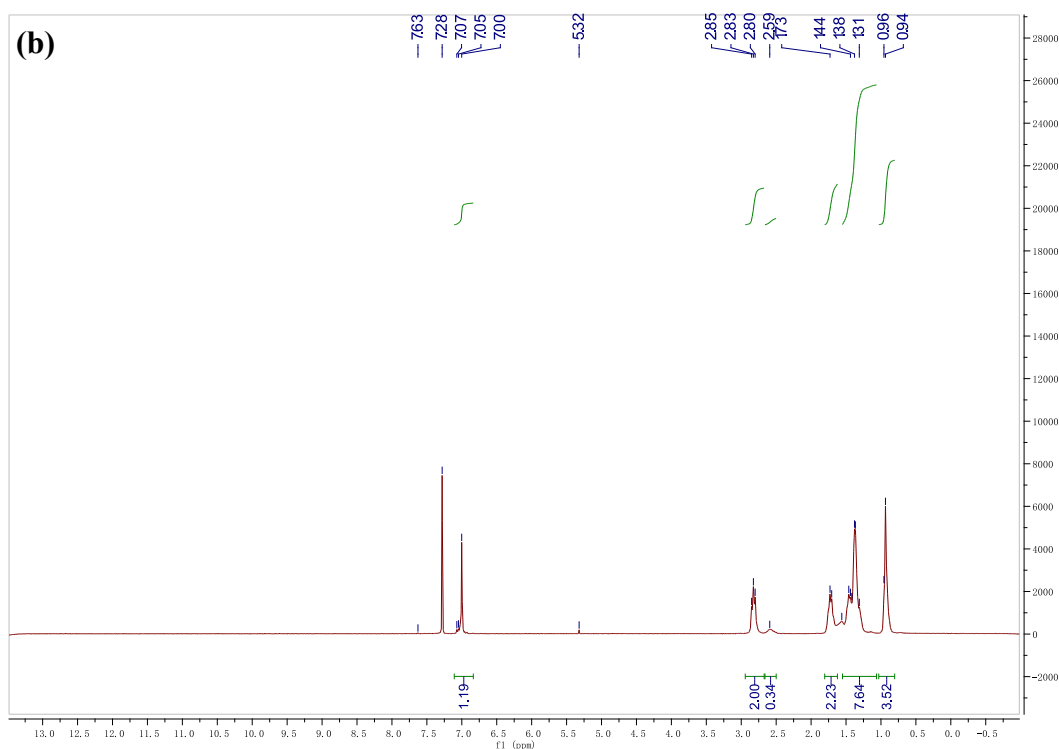
Figure 2-18 1H NMR spectra of **(a)** P3HT (rr~98%) and **(b)** P3HT (rr~85%).

2.5.2 Fabrication and Characterization of OTFT Devices

The hole mobility of polymer was measured by OTFT devices with the bottom-gate bottom-contact (BGBC) configuration. The preparation and fabrication procedure of OTFT device is as follows. Through conventional photolithography and thermal deposition, the gold source and drain pairs were patterned on a heavily n-doped SiO2/Si wafer with ~ 300 nm-thick SiO_2. After cleaning with acetone and isopropanol in an ultra-sonic bath each for 20 min, the substrates were dried by nitrogen and treated with air plasma for 2 min. In next step, the substrates were immersed in a solution of dodecyl trichlorosilane (DDTS) in toluene (3 % DDTS in toluene) at room temperature for 20 min. The substrate was rinsed with toluene and dried by nitrogen gas. Then a polymer film (~ 40 nm) was deposited onto the substrate by spin-coating at 3000 rpm for 60 s with a polymer solution in chloroform (5 mg/ml).

Configurations of four types of single-gate OTFTs structures: **a)** bottom-gate, top-contact (BGTC), **b)** bottom-gate, bottom-contact (BGBC),

All the OTFT devices have a channel width (W) of 1000 μm and a channel length (L) of 30 μm and and were characterized by an Agilent B2912A Semiconductor Analyzer. The hole and electron mobilities are calculated in the saturation regime according to the following equation:

$$I_{DS} = \frac{\mu C i W}{2L}(V_G - V_T)^2$$

where I_{DS} is the drain-source current, μ is charge carrier mobility, Ci is the gate dielectric layer capacitance per unit area (~ 11.6 nF cm^{-2}), L is the channel length (30 μm), V_G is the gate voltage, V_T is the threshold voltage, and W is the channel width (1000 μm).

2.5.3 Fabrication and Characterization of Conventional Organic Solar Cells

All the solar cells of conventional configuration were fabricated with ITO/PEDOT: PSS/Active layer/LiF/Al shown in **Figure 2-9**. The ITO glass substrates were immersed and sonicated in deionized water, acetone for 20 min respectively. Then the ITO glass substrates were placed on aluminum foil and cleaned by Q-tips with acetone. Then the substrates were placed in the ultra-sonic bath for 20 min in IPA. The substrates were dried under a nitrogen flow and treated with air plasma cleaner. A ~40nm layer of PEDOT: PSS (Al 4083) was deposited by spin-coating at 4000 rpm and dried subsequently at 150 °C for 20 min in air. Then the substrates were transferred to a nitrogen glove box and the active layer was spin-coated onto the PEDOT: PSS layer. The concentration of solution and spin speed both could control the thickness. For the thermal treatment, the substrates were placed onto the hotplate and annealed for 10 min in nitrogen atmosphere. Finally, a ~1 nm layer of LiF and a ~100nm layer of Al electrode were deposited in vacuum onto the substrate at P ≈ 5.0 × 10^{-6} Pa. The active

area was 0.0574 cm^2. The current density–voltage (J-V) characteristics of the solar cells were measured on an Agilent B2912A Semiconductor Analyser with a ScienceTech SLB300-A Solar Simulator. The light source was A 450 W xenon lamp with an air mass (AM) 1.5 filter.

Chapter 3. Characterization of Oxime-based Polymers for Organic Solar Cells

3.1 Introduction

In Chapter 2, we successfully improve the performance of P3HT:ITIC solar cell through enhancing the interactions between donor and acceptor. In order to further improve performance, different regioregularities of P3HT can be applied into OSCs. However, different regioregularities of P3HT are relatively difficult to get due to the requirement of accurate control of temperature and catalysts.[93] Besides, from contour plot showing the calculated energy-conversion efficiency (**Figure 2-2 (b)**), tuning the energy levels of donor polymers is also a promising direction to obtain higher performance. On the other hand, ITIC, which showed strong and broad absorption, good electron transport ability and and good miscibility with polymer have been widely studied with extraordinary OSC performances. Recently, by applying polythiophene derivatives and ITIC into OSCs, Bin[66] fabricated solar cell with J71:ITIC and got a PCE of 11.4% (**Figure 3-1 (a)**). Furthermore, Li [97] introduced a new donor polymer (PTFD) with acceptor (IT-IC), obtaining PCE over 10% (**Figure 3-1 (b)**).

(a)

44

(b)

PTFB-O   R=2-decyltetradecyl
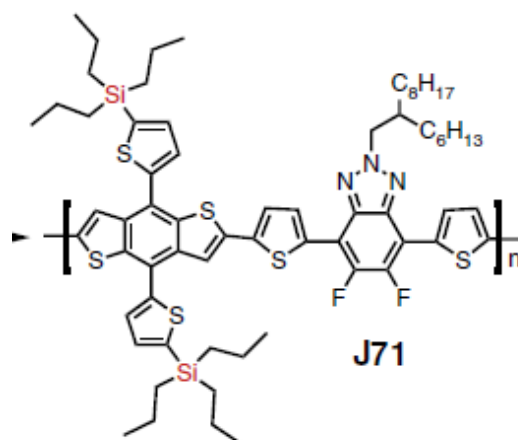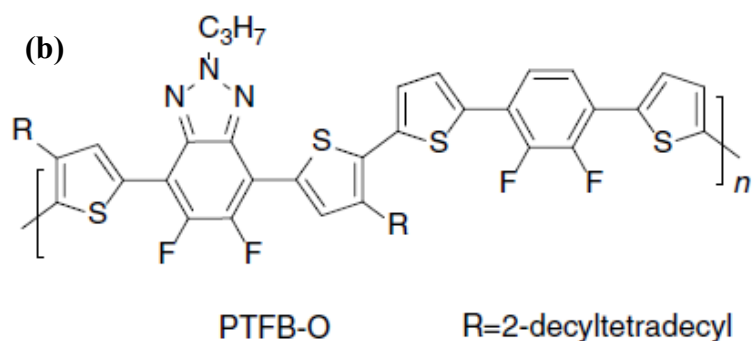
Figure 3-1 Chemical strictures of **(a)** J71[66] **(b)** PTFB-O[97]

Herein, our group designed an electron withdrawing (oxime) group as side chain to form D (main chain) -A (side chain) donor polymer and chemical structures of two isomeric polymers (PTOBT-1 and P-TOBT-2) are shown in **Figure 3-2**. Compared with donor polymers with high-performance mentioned before, PTOBT-1 and P-TOBT-2 exhibited much simpler synthetic route and lower cost. Furthermore, P3HT derivatives with electron withdrawing (oxime) group as side chains may lower the HOMO energy and band gap levels which is beneficial for achieving higher Voc and more light absorption. Therefore, to further explore the needs for low-cost and high performance, it is worthy to evaluate these two isomers for OSCs.

The synthesis of donor polymers and OTFT performance measurement were completed by Keqiang He in our group. The AFM, EQE and XRD were measured by Pankaj Kumar and Marwa Abd-Ellah. And the main work of mine is the fabrication of solar cell to improve the PCE and stability through the evaluations of OTFT, XRD and AFM,

45

etc.
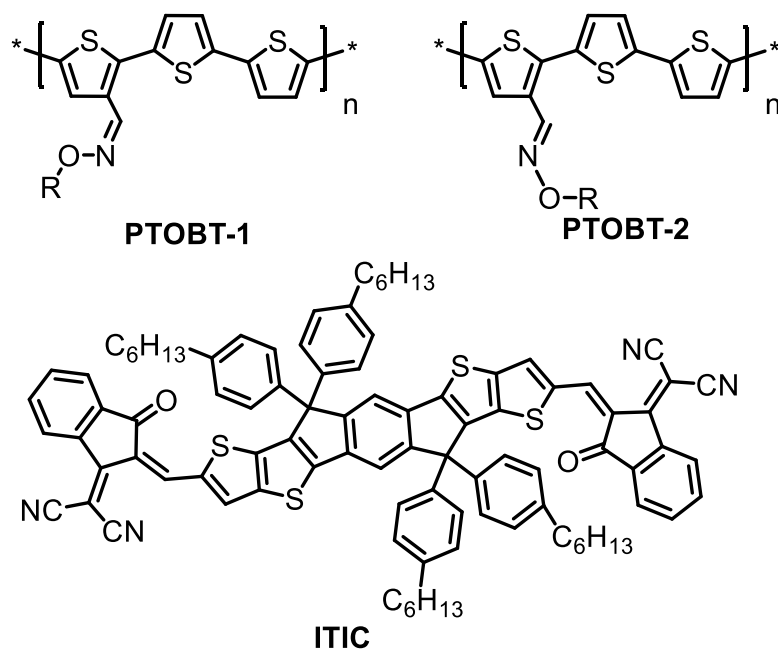
Figure 3-2 Chemical structure of P-TOBT-1, P-TOBT-2 and ITIC.

3.2 Characterization of P-TOBT-1 and P-TOBT-2

3.2.1 Characterization of P-TOBT-1 and P-TOBT-2 by UV-Vis, PL, CV and XRD

The UV-Vis absorption spectra of P-TOBT-1, P-TOBT-2, ITIC, P-TOBT-1:ITIC and P-TOBT-2:ITIC in thin films are shown in **Figure 3-3 (a)** and **(b)**. In solution, the maximum absorption wavelength (λ_m) of P-TOBT-1 and P-TOBT-2 are 543 nm and 597 nm respectively. In thin films, the P-TOBT-1 showed single absorption peak ($\lambda_m = 541$ nm) while the P-TOBT-2 exhibited absorption peak at 552 nm with shoulder peak (585 nm), suggesting the aggregation in solid state. For the blend of donor polymer and ITIC, the spectra showed the complementary profile of absorption, ranging from 450 nm to 750 nm, which is beneficial for their light harvesting property.
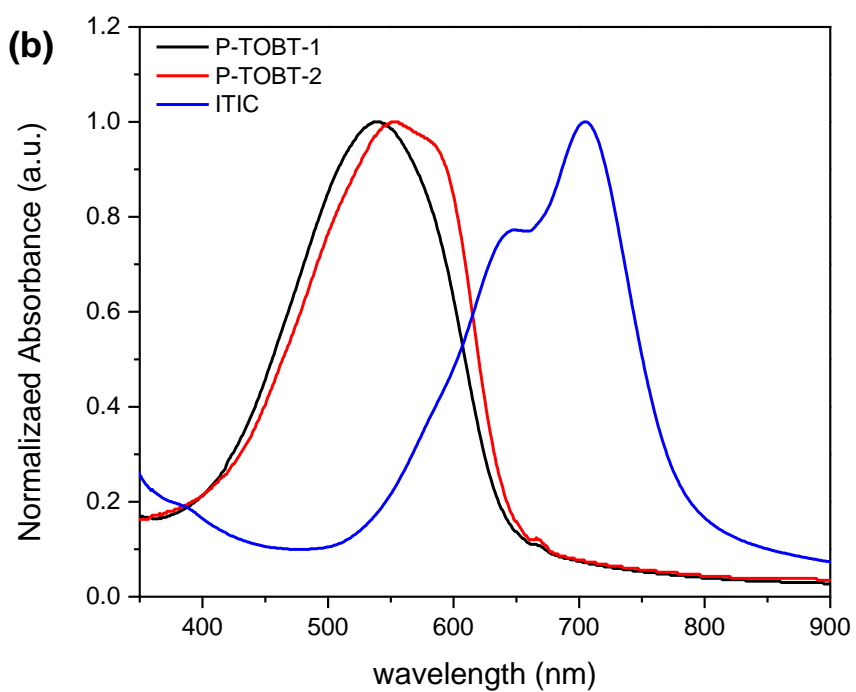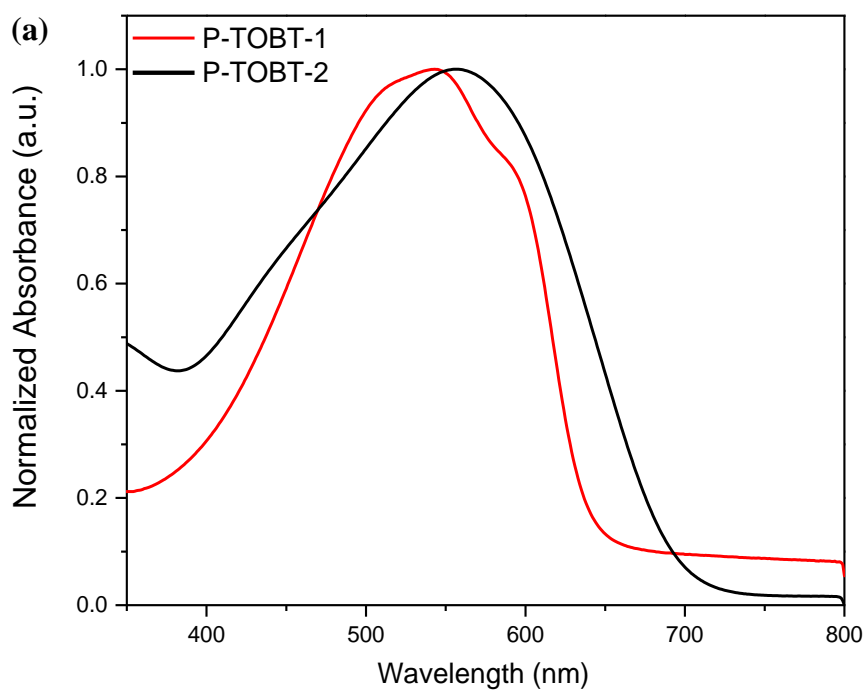
Figure 3-3 (a) Normalized UV-vis absorption spectra of P-TOBT-1, P-TOBT-2 in

solution (chloroform), **(b)** Normalized UV-vis absorption spectra of P-TOBT-1, P-TOBT-2, ITIC

Cyclic voltammetry (CV) was used to investigate the electrochemical property of both P-TOBT-1 and P-TOBT-2 polymers as shown in **Figure 3-4 (a)** and **Table 3-2**. Unlike the high-lying HOMO level of P3HT (-5.05 eV) [68,98], the oxidative onset potentials showed that the HOMO levels of P-TOBT-1 and P-TOBT-2 values are -5.43 eV and -5.44 eV respectively. Meanwhile, the LUMO levels were calculated from HOMO energy levels and the band gaps were obtained by the onset of the UV-vis spectra, which are -3.48 eV and -3.51 eV, respectively. As shown in **Figure 3-4 (a)**, the differences between LUMO energy levels of ITIC and HOMO energy levels of P-TOBT-1 or P-TOBT-2 are 1.56 eV and 1.57 eV respectively which is beneficial to obtain higher Voc. Additionally, the LUMO levels of P-TOBT-1 and P-TOBT-2 are 0.34 eV and 0.33 eV, respectively, higher than that of ITIC, so that the driving force can overcome the binding energy for effective exciton dissociation.
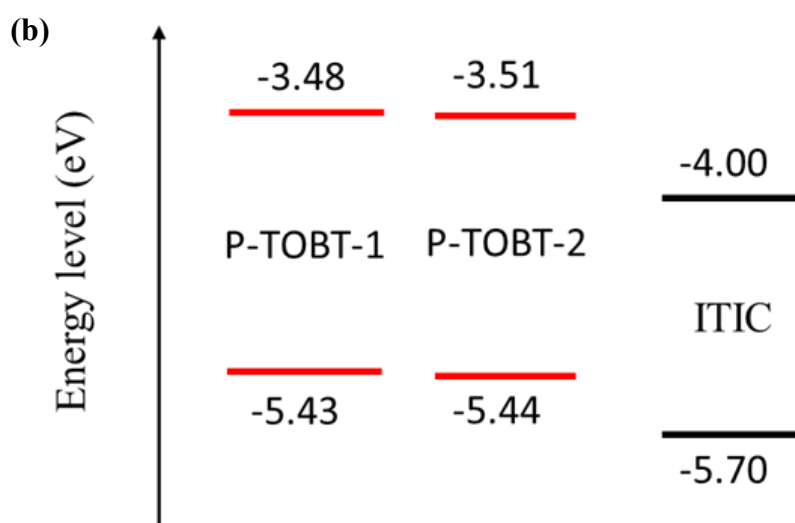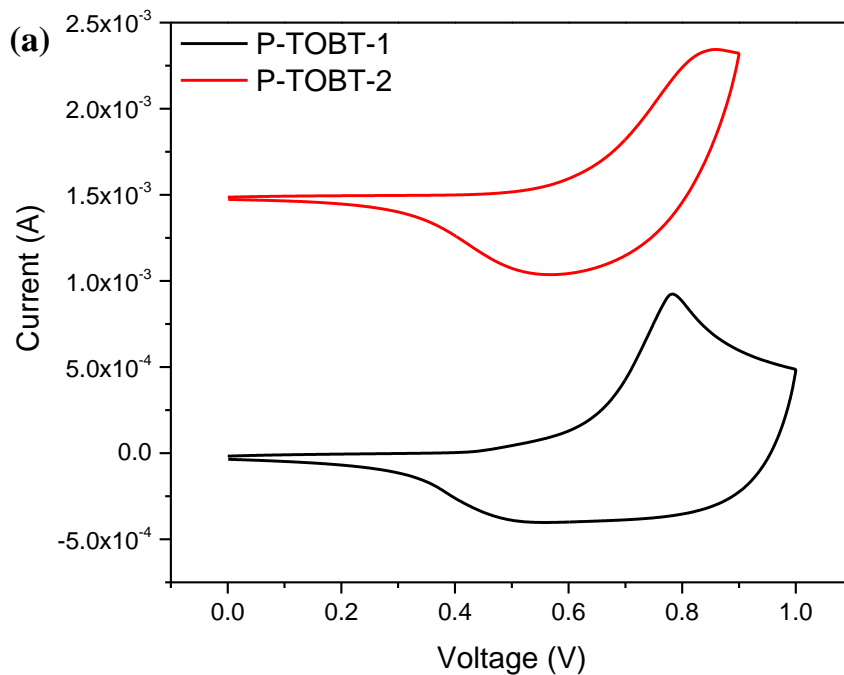
Figure 3-4 (a) the CV diagram of P-TOBT-1 and P-TOBT-2 at a scan rate of 0.1 V/s. The electrolyte was 0.1 M tetrabutylammonium hexafluorophosphate in anhydrous acetonitrile, **(b)** The comparison of the HOMO/LUMOs of P-TOBT-1, P-TOBT-2 and ITIC.

The photoluminescence (PL) measurement was carried out to investigate the efficiency of dissociation of excitons, which is the first step of current generation. It is worthy to note that both polymers were excited at 500 nm, where is not the exact absorption peak of polymer but the lowest absorption of ITIC, so that we could ignore the photoluminescence generated by ITIC phase. Therefore, 500nm was chosen as the excitation wavelength for both polymers. As shown in **Figure 3-4**, the PLQE of PTOBT-1 and PTOBT-2 blended with ITIC were 96% and 97%, respectively. Meanwhile the PLQE of ITIC with the introduction of PTOBT-1 and PTOBT-2 were slightly lower, 81% and 77% respectively. The reason why the PLQE were lower may be that the differences between LUMO energy levels of donor and acceptor are relatively small (0.27 eV and 0.26 eV, respectively). Besides, larger ITIC grain size may also lead to the lower PLQE because that electrons, which generated in ITIC phase far from interface, may undergo radiative emissions relaxing from the excited states to ground states. Furthermore, the PLQE of ITIC blended with P-TOBT-1 was lower than PLQE of ITIC blended with P-TOBT-2, which may be caused by the grain size of ITIC in P-TOBT-1:ITIC was relatively smaller than that in P-TOBT-2:ITIC. The relatively high quenching efficiencies exhibit that almost excitons in both donor and acceptor could be separated into free carriers.
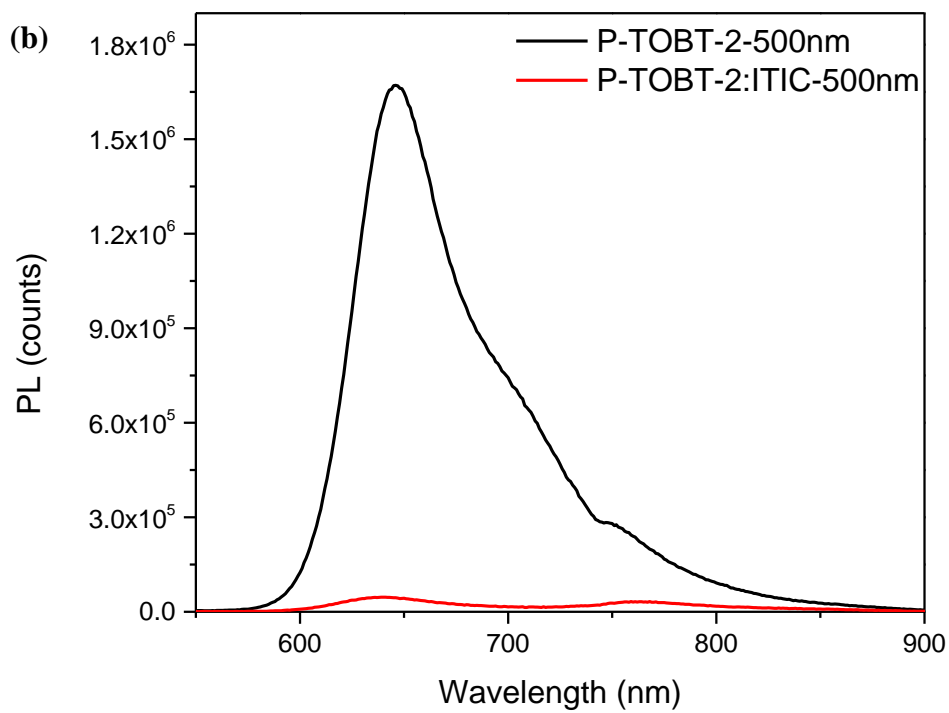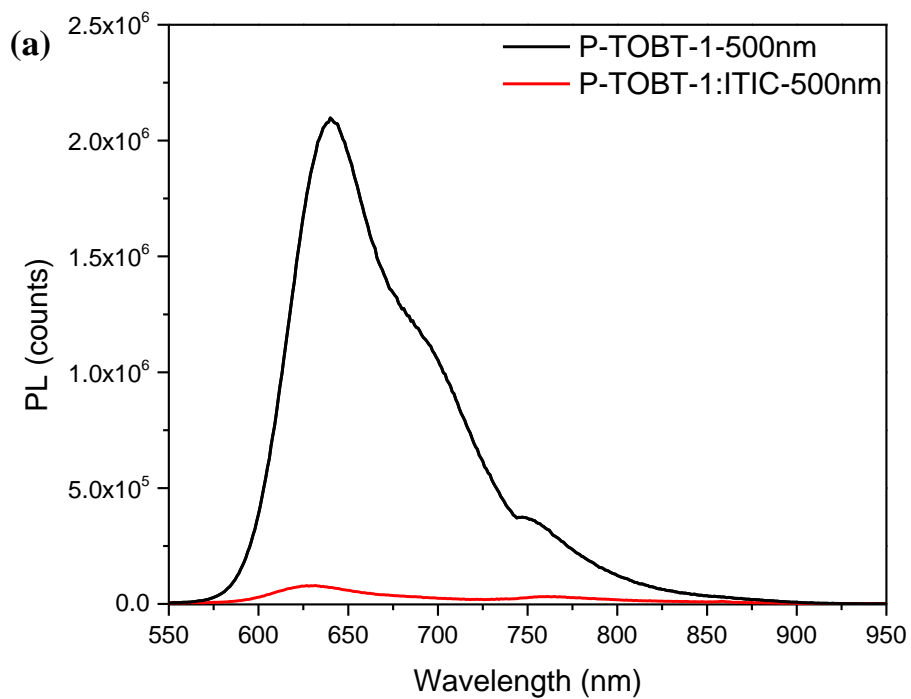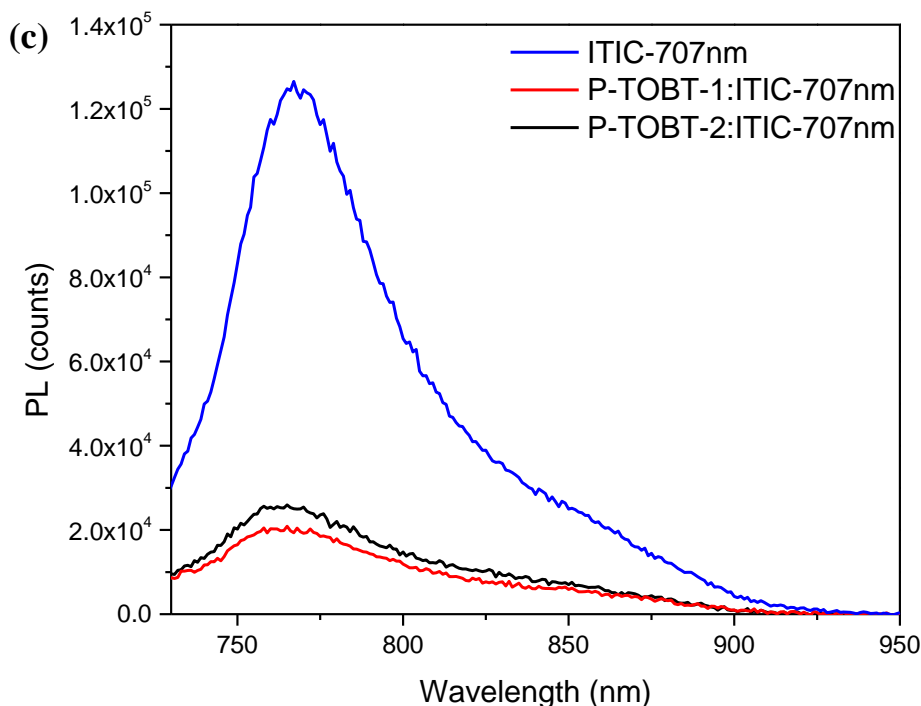
Figure 3-5 (a) Photoluminescence spectra of neat P-TOBT-1and blends of P-TOBT-1:ITIC, **(b)** photoluminescence spectra of neat P-TOBT-2 and blends of P-TOBT-2:ITIC, employing an excitation wavelength at 500 nm, **(c)** neat ITIC and blends of P-TOBT-1:ITIC and P-TOBT-2:ITIC, employing an excitation wavelength at 707 nm.

Reflective X-ray diffraction (XRD) was carried out to investigate the microstructures (**Figure 3-7** and **Figure 3-6**). There are no appreciable long-range order diffraction peaks observed by the XRD graphs based on P-TOBT-1 and P-TOBT-2 neat films, indicating poor crystallinity at room temperature. However, after annealing at 100 ℃ for 10 mins, two peaks were found which can be assigned to (100) and (200) in both neat polymer films, demonstrating the polymers edge-on arrangement and thermal treatment could improve the crystallinity. The d-spacings for P-TOBT-1 and P-TOBT-2 were 2.59 nm ($q_z = 0.24$ Å^{-1}) and 2.40 nm ($q_z = 0.26$ Å^{-1}), respectively. On the other hand, the P-TOBT-1:ITIC and P-TOBT-2 blend films exhibit peaks of lamella packing

even at room temperature with the d-spacing of 2.23 nm (q_z = 0.28 Å^{-1}) and 2.10 nm (q_z = 0.29 Å^{-1}), indicating that the ITIC could facilitate the crystallinity of donor polymer. After annealing at 100 °C for 10 mins, the diffraction peaks became obvious with respect to the d-spacing of 2.48 nm (q_z = 0.25 Å^{-1}) and 2.23 nm (q_z = 0.28 Å^{-1}) which may be caused by the rearrangement of side chains. The diffraction intensity of P-TOBT-2:ITIC films was much lower than that of P-TOBT-1:ITIC. This may be caused by the lower regioregularity of P-TOBT-2 which contains both Z and E configurations.
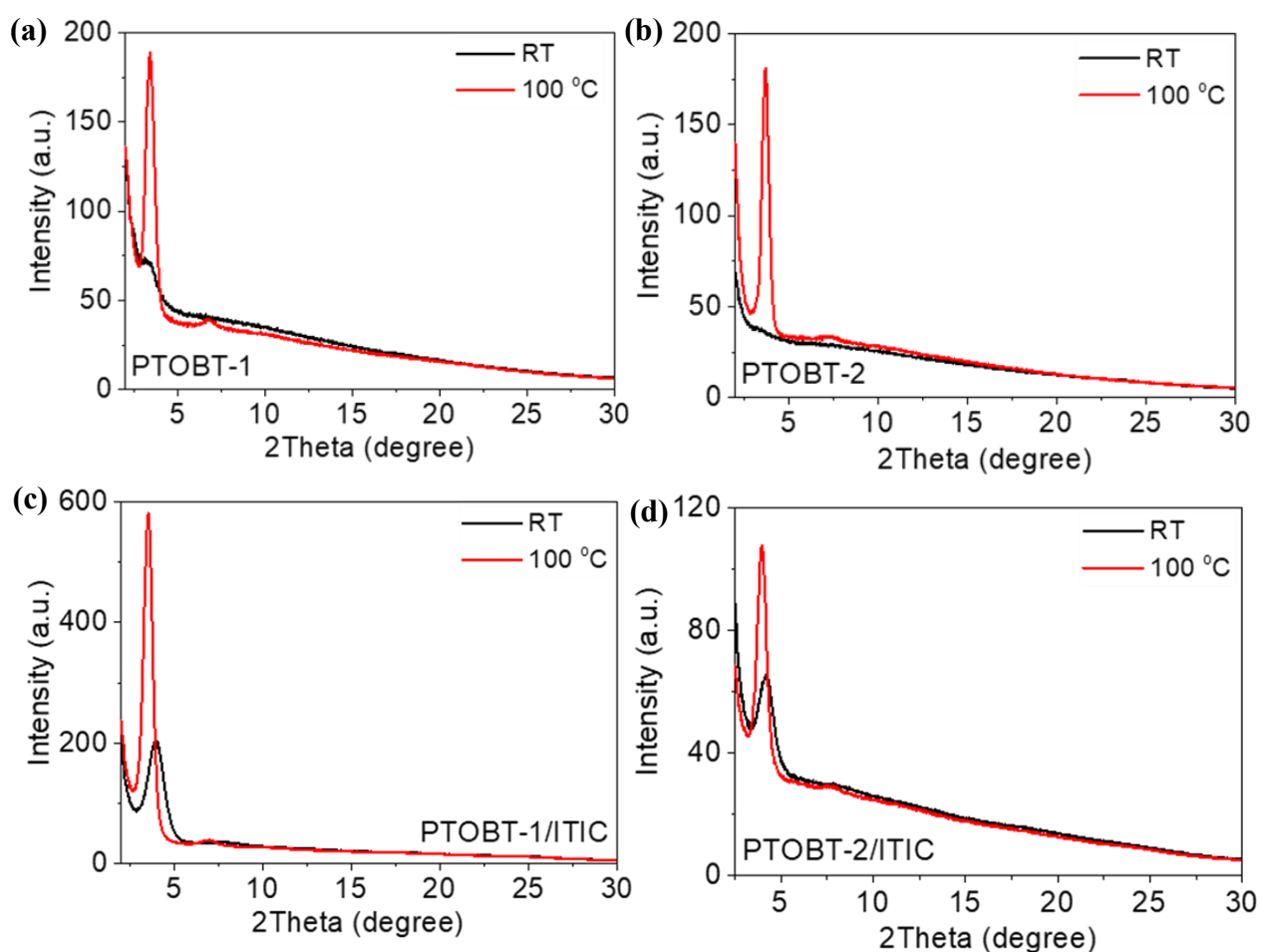
Figure 3-6 The out of plane XRD patterns of pure **(a, b)** and blend **(c, d)** thin films of PTOBT-1 (a, b) and PTOBT-2 (c, d) at room temperature and annealing at 100 ℃.
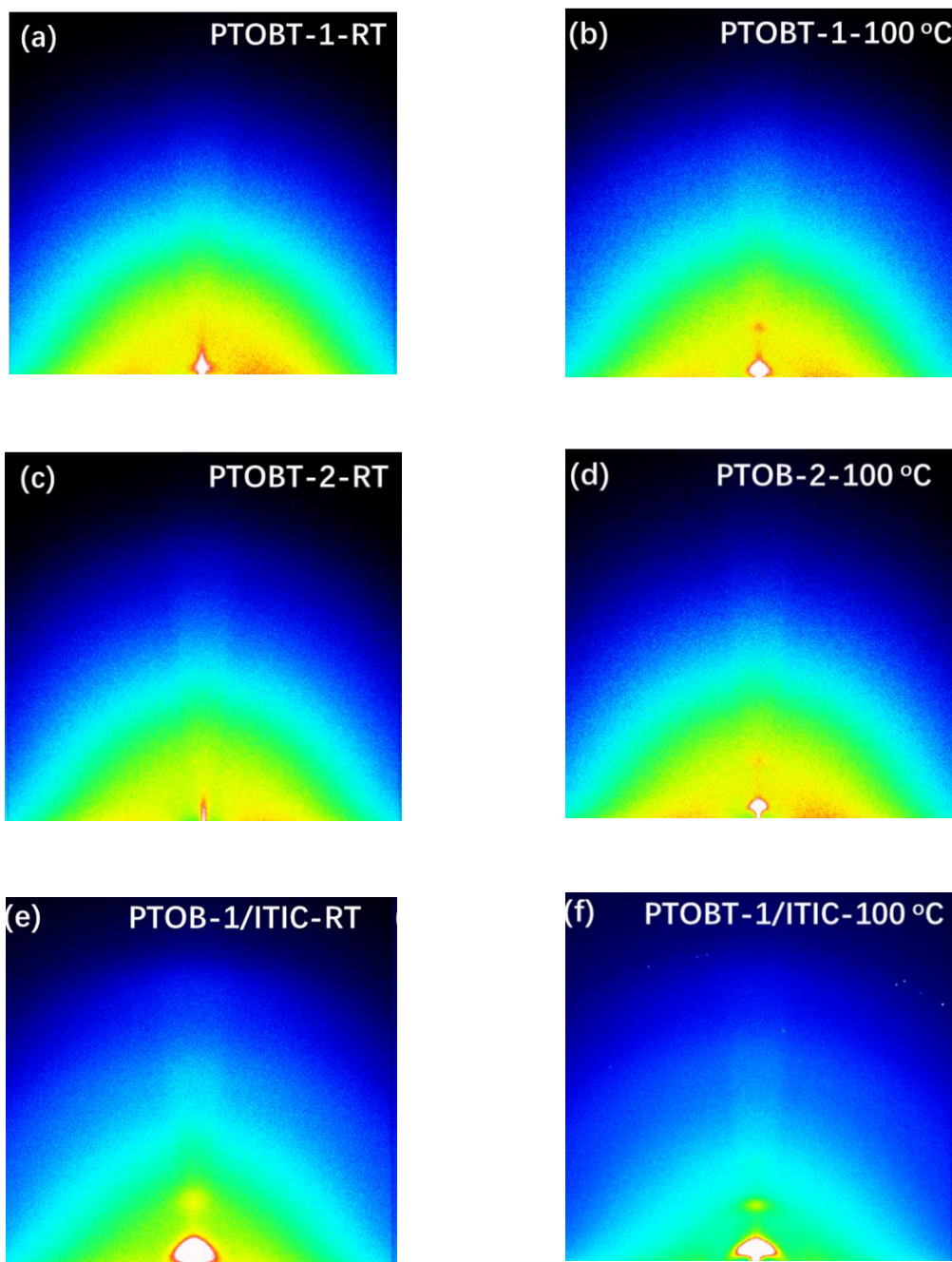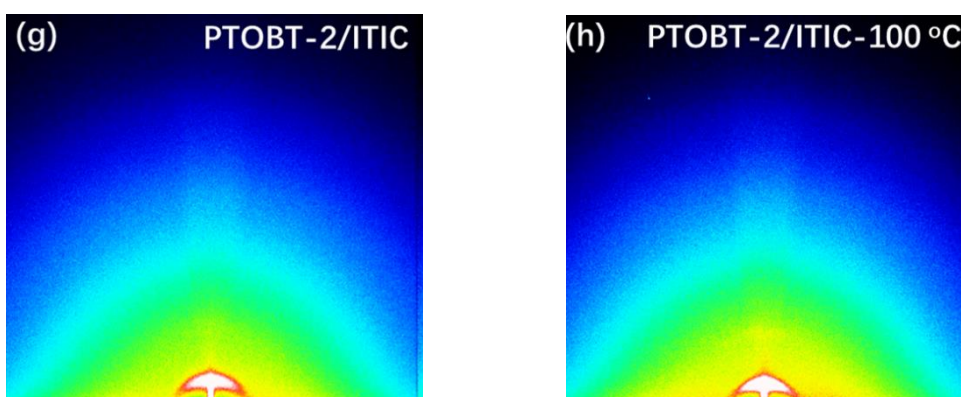
Figure 3-7 GIWAXS scans of P-TOBT-1, PTOBT-2 , P-TOBT-1:ITIC and P-TOBT:ITIC films under room temperature and annealing at 100 °C on DDTS-modified SiO$_2$/Si substrates.

3.2.2 OTFT Performance of P-TOBT-1 and P-TOBT-2

The properties of P-TOBT-1 and P-TOBT-2 as channel semiconductors were evaluated in BGBC OTFT devices fabricated on DDTS modified SiO$_2$/Si wafer substrates. The OTFT fabrications and characterizations are shown in section 2.5.2. Both polymers exhibited p-type charge transport behavior (**Table 3-1** and **Figure 3-8**). For devices based on P-TOBT-1, the best overall performance with hole mobility of 1.64×10^{-2} cm^2 V^{-1} s^{-1} was obtained under 150°C annealing for 10 mins which is around 10 times higher than that without thermal treatment. However, annealing at relatively higher temperature of 200°C did not further improve the device performance. Based on the devices of P-TOBT-2, the highest hole mobility achieved 1.52×10^{-2} cm^2 V^{-1} s^{-1} for the 200 °C annealed polymer film. It should be noticed that the threshold voltage (V_T) was close to 0 V, demonstrating a matched energy levels between gold electrode and polymer layer. Therefore, the square root of the drain current and gate voltage has linear relationship. Furthermore, it is evident that P-TOBT-1 exhibited better charge transporting properties in the parallel direction which may caused by the higher crystallinity.

Table 3-1 Summary of BGBC OTFT performance of P-TOBT-1 and P-TOBT-2.

Compound	Process (°C)	μ_{avg} ($cm^2V^{-1}s^{-1}$)	μ_{max} ($cm^2V^{-1}s^{-1}$)	V_{T-avg} (V)	$I_{on/off}$
PTOBT-1	rt	$9.25\times10^{-4} \pm 1.46\times10^{-4}$	1.03×10^{-3}	-13	10^4
	50	$2.01\times10^{-3} \pm 1.24\times10^{-4}$	2.11×10^{-3}	-13	10^4
	100	$1.07\times10^{-2} \pm 9.50\times10^{-4}$	1.23×10^{-2}	-20	10^5
	150	$1.50\times10^{-2} \pm 8.05\times10^{-4}$	1.64×10^{-2}	-2	10^5
	200	$1.15\times10^{-2} \pm 8.34\times10^{-4}$	1.25×10^{-2}	-4	10^5
PTOBT-2	rt	$3.60\times10^{-3} \pm 1.88\times10^{-4}$	3.80×10^{-3}	-6	10^4
	50	$4.54\times10^{-3} \pm 7.59\times10^{-4}$	5.29×10^{-3}	-1	10^4
	100	$8.20\times10^{-3} \pm 2.69\times10^{-3}$	1.09×10^{-2}	-3	10^5
	150	$9.10\times10^{-3} \pm 2.49\times10^{-3}$	1.24×10^{-2}	-7	10^5
	200	$1.21\times10^{-2} \pm 2.48\times10^{-3}$	1.52×10^{-2}	-10	10^5
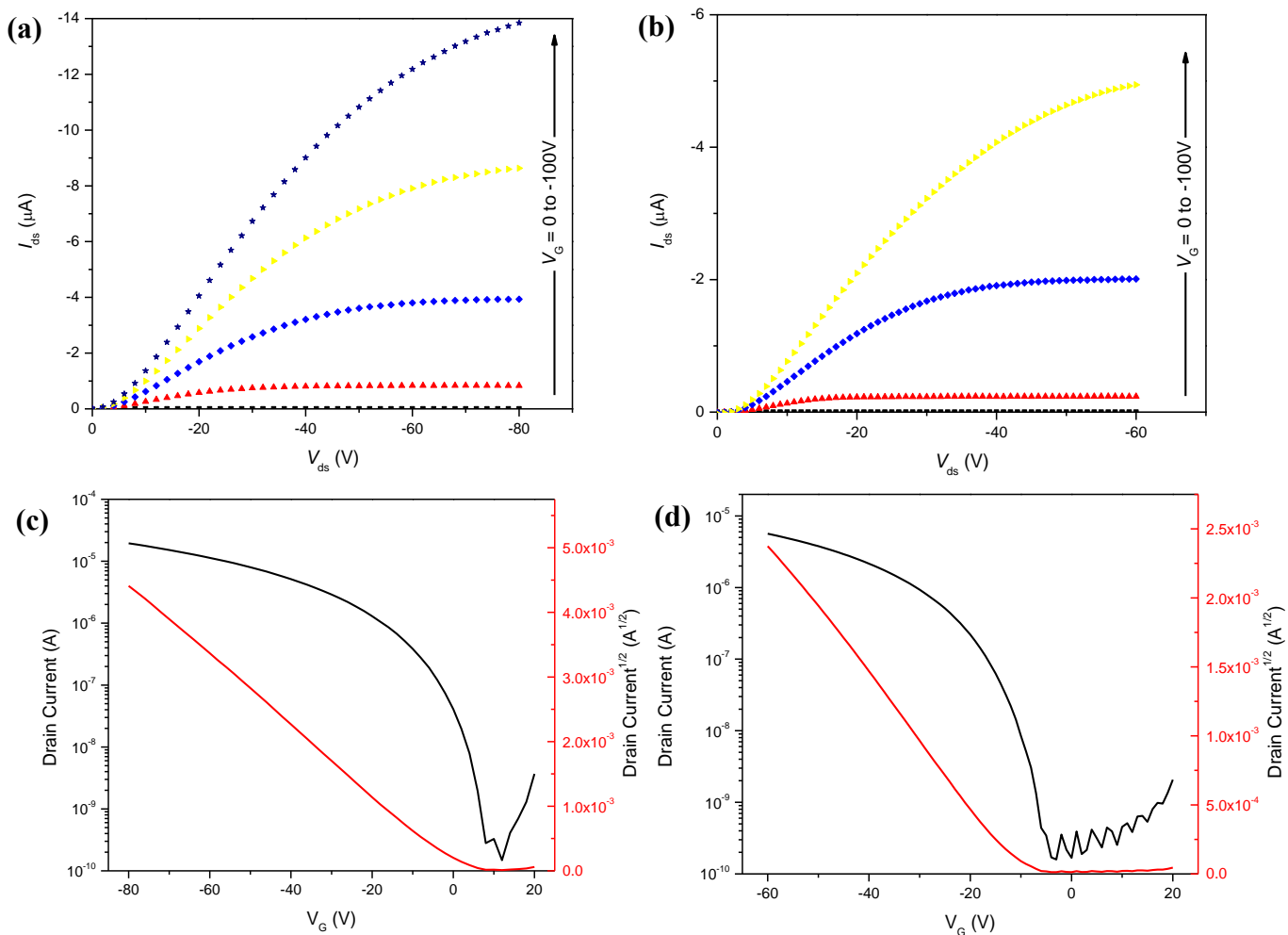
Figure 3-8 The output curves **(a)**, **(b)** and thansfer curves **(c)**, **(d)** for OTFTs based on P-TOBT-1 and PTOBT-2 annealed at 160 ℃. Device dimensions: channel length (L) = 30 μm; channel width (W) = 1000 μm. V_G valued from 0 to -100 V in the step of -20 V in output curves.

3.3 OPV performances of P-TOBT-1:ITIC and P-TOBT-2:ITIC

3.3.1 OPV Performance and Characterization for P-TOBT-1:ITIC and P-TOBT-2:ITIC

The solar cell results based on P-TOBT-1:ITIC and P-TOBT-2:ITIC in conventional structure are shown in **Figure 3-9** and **Table 3-2**. In this system, the devices were

processed at room temperature and annealed at 100 °C before evaporation of electrode. After annealing at 100 °C, The efficiency of the P-TOBT-1:ITIC solar cells decreased, compared with that without thermal treatment (from 6.03% to 3.30%). Additionally, the highest efficiency achieved 6.03% as Jsc reached 13.54 mA/cm^2. On the other hand, The I-V curve of P-TOBT-2:ITIC showed s-shape, indicating the possibility of poor contact between active layer and charge transport layer or unbalanced electron/hole mobilities. Furthermore, after annealing at 100 °C for 10 mins, the device showed no performance, which may be due to the poor contact after the annealing process.
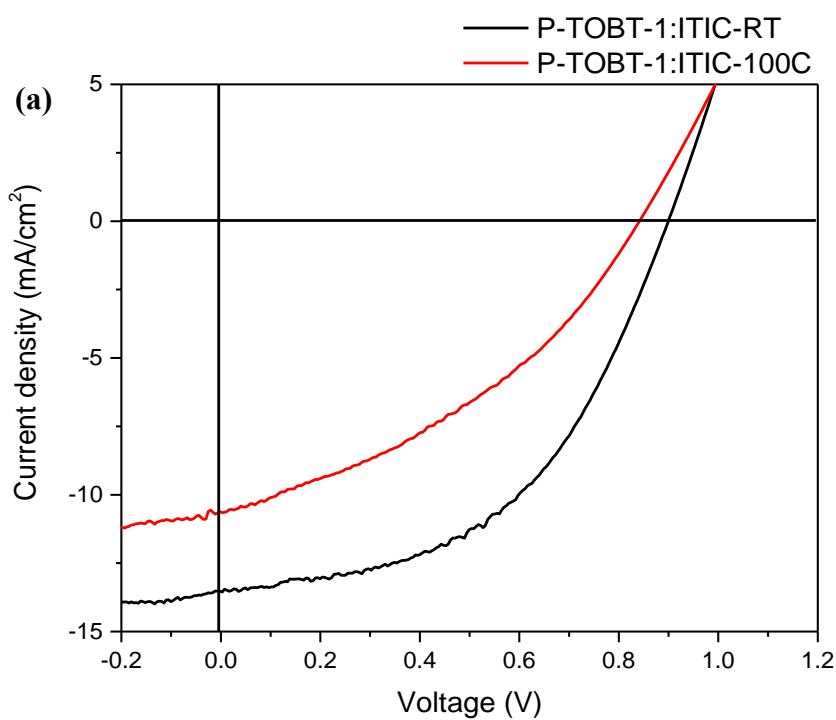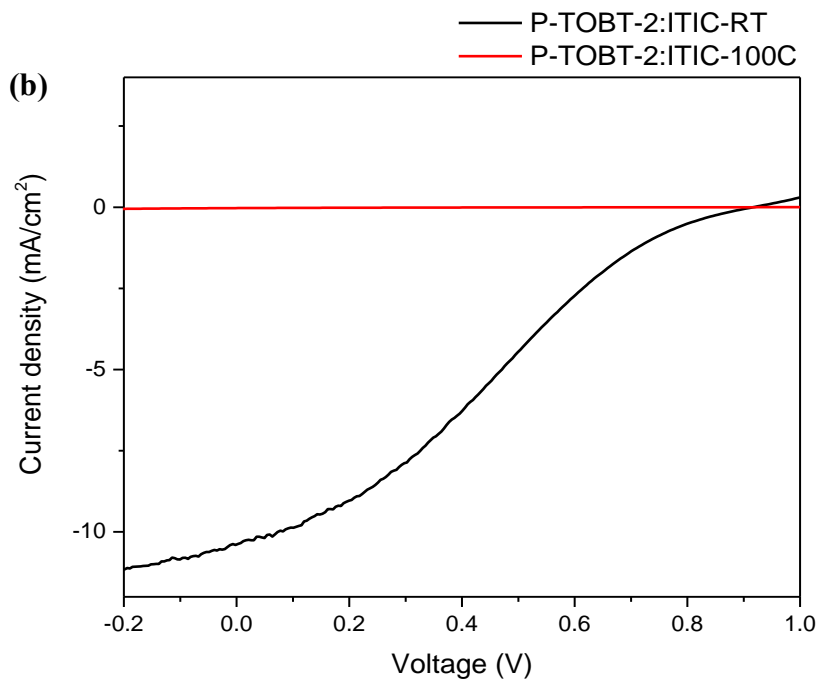
Figure 3-9 The J-V characteristic for the solar cell device based on **(a)** P-TOBT-1:ITIC and **(b)** P-TOBT-2:ITIC. The active layer (1:1 weight ratio) was spin-coated using a solution (16 mg/ml) in chloroform at 1500 rpm.

Table 3-2 Summary of device performance of P-TOBT-1:ITIC and P-TOBT-2:ITIC in conventional structure.

Sample	Jsc (mA/cm^2)	Voc (V)	FF	PCE (%)	Rs(ohm/ cm^2)	Rsh(ohm/ cm^2)
P-TOBT-1:ITIC-RT	13.54	0.90	0.50	6.03	19	505
P-TOBT-1:ITIC-100°C	10.63	0.84	0.37	3.33	22	375
P-TOBT-2:ITIC-RT	10.39	0.92	0.26	2.52	268	200
P-TOBT-2:ITIC-100°C	/	/	/	/	/	/

As mentioned before, the contact of interlayer may limit the improvement of solar cell performance, so we consider that changing structure of device may address this problem. Herein, we chose the inverted structure (ITO/ZnO /active layer/MoO$_3$ /Ag) instead of conventional ones of which configuration was shown in **Figure 3-10 (a)**. The results of P-TOBT-1:ITIC and P-TOBT-2:ITIC are shown in **Table 3-3** and **Figure 3-10**. Ultimately, the highest efficiency reached 9.04% when the temperature was 100 °C, indicating that the annealing will not deteriorate the contact between layers in this structure. Combined with XRD results, P-TOBT-1 exhibited higher crystallinity degree after annealing at 100 °C for 10 mins, which may enhance the transport of free carriers, resulting in higher Jsc. Furthermore, the s-shape of I-V curve, indicating bad contact between layers, in P-TOBT-2:ITIC system of conventional structure was also solved by changing configuration to inverted structure.

Figure 3-10 (a) Schematic representation of inverted device structure, the J-V

characteristic for the solar cell device based on **(b)** P-TOBT-1:ITIC and **(c)** P-TOBT-2:ITIC. The active layer (1:1 weight ratio) was spin-coated using a solution (20 mg/ml) in chloroform at 1500 rpm.

Table 3-3 Summary of device performance of P-TOBT-1:ITIC and P-TOBT-2:ITIC in inverted structure.

Sample Inverted Structure (CF)	Jsc (mA/cm^2)	Voc (V)	FF	PCE (%)	Rs(ohm/ cm^2)	Rsh(ohm/ cm^2)
P-TOBT-1:ITIC-RT	13.13	0.82	0.56	6.04	15	657
P-TOBT-1:ITIC-100C	19.86	0.82	0.55	9.04	9	416
P-TOBT-1:ITIC-130°C	16.17	0.82	0.44	5.81	15	235
P-TOBT-1:ITIC-160°C	9.18	0.75	0.37	2.55	27	166
P-TOBT-2:ITIC-RT	11.38	0.86	0.56	5.48	11	787
P-TOBT-2:ITIC-100C	12.66	0.90	0.56	6.32	12	434
P-TOBT-2:ITIC-130°C	8.19	0.77	0.44	2.74	24	418
P-TOBT-2:ITIC-160°C	4.16	0.47	0.36	0.70	52	274

Apart from the improvement by changing structure, it's worthy to note that solar cell performance of two isomers exhibited a clear difference. From XRD results, the crystallinity degree of P-TOBT-1:ITIC blend film is more intense than that of P-TOBT-2:ITIC, which may alleviate geminate and bimolecular recombination. Furthermore, combined with AFM images of the neat film, shown in **Figure 3-11 (a,c)**, the morphology and roughness of two isomers were similar. After annealing at 100 °C,

some aggregations were formed which may be caused by rearrangement after thermal treatment (**Figure 3-11 (b,d))**. On the other hand , the blend films of P-TOBT-1:ITIC were very smooth (RMS: 0.36 nm) and no aggregation is observed even after thermal treatment (**Figure 3-11 (g)**). However, for P-TOBT-2:ITIC, larger phase separation was observed resulting in higher roughness (0.85 nm) after annealing (**Figure 3-11 (h)**). The poorer charge separation and transportation caused by coarsened morphology may explain the lower current density of P:TOBT-2:ITIC solar cell.
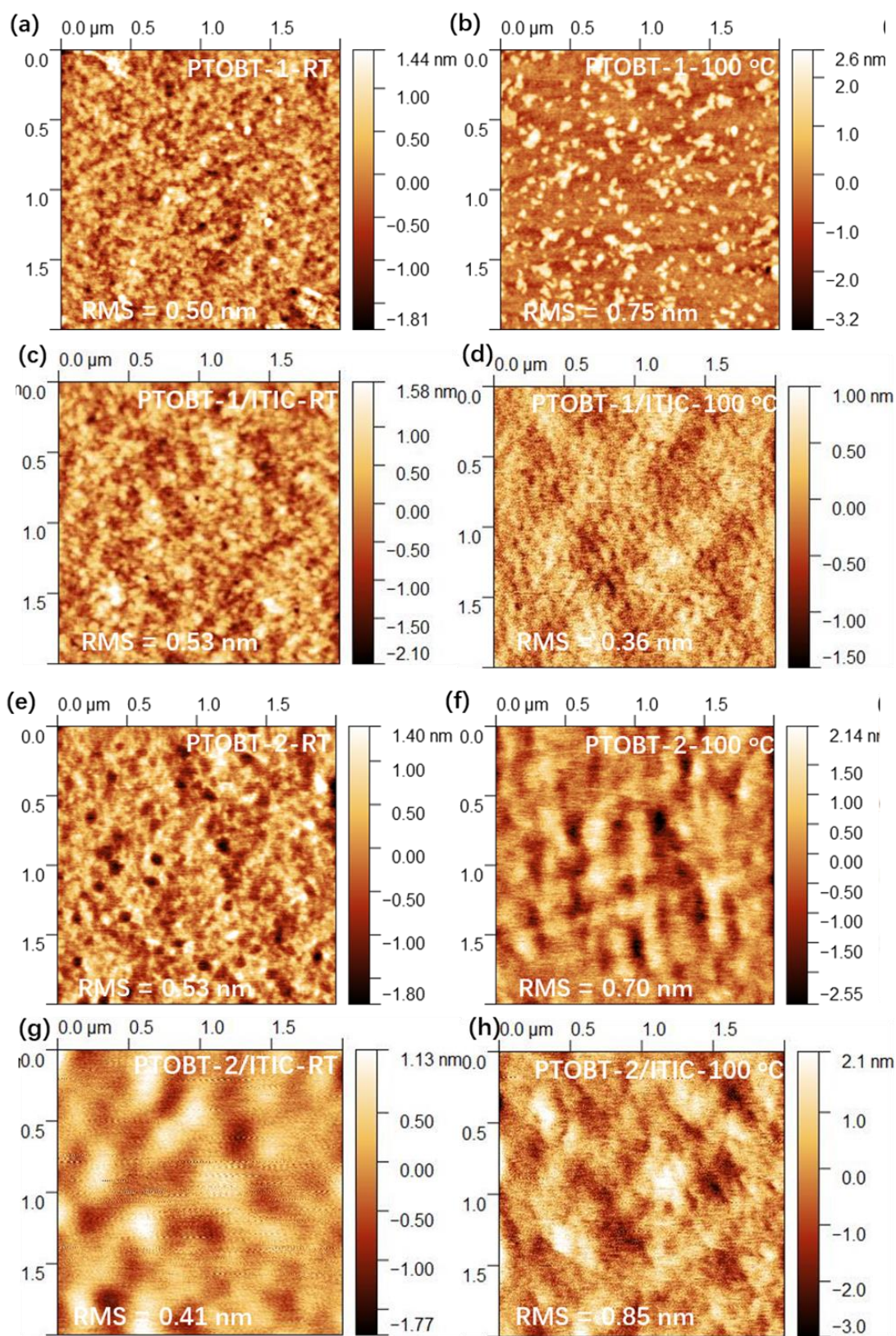
Figure 3-11 AFM height images of thin film of **(a, b, c, d)** PTOBT-1 and **(e, f, g, h)** PTOBT-2 spin-coated on PEDOT: PSS/ITO substrates processed at room temperature **(a, c, e, g)** and 100 °C **(b, d, f, h)**.

SCLC method was applied to investigate the ability of charge carrier transportation in the perpendicular direction to the substrates. The device structures were ITO/PEDOT:PSS (40 nm)/active layer/MoO$_3$ (10 nm)/Al (100 nm) and ITO/ZnO (40 nm)/active layer/LiF (1nm)/Al (100 nm) for hole-only and electron-only devices, respectively. As shown in **Figure 3-12** and **Table 3-4**, the P-TOBT-1:ITIC exhibited 1.95×10^{-4} for electron mobility and 6.34×10^{-5} cm^{2}V^{-1}s^{-1} for hole mobility, respectively. Additionally, The P-TOBT-2:ITIC exhibited 7.58×10^{-4} for electron mobility and 6.75×10^{-5} cm^{2}V^{-1}s^{-1} for hole mobility, respectively. The hole mobilities of the two isomers were similar but the electron mobility of PTOBT-1:ITIC was higher than P-TOBT:ITIC. The above results showed that PTOBT-1 have higher charge carrier mobility in both the parallel and perpendicular direction to the substrate which will be beneficial to the dissociation of excitons and transportation of the charge carriers to corresponding electrodes. Combined with XRD and AFM results, the better microstructure and stronger crystallinity, enhanced the electron mobility of P-TOBT-1:ITIC leading to higher efficiency while P-TOBT-2:ITIC indicated coarsened morphology, weaker crystallinity and lower electron mobility.
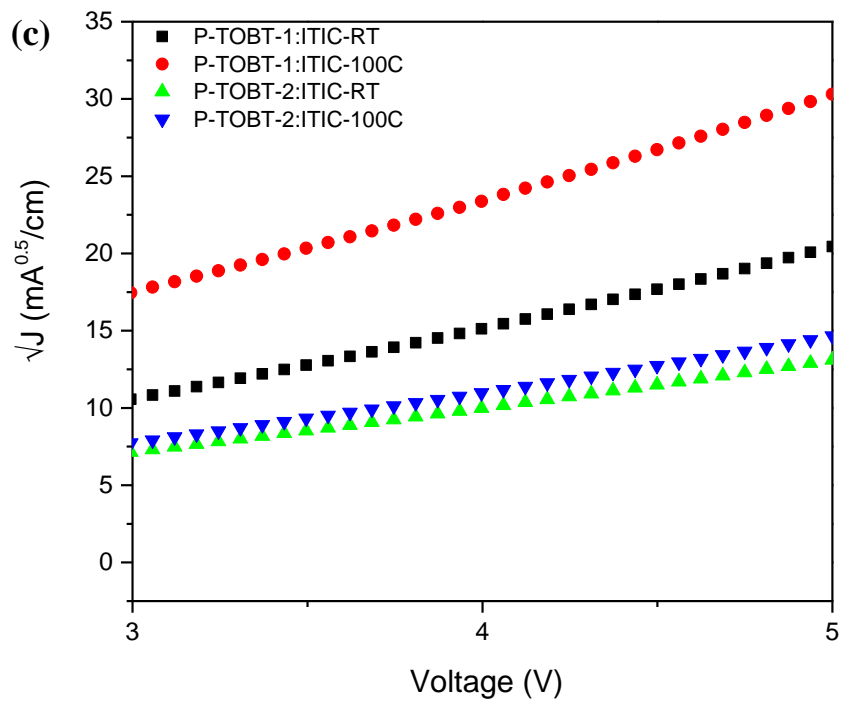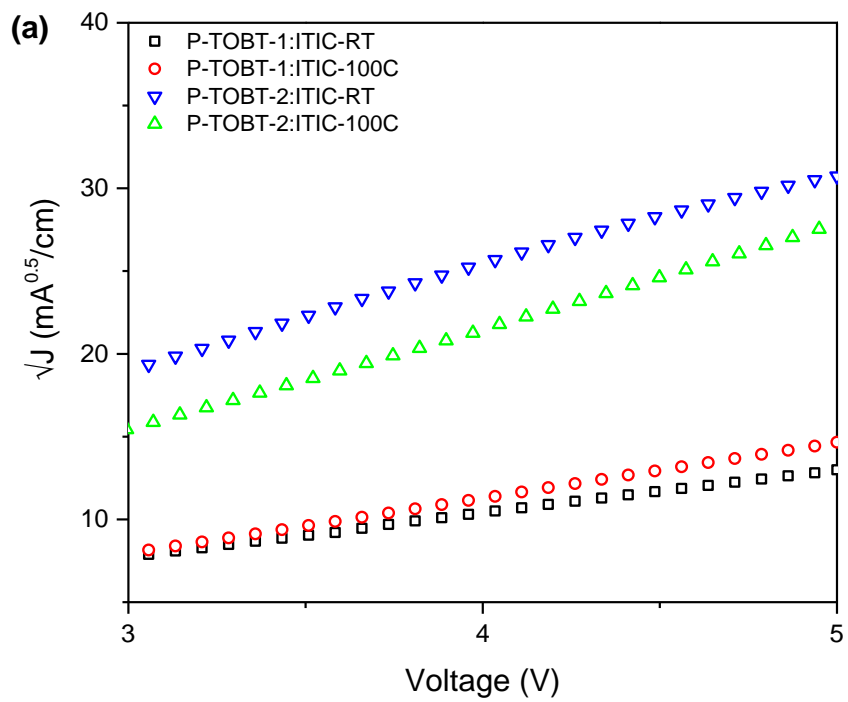
Figure 3-12 (a) Hole and **(b)** electron mobilities of PTOBT-1:ITIC and PTOBT-2:ITIC by SCLC method.

Table 3-4 Summary of the hole and electron mobility of PTOBT-1:ITIC and PTOBT-2:ITIC.

	PTOBT-1:ITIC		PTOBT-2:ITIC	
	RT	100 ºC	RT	100 ºC
μ_{hole} ($cm^2V^{-1}s^{-1}$)	4.16×10^{-5}	6.34×10^{-5}	2.44×10^{-4}	7.58×10^{-5}
$\mu_{electron}$ ($cm^2V^{-1}s^{-1}$)	1.29×10^{-4}	1.95×10^{-4}	4.93×10^{-5}	6.75×10^{-5}

3.3.2 Optimization of OPV Performance for P-TOBT-1:ITIC

In order to further optimize film quality, another solvent *o*-dichlorobenzene with higher boiling point (~190 °C) was investigated. The results of P-TOBT:ITIC in *o*-dichlorobenzene are shown in **Figure 3-13** and **Table 3-5**. Ultimately, the Jsc dropped to 15.32 mA/cm^2 and fill factor also decreased to 49%. Meanwhile the shunt resistance decreased slightly to 347 ohm/cm^2 and the series resistance almost doubled compared with our results with lower boiling point chloroform as processing solvent. This may be caused by unbalanced hole and electron mobilities as the higher boiling point of *o*-dichlorobenzene leading to larger aggregation.
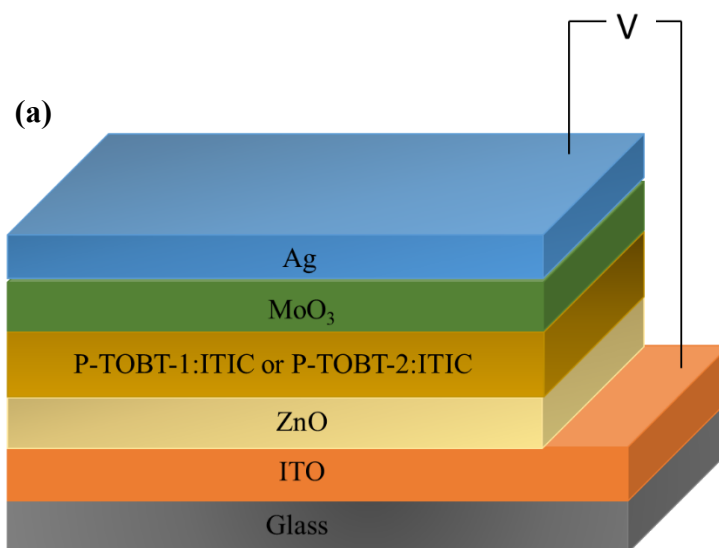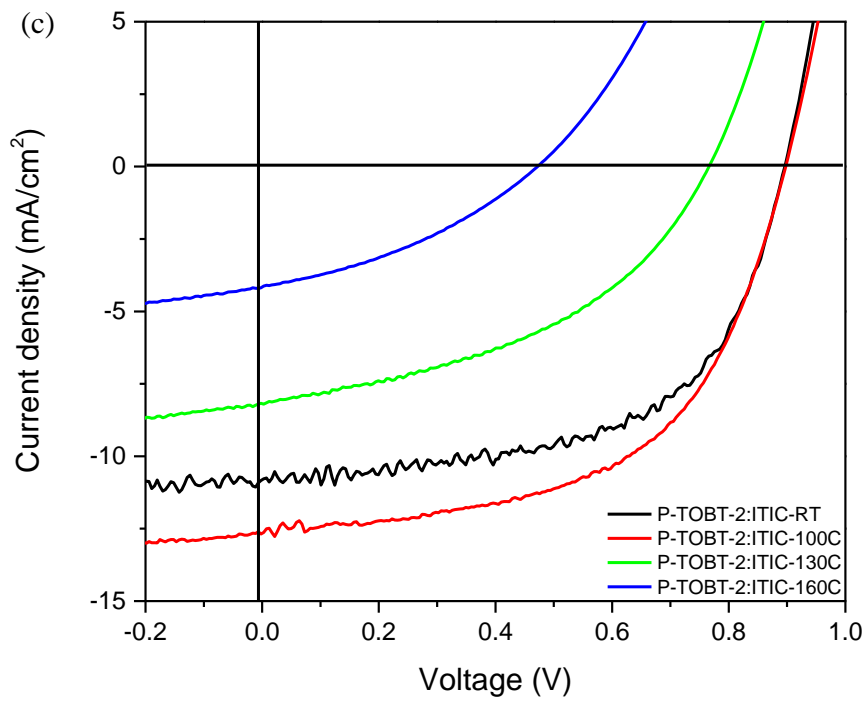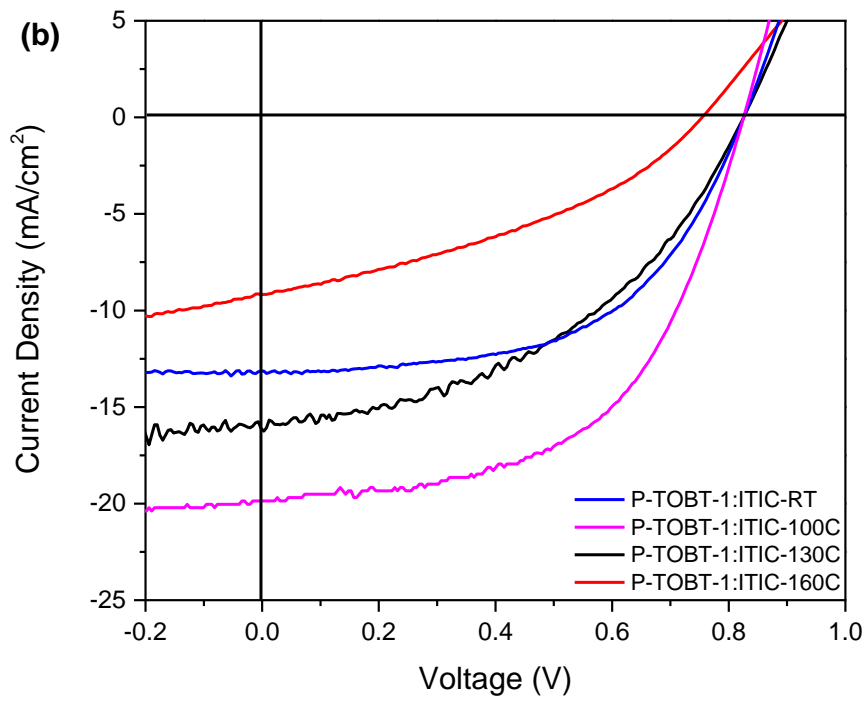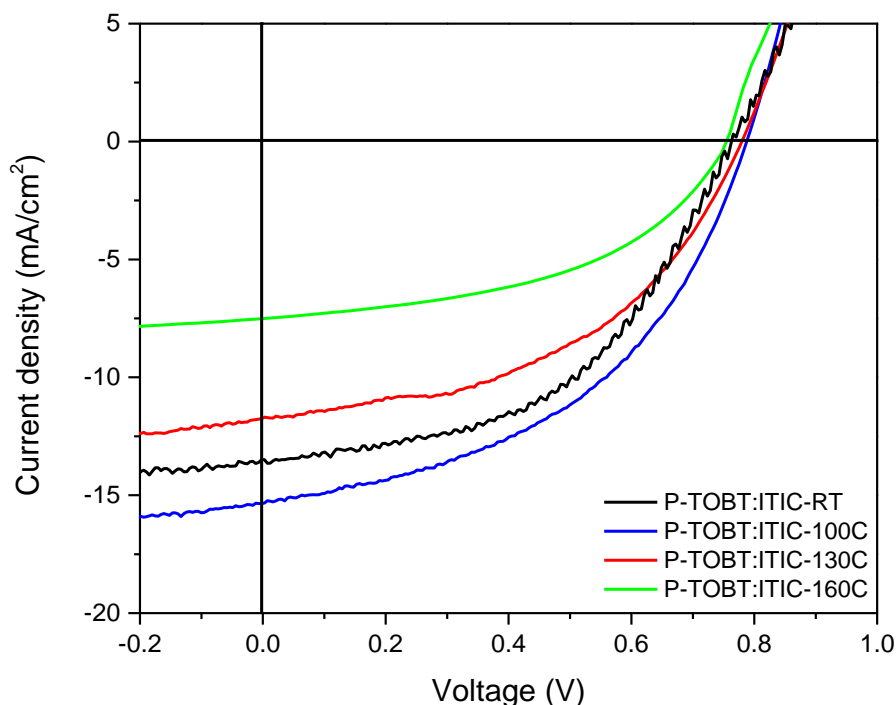
Figure 3-13 The J-V characteristic for the solar cell device based on **(a)** P-TOBT-1:ITIC and **(b)** P-TOBT-2:ITIC. The active layer (1:1 weight ratio) was spin-coated using a solution (20 mg/ml) in *o*-dichlorobenzene at 1500 rpm.

Table 3-5 Summary of device performance of P-TOBT-1:ITIC. The active layer spin-coated using a solution (20 mg/ml) in *o*-dichlorobenzene.

Sample	Jsc (mA/cm^2)	Voc (V)	FF	PCE (%)	Rs(ohm/ cm^2)	Rsh(ohm/ cm^2)
P-TOBT-1:ITIC-RT	13.49	0.76	0.50	5.17	352	19
P-TOBT-1:ITIC-100°C	15.32	0.78	0.49	6.27	347	16
P-TOBT-1:ITIC-130°C	11.72	0.78	0.48	4.36	330	25
P-TOBT-1:ITIC-160°C	7.49	0.75	0.48	2.73	319	27

As discussed before, the grain size of P-TOBT-1:ITIC in *o*-dichlorobenzene may be too large. Therefore, the lower boiling point solvent was required to form moderate domains. Therefore, we consider changing solvent to chlorobenzene of which boiling point (~135℃) is between chloroform and *o*-dichlorobenzene. The results of P-TOBT:ITIC in chlorobenzene are shown in **Figure 3-14** and **Table 3-6**. Consequently, although the series resistance increases slightly, the fill factor improved from 49% to 60% by almost doubled shunt resistance. This may be caused by the better heterojunction which could influence the interfacial barrier to facilitate the charge drifting toward the corresponding electrode.[99] Therefore, not only morphology, the contact between layers also plays a significant role in collecting free carriers. However, the Jsc dropped to 10.93 mA/cm^2 which may be still caused by unfavorable grain size. As a result, although the FF improved, the performance is still not as good as that in

chloroform.
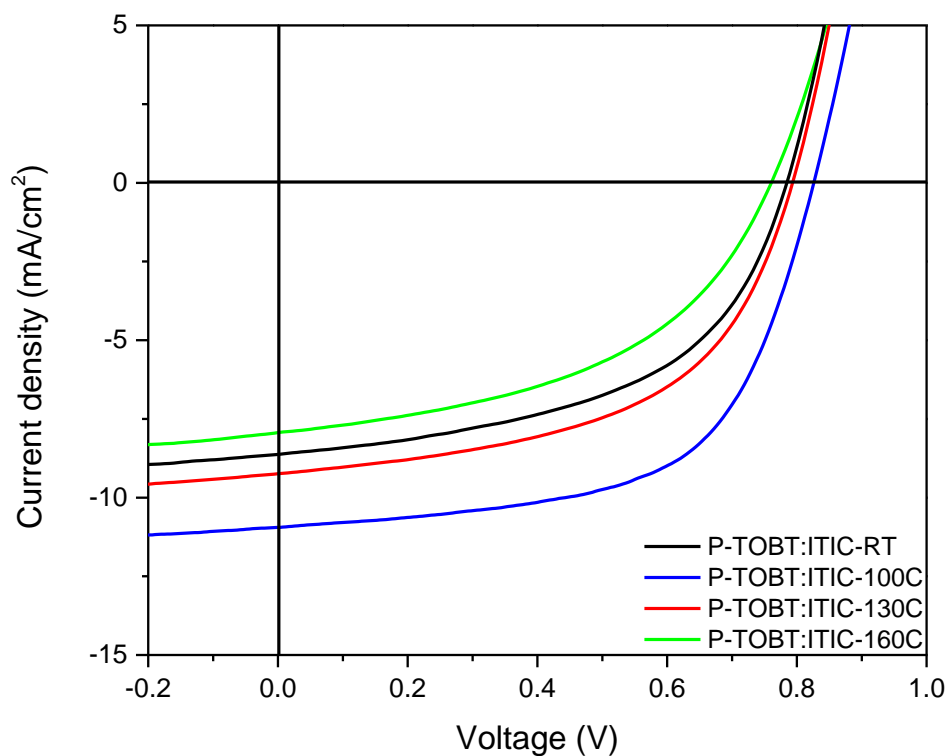
Figure 3-14 The J-V characteristic for the solar cell device based on **(a)** P-TOBT-1:ITIC and **(b)** P-TOBT-2:ITIC. The active layer (1:1 weight ratio) was spin-coated using a solution (20 mg/ml) in chlorobenzene at 1500 rpm.

Table 3-6 Summary of device performance of P-TOBT-1:ITIC. The active layer spin-coated using a solution (20 mg/ml) in chlorobenzene.

Sample	Jsc (mA/cm^2)	Voc (V)	FF	PCE (%)	Rs(ohm/ cm^2)	Rsh(ohm/ cm^2)
P-TOBT-1:ITIC-RT	8.61	0.78	0.51	3.49	529	12
P-TOBT-1:ITIC-100°C	10.93	0.82	0.60	5.43	724	12

P-TOBT-1:ITIC-130°C	9.23	0.79	0.53	3.90	523	12
P-TOBT-1:ITIC-160°C	7.93	0.75	0.47	2.85	438	21

3.3.3 Stability of OPV Performance Based on P-TOBT-1:ITIC.

Although we achieved high efficiency of P-TOBT-1:ITIC, the efficiency dropped from ~9.03% to ~6.55% after 20 mins exposure to air. In the bulk-heterojunction area, moisture in the active layer of OSCs could lead to a stronger recombination of free carriers.[100] This is the reason why it is difficult for us to measure the EQE, which need to exposure to air for measurement. The Jsc calculated from EQE (**Figure 3-15 (a)**) is 13.99 mA/cm^2, which is consistent with the 15.35 mA/cm^2 got from I-V curve after EQE measurement.

In order to improve the stability of P-TOBT-1:ITIC, wax and PMMA were applied as encapsulation avoid air exposure and moisture encroachment (**Figure 3-15 (c)** and **Figure 3-15 (d)**). We tested the efficiency immediately after encapsulation of wax, which is lower than that without any encapsulation. However, the performance is quite stable even after 12h exposure to air. The low efficiency may be caused by the relatively high temperature of melted wax (~60 °C) which is equivalent to device annealing. On the other hand, the original efficiency after encapsulation of PMMA was lower and get worse after exposure to air for 12 h. The I-V curve exhibits obviously low shunt resistance, indicating PMMA possibly deteriorate the contact between layers.

(a)

(b)

P-TOBT-1:ITIC-After 20min
P-TOBT-1:ITIC-After 12h

(c)

P-TOBT-1:ITIC-With wax encapsulation
P-TOBT-1:ITIC-After 12h with wax encapsulation

(d)

P-TOBT-1:ITIC-With PMMA encapsulation
P-TOBT-1:ITIC-After 12h with PMMA encapsulation

73
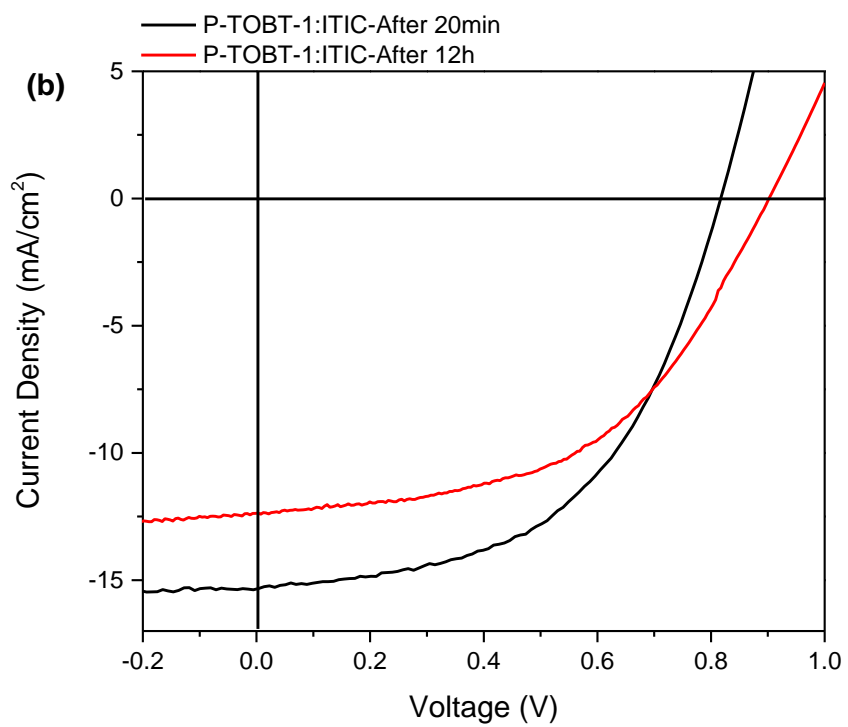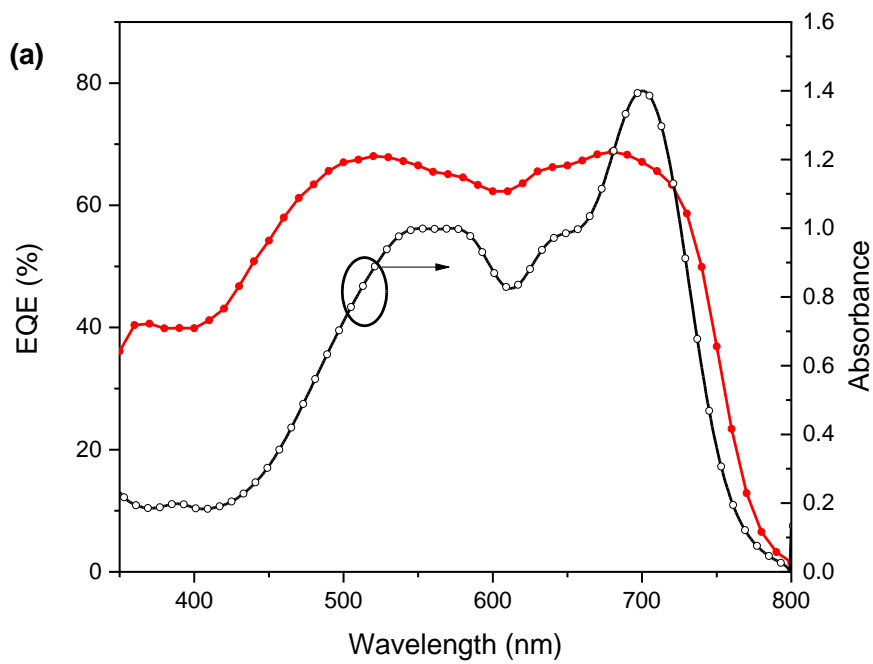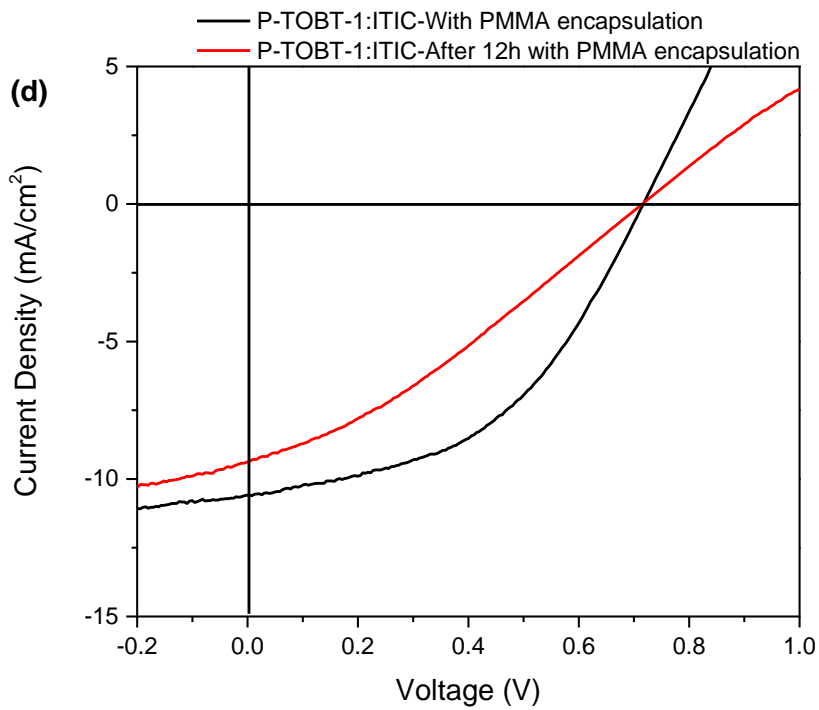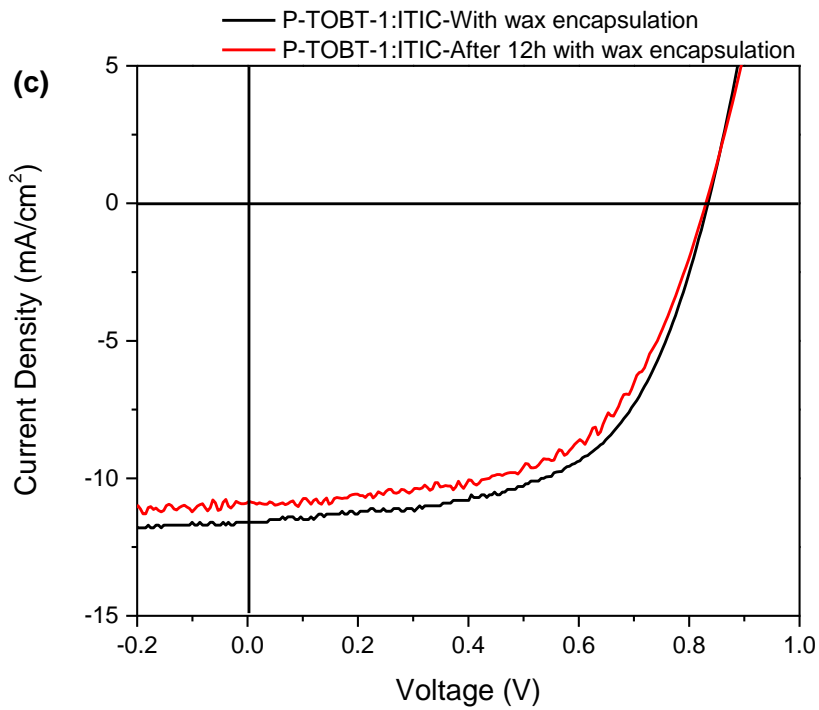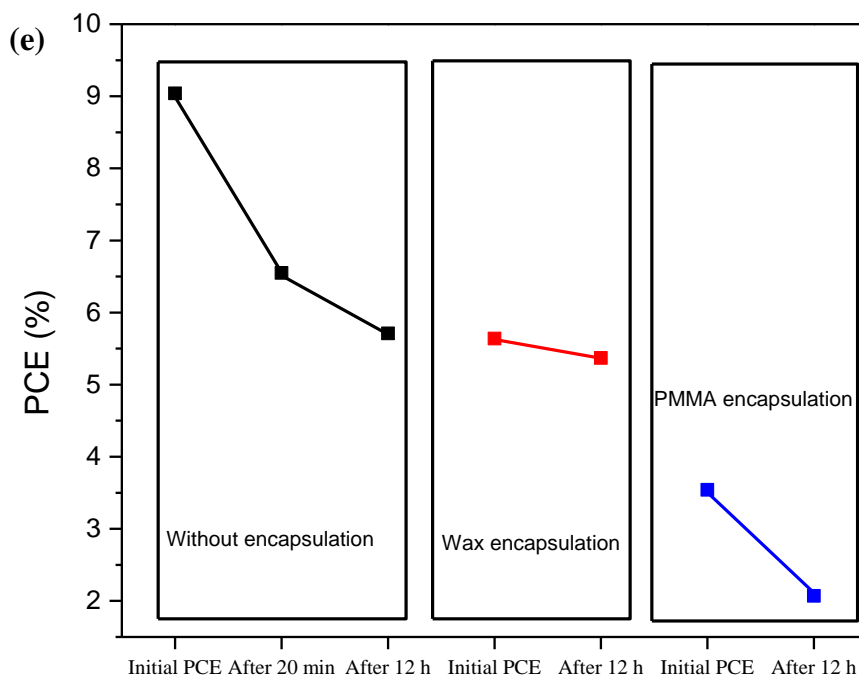
Figure 3-15 (a) EQE curve of PSCs and absorption spectra based on P3HT(rr~98%):ITIC and P3HT(rr~85%):ITIC, **(b)** the J-V characteristic for the solar cell device based on P-TOBT-1:ITIC after 20 mins and 12h, **(c), (d)** the J-V characteristic for the solar cell device based on P-TOBT-1:ITIC with wax and PMMA encapsulation, respectively. The active layer (1:1 weight ratio) was spin-coated using a solution (16 mg/ml) in chloroform at 1500 rpm, **(e)** the summery of PCE for different encapsulation.

Table 3-7 Summary of device performance of P-TOBT-1:ITIC and P-TOBT-2:ITIC with encapsulation of wax and PMMA.

Without encapsulation	Jsc (mA/cm^2)	Voc （V）	FF	PCE （%）	Rs (ohm/cm^2)	Rsh (ohm/cm^2)

	Jsc (mA/cm²)	Voc （V）	FF	PCE （%）	Rs (ohm/cm²)	Rsh (ohm/cm²)
P-TOBT-1:ITIC- after 20 min	15.35	0.82	0.52	6.55	12	679
P-TOBT-1:ITIC- after 12h	12.37	0.90	0.51	5.71	13	681
Wax encapsulation	**Jsc (mA/cm²)**	**Voc （V）**	**FF**	**PCE （%）**	**Rs (ohm/cm²)**	**Rsh (ohm/cm²)**
P-TOBT-1:ITIC	11.59	0.83	0.58	5.64	14	1282
P-TOBT-1:ITIC- After 12h	10.87	0.83	0.60	5.37	15	1204
PMMA encapsulation	**Jsc (mA/cm²)**	**Voc （V）**	**FF**	**PCE （%）**	**Rs(ohm/cm²)**	**Rsh (ohm/cm²)**
P-TOBT-1:ITIC	10.58	0.72	0.47	3.54	25	296
P-TOBT-1:ITIC- After 12h	9.38	0.72	0.31	2.07	61	158

3.4 Summery and Future Directions

In conclusion, we report the performance for OSCs of two novel donor polymers with oxime group. P-TOBT-1, which consists of only Z configuration in the side chain, exhibited higher stereoregularity, resulting in higher Jsc (19.32 mA/cm²) and PCE (9.04%). On the other hand, the P-TOBT-2, which contains both Z and E configurations, showed lower PCE (6.32%) based on P-TOBT-2:ITIC OSCs as a result of lower Jsc 12.66 mA/cm². The P-TOBT-1:ITIC exhibited 1.95×10^{-4} cm²V⁻¹s⁻¹ for electron mobility and 6.34×10^{-5} cm²V⁻¹s⁻¹ for hole mobility, respectively. Additionally, The P-TOBT-2:ITIC exhibited 7.58×10^{-4} cm²V⁻¹s⁻¹ for electron mobility and 6.75×10^{-5} cm²V⁻¹s⁻¹ for hole mobility, respectively. Compared with P-TOBT-2:ITIC, the higher electron mobility of P-TOBT-1:ITIC can be explained by XRD and AFM results. The

better intermixing of donor and accepter phases with lower RMS (0.36 nm) and stronger crystallinity resulted enhanced the electron mobility of P-TOBT-1:ITIC leading to higher efficiency while P-TOBT-2:ITIC indicated coarsened morphology (RMS:0.85 nm), weaker crystallinity. Although we obtained high performance OSCs, the performance of P-TOBT:ITIC was unstable because of air exposure. Sequentially, the OSCs were encapsulated by PMMA or wax to avoid the exposure to air and moisture meanwhile those approaches deteriorated surface morphology.

To enhance the stability of P-TOBT-1:ITIC, other methods of encapsulation[101] can be applied in organic solar cells. For the further optimization, the TO electron-efficient building block could be polymerized with different comonomer[102] to enhance light absorption as well as to improve the morphology. In addition, the quenching efficiency in ITIC part are 81% and 77% for P-TOBT-1:ITIC and P-TOBT-2:ITIC respectively. This may be caused by the relatively small difference (~0.27 eV) between HOMO energy levels of donor and acceptor. On the other hand, by controlling the intramolecular electron push-pulling effects, we could tune the absorption spectra energy levels of ITIC derivatives. [103–106] Therefore, we could try ITIC derivatives, such as IT-4F[88,105], which have a relatively lower HOMO energy level to achieve higher quenching efficiency.

3.5 Experimental Section

3.5.1 Materials and Characterization

As shown in **Figure 3-16**, for the ^{1}H NMR spectra of P-TOBT-1, two singlet peaks assigned to the proton in 4-position of thiophene and C-C double bonds together with a multiple peaks assigned to protons in benzene ring coming from the blocking agent existed in the aromatic zone, suggesting that all of the side chains of were Z-configuration. While for PTOBT-2, two sets of peaks which can be assigned to Z and E configuration with the proton ratio of 1:2 were observed in the aromatic zone,

indicating that in the process of polymerization, 1/3 of the monomer **4-E** convert to **4-Z** as the latter is more stable. The number-average molecular weight (M_n) and polydispersity index (PDI) of PTOBT-1 and PTOBT-2 are 57.1, 25.3 kDa and 4.73, 1.65, respectively, as determined by gel-permeation chromatography (GPC) using polystyrene as a standard.
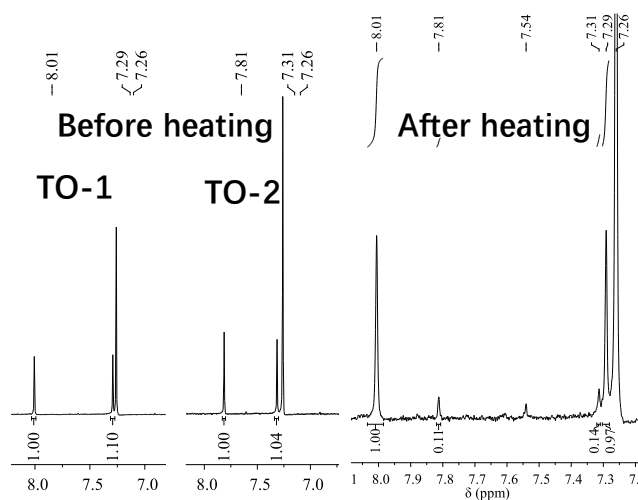
Figure 3-16 Conversion between the two isomers of monomer. ^{1}H NMR spectra before and after heating in chlorobenzene solution.

3.5.2 Fabrication and Characterization of Inverted Organic Solar Cells

The OSC devices were fabricated using the inverted structure of ITO/ZnO (40 nm)/active layer/MoO$_3$ (10 nm)/Ag (100 nm). ITO glass substrates were ultrasonicated for 20 min sequentially in de-ionized water, acetone and iso-propanol, respectively. The ZnO precursor was synthesized with the recipe of zinc acetate (197 mg), ethanolamine (54 μl) and 2-methoxyethanol (2 ml). After stirring vigorously at 50 °C overnight, the solution was filtered through a 0.5 micrometer syringe filter. Then the substrates were treated with plasma for 15min. A thin layer of ZnO was deposited through spining coated at 3500 rpm for 60s and annealed at 200 °C for 1h in the air. All the substrates were transferred to a nitrogen-filled glove box, where the D/A blend layer (~ 120 nm)

was spin-coated onto the ZnO layer. The D/A blends were dissolved in CF and the weight ratio is 1:1 with a total concentration of 16 mg/mL in the glove box. The solutions were stirred at 50 °C for 12 h, After that, the active layers were thermal annealed at 100 °C for 20 min before being transferred into a vacuum chamber. Due to relatively poor solubility in chlorobenzene or o-dichlorobenzene, the active layer was required to spin coat with hot solution on the post-annealing (100 °C) substrate. Finally, at P $\approx$ 5.0 $\times$ 10^{-6} Pa, a thin layer of MoO_3 (10 nm) and a layer of Ag (100 nm) electrode were deposited in vacuum onto the substrate. The active area is 0.0574 cm^2. The current density-voltage (J-V) characteristics of the devices were measured on an Agilent B2912A Semiconductor Analyzerwith a Science Tech SLB300-A Solar Simulator. A 450 W xenon lamp and an air mass (AM) 1.5 filter were used as the light source.

Chapter 4. Summery and Future Directions

In conclusion, this thesis presents the development of polythiophenes which could be applied into low-cost OSCs. In order to manufacture large-area solar cells, it is still necessary to develop low-cost donor polythiophenes with simpler synthetic route in traditional bulk heterojunction structure. Up to now, P3HT has the simplest synthetic route and exhibits great potential for commercialization. In Chapter 2, to enhance the interaction between donor and acceptor, P3HT (rr~85%) was applied into OSCs. Consequently, the PCE (1.33%) was successfully improved compared with P3HT (rr~98%):ITIC (0.76%). In order to further satisfy the needs for low cost and high performance, another method is to design and synthesize new novel polythiophenes (P-TOBT-1 and P-TOBT-2). Ultimately, P-TOBT-1:ITIC OSCs achieved a PCE of 9.04% after optimization in Chapter 3. To the best of our knowledge, this is the lowest synthetic cost with high PCE above 9%.

In Chapter 2, P3HT (rr~85%) was introduced to enhance the interaction between two phases, which may improve the charge transport and collection. The SCLC results demonstrate that both hole/electron mobilities of P3HT (rr~85%):ITIC blend film did improve compared with P3HT (rr~98%):ITIC. To further investigate the high mobilities of P3HT (rr~85%):ITIC, we measured both the height and phase AFM of the blend surfaces. As a result, the P3HT (rr~85%):ITIC blend film exhibited better intermixing of two phases (RMS:1.13 nm) whereas the P3HT (rr~98%):ITIC blend film demonstrated large-scale aggregation with higher RMS (2.81 nm). Consequently, a PCE of 1.33% was obtained based on P3HT (rr~85%):ITIC which is higher than that of P3HT (rr~98%):ITIC (0.76%). Therefore, bimolecular recombination may occur in P3HT (rr~98%):ITIC, resulting in poor performance. In future, in order to obtain a more systematically comparative study, P3HT with different regioregularities, such as 70%

or 90%, are required to characterize their morphology, crystallinity, electrical properties and OSC performance.

In Chapter 3, two novel donor polymers P-TOBT-1 and P-TOBT-2 were used as donors to obtain higher Voc and Jsc. Both OSCs based on P-TOBT-1:ITIC and P-TOBT-2:ITIC exhibited high Voc (0.82 ~ 0.90 V) values as designed. PTOBT-1 contains only Z configuration in the side chain while PTOBT-2 contains both Z and E configurations. Compared with P-TOBT-2:ITIC (PCE = 6.32%), the P-TOBT-1:ITIC film exhibited higher electron mobility and smoother morphology, resulting in a higher PCE (9.04%). This optimal performance was achieved by inverted structure with the D/A dissolved in chloroform for spinning coating active layer, indicating better heterojunction and contact. However, the devices based on P-TOBT-1:ITIC were unstable which may be caused by exposure to air and moisture. Future work based on P-TOBT polymers can be focused on following directions:

❖ To enhance the stability of P-TOBT-1:ITIC, other methods of encapsulation can be applied in organic solar cells[101].

❖ The electron-efficient building block (TO) could be polymerized with different comonomer to enhance light absorption as well as to improve the morphology.

❖ Try ITIC derivatives[103–106] which have relatively lower HOMO energy level to achieve higher quenching efficiency.

Bibliography

1. Home | Solar League. https://www.solarleague.org/.

2. Thakkar, V. N., Parmar, H. R. & Nayak, J. S. GHG Tank : for Heat Storage and Utilization. *International Journal of Engineering Research* **3**, 9 (2014).

3. Solar energy: Potential and future prospects - ScienceDirect. https://www.sciencedirect.com/science/article/pii/S1364032117313485.

4. Environmental impacts from the solar energy technologies - ScienceDirect. https://www.sciencedirect.com/science/article/pii/S0301421503002416.

5. Green, M. A., Emery, K., Hishikawa, Y. & Warta, W. Solar cell efficiency tables (version 37). *Progress in Photovoltaics: Research and Applications* **19**, 84–92 (2011).

6. Swanson, R. M. A vision for crystalline silicon photovoltaics. *Progress in Photovoltaics: Research and Applications* **14**, 443–453.

7. Miles, R. W., Hynes, K. M. & Forbes, I. Photovoltaic solar cells: An overview of state-of-the-art cell development and environmental issues. *Progress in Crystal Growth and Characterization of Materials* **51**, 1–42 (2005).

8. Basore, P. A. Large-area deposition for crystalline silicon on glass modules. *3rd World Conference on Photovollaic Energv Conversion* 935–938 (2003).

9. Shah, A. V. *et al.* Thin-film silicon solar cell technology. *Progress in Photovoltaics: Research and Applications* **12**, 113–142 (2004).

10. Kibria, M. T., Ahammed, A., Sony, S. M. & Hossain, F. A Review: Comparative studies on different generation solar cells technology. *Proceedings of 5th International Conference on Environmental Aspects of Bangladesh* 51–53 (2014).

11. Yan, J. & R. Saunders, B. Third-generation solar cells: a review and comparison of polymer:fullerene, hybrid polymer and perovskite solar cells. *RSC Advances* **4**, 43286–43314 (2014).

12. Cheng, Y.-J., Yang, S.-H. & Hsu, C.-S. Synthesis of Conjugated Polymers for Organic Solar Cell Applications. *Chem. Rev.* **109**, 5868–5923 (2009).

13. Blom, P. W. M., Mihailetchi, V. D., Koster, L. J. A. & Markov, D. E. Device Physics of Polymer:Fullerene Bulk Heterojunction Solar Cells. *Advanced Materials* **19**, 1551–1566 (2007).

14. Etxebarria, I., Ajuria, J. & Pacios, R. Solution-processable polymeric solar cells: A review on materials, strategies and cell architectures to overcome 10%. *Organic Electronics* **19**, 34–60 (2015).

15. Li, G., Zhu, R. & Yang, Y. Polymer solar cells. *Nature Photonics* **6**, 153–161 (2012).

16. Yan, J. & Saunders, B. R. Third-generation solar cells: a review and comparison of polymer:fullerene, hybrid polymer and perovskite solar cells. *RSC Adv.* **4**, 43286–

43314 (2014).

17. Markvart, T. & Castañer, L. Chapter I-1-A - Principles of Solar Cell Operation. in *McEvoy's Handbook of Photovoltaics (Third Edition)* (ed. Kalogirou, S. A.) 3–28 (Academic Press, 2018). doi:10.1016/B978-0-12-809921-6.00001-X.

18. Tang, C. W. Two-layer organic photovoltaic cell. *Appl. Phys. Lett.* **48**, 183–185 (1986).

19. Sariciftci, N. S., Smilowitz, L., Heeger, A. J. & Wudl, F. Semiconducting polymers (as donors) and buckminsterfullerene (as acceptor): photoinduced electron transfer and heterojunction devices. *Synthetic Metals* **59**, 333–352 (1993).

20. Yu, G. & Heeger, A. J. Charge separation and photovoltaic conversion in polymer composites with internal donor/acceptor heterojunctions. *Journal of Applied Physics* **78**, 4510–4515 (1995).

21. Brabec, C. J., Sariciftci, N. S. & Hummelen, J. C. Plastic Solar Cells. *Advanced Functional Materials* **11**, 15–26 (2001).

22. Scharber, M. C. *et al.* Design Rules for Donors in Bulk-Heterojunction Solar Cells—Towards 10 % Energy-Conversion Efficiency. *Advanced Materials* **18**, 789–794 (2006).

23. Moulé, A. J. & Meerholz, K. Morphology Control in Solution-Processed Bulk-Heterojunction Solar Cell Mixtures. *Advanced Functional Materials* **19**, 3028–

3036 (2009).

24. Günes, S., Neugebauer, H. & Sariciftci, N. S. Conjugated Polymer-Based Organic Solar Cells. *Chemical Reviews* **107**, 1324–1338 (2007).

25. Coakley, K. M. & McGehee, M. D. Conjugated Polymer Photovoltaic Cells. *Chemistry of Materials* **16**, 4533–4542 (2004).

26. Halls, J. J. M. *et al.* Efficient photodiodes from interpenetrating polymer networks. *Nature* **376**, 498–500 (1995).

27. Padinger, F., Rittberger, R. S. & Sariciftci, N. S. Effects of Postproduction Treatment on Plastic Solar Cells. *Advanced Functional Materials* **13**, 85–88 (2003).

28. Li, C. *et al.* A fullerene–single wall carbon nanotube complex for polymer bulk heterojunction photovoltaic cells. *J. Mater. Chem.* **17**, 2406–2411 (2007).

29. Lu, L. *et al.* Recent Advances in Bulk Heterojunction Polymer Solar Cells. *Chemical Reviews* **115**, 12666–12731 (2015).

30. Koster, L. J. A., Smits, E. C. P., Mihailetchi, V. D. & Blom, P. W. M. Device model for the operation of polymer/fullerene bulk heterojunction solar cells. *Physical Review B* **72**, (2005).

31. Hoppe, H. & Sariciftci, N. S. Morphology of polymer/fullerene bulk heterojunction solar cells. *J. Mater. Chem.* **16**, 45–61 (2006).

32. Yu, G., Gao, J., Hummelen, J. C., Wudl, F. & Heeger, A. J. Polymer Photovoltaic Cells: Enhanced Efficiencies via a Network of Internal Donor-Acceptor Heterojunctions. *Science* **270**, 1789–1791 (1995).

33. Clarke, T. M. & Durrant, J. R. Charge Photogeneration in Organic Solar Cells. *Chemical Reviews* **110**, 6736–6767 (2010).

34. Veldman, D., Meskers, S. C. J. & Janssen, R. A. J. The Energy of Charge-Transfer States in Electron Donor-Acceptor Blends: Insight into the Energy Losses in Organic Solar Cells. *Advanced Functional Materials* **19**, 1939–1948 (2009).

35. Scharber, M. C. On the Efficiency Limit of Conjugated Polymer:Fullerene-Based Bulk Heterojunction Solar Cells. *Advanced Materials* **28**, 1994–2001 (2016).

36. Vandewal, K. *et al.* Quantification of Quantum Efficiency and Energy Losses in Low Bandgap Polymer:Fullerene Solar Cells with High Open-Circuit Voltage. *Advanced Functional Materials* **22**, 3480–3490 (2012).

37. Brédas, J.-L., Beljonne, D., Coropceanu, V. & Cornil, J. Charge-Transfer and Energy-Transfer Processes in π-Conjugated Oligomers and Polymers: A Molecular Picture. *Chemical Reviews* **104**, 4971–5004 (2004).

38. Servaites, J. D., Ratner, M. A. & Marks, T. J. Organic solar cells: A new look at traditional models. *Energy & Environmental Science* **4**, 4410 (2011).

39. Jacoboni, C., Canali, C., Otiaviani, G. & Quaranta, A. A. A REVIEW OF SOME

40. Liu, X., Huettner, S., Rong, Z., Sommer, M. & Friend, R. H. Solvent Additive Control of Morphology and Crystallization in Semiconducting Polymer Blends. *Advanced Materials* **24**, 669–674 (2012).

41. Brabec, C. J., Shaheen, S. E., Winder, C., Sariciftci, N. S. & Denk, P. Effect of LiF/metal electrodes on the performance of plastic solar cells. *Applied Physics Letters* **80**, 1288–1290 (2002).

42. Miller, A. & Abrahams, E. Impurity Conduction at Low Concentrations. *Physical Review* **120**, 745–755 (1960).

43. Lee, J. K. *et al.* Processing Additives for Improved Efficiency from Bulk Heterojunction Solar Cells. *Journal of the American Chemical Society* **130**, 3619–3623 (2008).

44. Rogers, J. T., Schmidt, K., Toney, M. F., Kramer, E. J. & Bazan, G. C. Structural Order in Bulk Heterojunction Films Prepared with Solvent Additives. *Advanced Materials* **23**, 2284–2288 (2011).

45. Mott, N. F. Conduction in non-crystalline materials: III. Localized states in a pseudogap and near extremities of conduction and valence bands. *Philosophical Magazine* **19**, 835–852 (1969).

46. Yang, X. & Uddin, A. RETRACTED: Effect of thermal annealing on P3HT:PCBM

bulk-heterojunction organic solar cells: A critical review. *Renewable and Sustainable Energy Reviews* **30**, 324–336 (2014).

47. Ma, W., Yang, C., Gong, X., Lee, K. & Heeger, A. J. Thermally Stable, Efficient Polymer Solar Cells with Nanoscale Control of the Interpenetrating Network Morphology. *Advanced Functional Materials* **15**, 1617–1622 (2005).

48. Chen, L., Wang, P. & Chen, Y. High Efficiency of Poly(3-hexylthiophene)/[6,6]-phenyl C $_{61}$ Butyric Acid Methyl Ester Bulk Heterojunction Solar Cells through Precrystallining of Poly(3-hexylthiophene) Based Layer. *ACS Applied Materials & Interfaces* **5**, 5986–5993 (2013).

49. Li, G. *et al.* High-efficiency solution processable polymer photovoltaic cells by self-organization of polymer blends. *Nature Materials* **4**, 864–868 (2005).

50. Peng, B. *et al.* Performance improvement of polymer solar cells by using a solvent-treated poly(3,4-ethylenedioxythiophene):poly(styrenesulfonate) buffer layer. *Applied Physics Letters* **98**, 243308 (2011).

51. Peet, J. *et al.* Efficiency enhancement in low-bandgap polymer solar cells by processing with alkane dithiols. *Nature Materials* **6**, 497–500 (2007).

52. Chen, H.-Y. *et al.* Fast-Grown Interpenetrating Network in Poly(3-hexylthiophene): Methanofullerenes Solar Cells Processed with Additive. *The Journal of Physical Chemistry C* **113**, 7946–7953 (2009).

53. Erb, T. *et al.* Correlation Between Structural and Optical Properties of Composite Polymer/Fullerene Films for Organic Solar Cells. *Advanced Functional Materials* **15**, 1193–1196 (2005).

54. Ishii, H., Sugiyama, K., Ito, E. & Seki, K. Energy Level Alignment and Interfacial Electronic Structures at Organic/Metal and Organic/Organic Interfaces. *Advanced Materials* **11**, 605–625 (1999).

55. Tellinghuisen, J. The Franck-Condon Principle. in *Photons and Continuum States of Atoms and Molecules* (eds. Rahman, N. K., Guidotti, C. & Allegrini, M.) 149–156 (Springer Berlin Heidelberg, 1987).

56. Camacho, R. Polarization portraits of light-harvesting antennas: from single molecule spectroscopy to imaging. (2014) doi:10.13140/2.1.4852.5607.

57. Dennler, G., Scharber, M. C. & Brabec, C. J. Polymer-Fullerene Bulk-Heterojunction Solar Cells. *Advanced Materials* **21**, 1323–1338 (2009).

58. Mihailetchi, V. D., Blom, P. W. M., Hummelen, J. C. & Rispens, M. T. Cathode dependence of the open-circuit voltage of polymer:fullerene bulk heterojunction solar cells. *Journal of Applied Physics* **94**, 6849–6854 (2003).

59. Brabec, C. J. *et al.* Origin of the Open Circuit Voltage of Plastic Solar Cells. *Advanced Functional Materials* **11**, 374–380 (2001).

60. Hill, I. G., Kahn, A., Soos, Z. G. & Pascal, R. A. Charge-separation energy in films

of p-conjugated organic molecules. 8 (2000).

61. Blakesley, J. C. & Neher, D. Relationship between energetic disorder and open-circuit voltage in bulk heterojunction organic solar cells. *Physical Review B* **84**, (2011).

62. Elumalai, N. K. & Uddin, A. Open circuit voltage of organic solar cells: an in-depth review. *Energy & Environmental Science* **9**, 391–410 (2016).

63. Qi, B. & Wang, J. Fill factor in organic solar cells. *Physical Chemistry Chemical Physics* **15**, 8972 (2013).

64. Stubhan, T. *et al.* Increasing the Fill Factor of Inverted P3HT:PCBM Solar Cells Through Surface Modification of Al-Doped ZnO via Phosphonic Acid-Anchored C60 SAMs. *Advanced Energy Materials* **2**, 532–535 (2012).

65. Aernouts, T. *et al.* Extraction of bulk and contact components of the series resistance in organic bulk donor-acceptor-heterojunctions. *Thin Solid Films* **403–404**, 297–301 (2002).

66. Bin, H. *et al.* 11.4% Efficiency non-fullerene polymer solar cells with trialkylsilyl substituted 2D-conjugated polymer as donor. *Nature Communications* **7**, (2016).

67. Dang, M. T., Hirsch, L., Wantz, G. & Wuest, J. D. Controlling the Morphology and Performance of Bulk Heterojunctions in Solar Cells. Lessons Learned from the Benchmark Poly(3-hexylthiophene):[6,6]-Phenyl-C $_{61}$ -butyric Acid Methyl Ester

System. *Chemical Reviews* **113**, 3734–3765 (2013).

68. Fan, Q. *et al.* A New Polythiophene Derivative for High Efficiency Polymer Solar Cells with PCE over 9%. *Adv. Energy Mater.* **6**, 1600430 (2016).

69. Gao, Y. *et al.* Homo-Tandem Polymer Solar Cells with V_{OC} >1.8 V for Efficient PV-Driven Water Splitting. *Adv. Mater.* **28**, 3366–3373 (2016).

70. Xu, X. *et al.* Single-Junction Polymer Solar Cells with 16.35% Efficiency Enabled by a Platinum(II) Complexation Strategy. *Adv. Mater.* **31**, 1901872 (2019).

71. Meng, L. *et al.* Organic and solution-processed tandem solar cells with 17.3% efficiency. *Science* **361**, 1094–1098 (2018).

72. Po, R., Bianchi, G., Carbonera, C. & Pellegrino, A. "All That Glisters Is Not Gold": An Analysis of the Synthetic Complexity of Efficient Polymer Donors for Polymer Solar Cells. *Macromolecules* **48**, 453–461 (2015).

73. Qin, Y. *et al.* Highly Efficient Fullerene-Free Polymer Solar Cells Fabricated with Polythiophene Derivative. *Advanced Materials* **28**, 9416–9422 (2016).

74. Poelking, C., Daoulas, K. & Troisi, A. Advances in Polymer Science. in *In P3HT Revisited—From Molecular Scale to Solar Cell Devices*.

75. Cui, Y. *et al.* Over 16% efficiency organic photovoltaic cells enabled by a chlorinated acceptor with increased open-circuit voltages. *Nat Commun* **10**, 2515

(2019).

76. Zhang, M., Guo, X., Ma, W., Ade, H. & Hou, J. A Polythiophene Derivative with Superior Properties for Practical Application in Polymer Solar Cells. *Advanced Materials* **26**, 5880–5885 (2014).

77. Dang, M. T., Hirsch, L. & Wantz, G. P3HT:PCBM, Best Seller in Polymer Photovoltaic Research. *Adv. Mater.* **23**, 3597–3602 (2011).

78. Zhao, Y., Xie, Z., Qu, Y., Geng, Y. & Wang, L. Solvent-vapor treatment induced performance enhancement of poly(3-hexylthiophene):methanofullerene bulk-heterojunction photovoltaic cells. *Appl. Phys. Lett.* **90**, 043504 (2007).

79. Chen, D., Nakahara, A., Wei, D., Nordlund, D. & Russell, T. P. P3HT/PCBM Bulk Heterojunction Organic Photovoltaics: Correlating Efficiency and Morphology. *Nano Lett.* **11**, 561–567 (2011).

80. Holliday, S. *et al.* High-efficiency and air-stable P3HT-based polymer solar cells with a new non-fullerene acceptor. *Nat Commun* **7**, 11585 (2016).

81. Jørgensen, M. *et al.* Stability of Polymer Solar Cells. *Adv. Mater.* **24**, 580–612 (2012).

82. Bannock, J. H. *et al.* Continuous Synthesis of Device-Grade Semiconducting Polymers in Droplet-Based Microreactors. *Adv. Funct. Mater.* **23**, 2123–2129 (2013).

83. Li, Y. *et al.* Non-fullerene acceptor with low energy loss and high external quantum efficiency: towards high performance polymer solar cells. *Journal of Materials Chemistry A* **4**, 5890–5897 (2016).

84. Holliday, S. *et al.* A Rhodanine Flanked Nonfullerene Acceptor for Solution-Processed Organic Photovoltaics. *Journal of the American Chemical Society* **137**, 898–904 (2015).

85. Cha, H. *et al.* An Efficient, "Burn in" Free Organic Solar Cell Employing a Nonfullerene Electron Acceptor. *Advanced Materials* **29**, 1701156 (2017).

86. Lin, Y. *et al.* An Electron Acceptor Challenging Fullerenes for Efficient Polymer Solar Cells. *Advanced Materials* **27**, 1170–1174 (2015).

87. Chen, S. *et al.* A Wide-Bandgap Donor Polymer for Highly Efficient Non-fullerene Organic Solar Cells with a Small Voltage Loss. *Journal of the American Chemical Society* **139**, 6298–6301 (2017).

88. Zhao, W. *et al.* Molecular Optimization Enables over 13% Efficiency in Organic Solar Cells. *Journal of the American Chemical Society* **139**, 7148–7151 (2017).

89. Du, X. *et al.* Efficient Polymer Solar Cells Based on Non-fullerene Acceptors with Potential Device Lifetime Approaching 10 Years. *Joule* **3**, 215–226 (2019).

90. Barta, P., F. Cacialli, R. H. Friend, W. R. Salaneck, M. Zagorska, and A. Proń. On the influence of regioregularity on electronic and optical properties of poly

(alkylthiophenes). *Synthetic metals* **101**, 296–297 (1999).

91. Sirringhaus, H. *et al.* Two-dimensional charge transport in self-organized, high-mobility conjugated polymers. *Nature* **401**, 685–688 (1999).

92. Woo, C. H., Thompson, B. C., Kim, B. J., Toney, M. F. & Fréchet, J. M. J. The Influence of Poly(3-hexylthiophene) Regioregularity on Fullerene-Composite Solar Cell Performance. *J. Am. Chem. Soc.* **130**, 16324–16329 (2008).

93. Chen, T.-A., Wu, X. & Rieke, R. D. Regiocontrolled Synthesis of Poly(3-alkylthiophenes) Mediated by Rieke Zinc: Their Characterization and Solid-State Properties. *Journal of the American Chemical Society* **117**, 233–244 (1995).

94. Mauer, R., Kastler, M. & Laquai, F. The Impact of Polymer Regioregularity on Charge Transport and Efficiency of P3HT:PCBM Photovoltaic Devices. *Advanced Functional Materials* **20**, 2085–2092 (2010).

95. Non-fullerene acceptors for organic solar cells | Nature Reviews Materials. https://www.nature.com/articles/natrevmats20183.

96. Kotlarski, J. D., Moet, D. J. D. & Blom, P. W. M. Role of balanced charge carrier transport in low band gap polymer:Fullerene bulk heterojunction solar cells. *J. Polym. Sci. B Polym. Phys.* **49**, 708–711 (2011).

97. Li, Z. *et al.* Donor polymer design enables efficient non-fullerene organic solar cells. *Nat Commun* **7**, 13094 (2016).

98. Helgesen, M., Søndergaard, R. & Krebs, F. C. Advanced materials and processes for polymer solar cell devices. *J. Mater. Chem.* **20**, 36–60 (2010).

99. Liu, H. *et al.* Boosting Organic–Metal Oxide Heterojunction via Conjugated Small Molecules for Efficient and Stable Nonfullerene Polymer Solar Cells. *Adv. Energy Mater.* **9**, 1900887 (2019).

100.   Wang, X., Xinxin Zhao, C., Xu, G., Chen, Z.-K. & Zhu, F. Degradation mechanisms in organic solar cells: Localized moisture encroachment and cathode reaction. *Solar Energy Materials and Solar Cells* **104**, 1–6 (2012).

101.   Sarkar, S., Culp, J. H., Whyland, J. T., Garvan, M. & Misra, V. Encapsulation of organic solar cells with ultrathin barrier layers deposited by ozone-based atomic layer deposition. *Organic Electronics* **11**, 1896–1900 (2010).

102.   Liang, Y. *et al.* For the Bright Future-Bulk Heterojunction Polymer Solar Cells with Power Conversion Efficiency of 7.4%. *Adv. Mater.* **22**, E135–E138 (2010).

103.   Hou, J., Inganäs, O., Friend, R. H. & Gao, F. Organic solar cells based on non-fullerene acceptors. *Nature Mater* **17**, 119–128 (2018).

104.   Li, S. *et al.* Energy-Level Modulation of Small-Molecule Electron Acceptors to Achieve over 12% Efficiency in Polymer Solar Cells. *Adv. Mater.* **28**, 9423–9429 (2016).

105.   Zheng, Z. *et al.* A Highly Efficient Non-Fullerene Organic Solar Cell with a

Fill Factor over 0.80 Enabled by a Fine-Tuned Hole-Transporting Layer. *Adv. Mater.* **30**, 1801801 (2018).

106.   Song, X. *et al.* A Highly Crystalline Fused-Ring n-Type Small Molecule for Non-Fullerene Acceptor Based Organic Solar Cells and Field-Effect Transistors. *Adv. Funct. Mater.* **28**, 1802895 (2018).